Rapid Computational Aerodynamics for Aircraft Gust Response Analysis

Thesis submitted in accordance with the requirements of
the University of Liverpool for the degree of Doctor in Philosophy
by

Philipp Bekemeyer (MSc.)

May 2018

Abstract

Computational engineering methods play a more and more important role in building aircraft that move people and goods. Particular in high-speed civil air transport increased usage of higher fidelity simulation tools are expected to enable greener designs with a reduced environmental footprint. The challenge of including computational fluid dynamics in aircraft loads and aeroelasticity is addressed herein. During the aircraft design and certification process a tremendous number of dynamic responses to atmospheric turbulence need to be analysed. Current industrial loads computations are based on corrected linear potential flow methods which offer fast predictions but suffer several drawbacks once aerodynamic non-linearities occur. Instead, aerodynamic loads offered by computational fluid dynamics are highly accurate also at these non-linear conditions. However, computational cost necessary for performing time-marching simulations makes these methods prohibitive for unsteady loads in an industrial context. This work addresses how to efficiently introduce computational fluid dynamics based aerodynamics during gust loads analysis. It is shown that using frequency domain methods in conjunction with reduced order modelling techniques based on modal decomposition and projection offer accurate models which can be analysed at low cost. The three requirements of such an industrial gust loads process are, first, the need for high accuracy, secondly, a significant reduction of runtime compared to unsteady full order time-marching simulations, and thirdly, the ability to automatise the generation and solution process of the reduced model as well as the design and certification process. Therefore, the linearised frequency domain method is extended towards gust responses by altering the right-hand side forcing term. An aerodynamic reduced order model is constructed by computing a modal basis using proper orthogonal decomposition and projecting the linearised equations afterwards. Finally, a coupled aeroelastic model is obtained by combining the aerodynamics model with eigenmodes of the coupled Jacobian matrix for the structural vibration and projecting the coupled linearised equations. The final small sized aeroelastic model enables the inclusion of highly accurate loads during time-critical gust loads analysis and provides the opportunity to introduce these loads in a wider multidisciplinary context. Thus it is a substantial step towards establishing computational fluid dynamics for unsteady aeroelastic analysis.

Acknowledgements

I would like to acknowledge my supervisors Doctor S. Timme and Professor K. J. Badcock. In particular the insights Doctor S. Timme provided were greatly appreciated. Your persistence helped to make this thesis what it is now. Thank you for the huge amount of time you spent working with me and the discussions we had concerning various aspects of aeroelasticity, computational fluid dynamics and unsteady aerodynamic loads predictions.

I am especially thankful for the time I had together with Doctor R. Thormann and the critical questions he asked. He became a dear colleague and good friend. Your experience you kindly shared with me about computational fluid dynamics and aeroelasticity were greatly appreciated. Moreover, I would like to thank all colleagues from the office at the University of Liverpool for the discussions we had and the time we spent together working as well as just hanging out.

I would also like to thank my two examiners Professor Vassilios Theofilis and Professor Russell M. Cummings for the insights they provided and for letting me see this work from a different and angle and within a more global perspective. Comments and suggestions given have been greatly appreciated and helped to improve this work once more.

Finally, and most importantly, I would like to thank my girlfriend and family. You gave me support when needed, calmed me down if necessary and gave me the strength to finish this work. Without all of you this would not have been possible.

The research leading to these results was co-funded by Innovate UK, the UK's innovation agency, as part of the Enhanced Fidelity Transonic Wing project. This work used the ARCHER UK National Supercomputing Service (http://www.archer.ac.uk).

Declaration

I confirm that the thesis is my own work, that I have not presented anyone else's work as my own and that full and appropriate acknowledgement has been given where reference has been made to the work of others.

Philipp Bekemeyer
May 2018

List of Publications

Journal publications

Bekemeyer, P. and Timme S., "Reduced Order Transonic Aeroelastic Gust Response Simulation of Large Aircraft", Journal of Aircraft - under review

Bekemeyer, P., Thormann, R. and Timme, S., "Rapid Gust Response Simulation of Large Civil Aircraft using Computational Fluid Dynamics", The Aeronautical Journal, Vol. 121, No. 1246, pp 1795-1807, 2017

Bekemeyer, P., Thormann, R. and Timme, S., "Frequency-Domain Gust Response Simulation Using Computational Fluid Dynamics", AIAA Journal, Vol. 55, No. 7, pp 2174-2185, 2017

Conference publications

Bekemeyer, P. and Timme S., "Reduced Order Transonic Aeroelastic Gust Response Simulation of Large Aircraft", 35th AIAA Applied Aerodynamics Conference, Denver, CO, June, 2017. *AIAA Paper 2017-4361*

Bekemeyer, P., Thormann, R. and Timme, S., "Rapid Gust Response Simulation of Large Civil Aircraft using Computational Fluid Dynamics", Royal Aeronautical Society - Applied Aerodynamics Conference, Bristol, UK, July, 2016. *AAC paper O1*

Bekemeyer, P., Thormann, R. and Timme, S., "Linearised frequency domain gust analysis of large civil aircraft", European Congress on Computational Methods in Applied Sciences and Engineering, Crete Island, Greece, June, 2016. *ECCOMAS Paper 5316*

Bekemeyer, P. and Timme, S., "Reduced Order Gust Response Simulation using Computational Fluid Dynamics", 54th AIAA Aerospace Sciences Meeting, San Diego, CA, Jan. 2016. *AIAA Paper 2016-1485*

Pagliuca, G., Bekemeyer, P., Thormann, R. and Timme, S., "Model reduction for gust load analysis of free-flying aircraft", International Forum on Aeroelasticity and Structural Dynamics (IFASD), Como, Italy, June 2017. *IFASD 2017-148*

Thormann, R., Bekemeyer, P. and Timme, S., "Reduced order modelling of gust analysis using computational fluid dynamics", European Congress on Computational Methods in Applied Sciences and Engineering, Crete Island, Greece, June, 2016. *ECCOMAS Paper 5441*

Table of Contents

List of Figures

List of Tables

List of Symbols

A	=	Jacobian matrix
A_{ref}	=	reference area
$\mathcal{A}$	=	projected Jacobian matrix
C_L	=	coefficient of lift $C_L = \frac{L}{\frac{1}{2}\varrho_{\text{ref}} A_{\text{ref}} U_{\text{ref}}^2}$
C_{My}	=	coefficient of pitching moment $C_{My} = \frac{M_y}{\frac{1}{2}\varrho_{\text{ref}} c_{\text{ref}} A_{\text{ref}} U_{\text{ref}}^2}$
c_{ref}	=	reference chord length
I	=	identity matrix
i	=	imaginary unit ($= \sqrt{-1}$)
k	=	number of POD samples
L	=	lift
L_g	=	gust length
M, D, K	=	mass, damping and stiffness matrix
$\mathcal{M}, \mathcal{D}, \mathcal{K}$	=	generalised mass, damping and stiffness matrix
M_y	=	pitching moment
m	=	number of eigenmodes
n	=	number of unknowns
$\boldsymbol{q}$	=	velocity vector
$\boldsymbol{R}$	=	residual vector
r	=	POD relative information content
S	=	Schur complement matrix and POD covariance matrix
t	=	time
U_{ref}	=	reference velocity
V	=	Karhunen–Loève basis
$\mathcal{V}$	=	diagonal cell volume matrix
$\mathbf{v}$	=	eigenmodes of the POD correlation matrix
$\boldsymbol{v}_g$	=	gust disturbance velocity
$\boldsymbol{w}, \dot{\boldsymbol{w}}$	=	vectors of unknowns and corresponding temporal derivatives
$\boldsymbol{x}$, $\dot{\boldsymbol{x}}$	=	vectors containing grid location and velocity
x_0	=	gust offset
$\boldsymbol{z}$	=	vector of the reduced space variable

Greek Symbols

α	=	angle of attack
ε	=	finite difference step-size
$\boldsymbol{\eta}, \dot{\boldsymbol{\eta}}$	=	structural modal displacement and velocity
λ	=	coupled global eigenvalue
μ	=	eigenvalue of POD correlation matrix
Ξ	=	weighting factor
Φ,Ψ	=	matrix containing reduction and projection modes
ϕ,ψ	=	reduction and projection modal basis vector
$\boldsymbol{\varphi}$	=	phase shift for all points
ω	=	circular frequency
ω^*	=	reduced frequency

Subscripts

f	=	fluid
g	=	gust
ref	=	reference value (typically related to the freestream)
s	=	structural
0	=	steady-state solution, mean value or initial value

Acronyms

CFD	=	Computational Fluid Dynamics
DLM	=	Doublet Lattice Method
DLR	=	German Aerospace Center (Deutsches Zentrum für Luft- und Raumfahrt)
EASA	=	European Aviation Safety Agency
EMD	=	Eigenmode Decomposition
FAA	=	Federal Aviation Administration
FOM	=	Full Order Model
FVM	=	Field Velocity Method
LFD	=	Linearised Frequency Domain
POD	=	Proper Orthogonal Decomposition
RANS	=	Reynolds-averaged Navier–Stokes
ROM	=	Reduced Order Model
TD	=	Time Domain

Chapter 1

Introduction

Atmospheric turbulence, also referred to as gusts, resulting from sudden changes in air velocity has been regarded as a significant risk to aircraft safety and human life since the early days of flying [1–3]. Between 1964 and 1975 nearly 25% of all reported accidents with either substantial structural damage or loss of life were gust related [4]. These serious or even fatal events in the past led to strict certification requirements for turbulence encounter to ensure a high level of safety. Therefore, gust load analysis became an integral part of any aircraft design programme. In fact, when analysing accidents today, sudden changes in air velocity are still a threat, however, numbers are vanishingly small compared to the overall number of flights.

The industrial gust load analysis process, driven by safety considerations in the past, is well established and certified. However, aiming for greener aircraft with a reduced environmental footprint, various paradigm changes have been proposed including more lightweight structural design, modern composite materials or even completely new aircraft concepts. Currently low-fidelity, panel-based, aerodynamic prediction methods are applied which neglect crucial nonlinear aerodynamic effects. Thus, higher fidelity data is used to correct unsteady low-fidelity loads. Ambitious future plans in the aviation industry demand for better integrated and higher-fidelity aerodynamic modelling approaches to accurately predict unsteady loads at transonic speeds and close to the edge of the flight envelope.

The ever increasing computational power has made simulation techniques affordable, which were beyond anything possible just a decade ago. Taking advantage of this, the aviation sector strives towards virtual aircraft design and certification. The increased usage of more accurate simulations not only reduces the need for expensive wind tunnel and in-flight testing but, moreover, complex aerodynamic and aeroelastic problems can be identified earlier during the design process. Thus, initial misjudgements which can cause significant financial burdens or even failure of the whole aircraft programme can be prevented. Finally, more accurate load predictions would allow reduced certification safety margins making more radical concepts imaginable. However, increased fidelity

in aerodynamic modelling offered by computational fluid dynamics (CFD) cause a significant increase in computational cost, which is impractical in an industrial context. Therefore, efficient model reduction techniques are necessary to incorporate CFD during the routine gust load process and fully exploit the capabilities offered from increasingly accurate aerodynamic prediction tools.

1.1 A Short History and Industrial Standards

The certification requirements for gust excitations developed between the early 1930s and mid 1950s mainly due to increasing flight speeds, which led to more critical gust encounter. Before this time, considering only forces arising from manoeuvres was assumed to be sufficient to construct an airframe which can withstand all occurring in-flight loads. Even before the 1930s, atmospheric turbulence and its impact on human flight were investigated. Initial results were published as a NACA report in 1915, which is extensively reviewed in [2]. In the first regulatory text, only sharp-edge gusts with a fixed gust speed needed to be considered and airplane motion was generally neglected. From the late 1930s onwards the gust velocities were linked to the aircraft speed to account for different types such as gliders and larger commercial planes. In 1953 the sharp-edge gust shape was replaced by the one-minus-cosine (1-cos) shape and also a variation over altitude was introduced. A more in-depth review on the influence of gust loads during the early years of flying can be found in [3].

Current certification requirements include discrete gusts, as defined by the aforementioned 1-cos shape, and continuous excitations described for example by the von Kármán spectrum [5]. Both need to be considered in vertical and lateral directions. While gust lengths are defined independent of the altitude and aircraft configuration, the gust velocity varies with respect to both parameters. A decrease in altitude causes gust velocities to increase while the reverse effect is obtained for a decrease in aircraft mass. Unsteady aerodynamic effects, elastic deformations as well as changes in flight path need to be taken into account during the analysis. In addition, if a control system is present also this needs to be included. Even though the gust related parts in aircraft specifications differ slightly in wording between the Federal Aviation Administration (FAA) and the European Aviation Safety Agency (EASA), they are essentially equal. A detailed description of current EASA specifications is given in Appendix A including the relations between mass properties, flight velocities and altitude.

Pioneering approaches to numerically investigate gust responses are based on incompressible potential flow theories for two-dimensional problems. While Wagner's function is used for motion-induced aerodynamic terms [6], the Küssner function offers an analytical description of unsteady lift responses due to gust excitation in time domain [7]. The frequency domain equivalents are the Theodorsen function for unsteady airloads of a pitching and plunging aerofoil [8] and the Sears function for gust

responses [9]. An early extension to three-dimensional compressible flow can be found in [10]. No matter if aerodynamics are computed in time or frequency domain, loads become inaccurate once compressibility effects need to be considered.

Currently, gust response analysis is based on potential theory due to the small system size resulting in rapid turnaround times [11]. The most common approach is the doublet lattice method (DLM) introduced in 1969 [12]. Lifting surfaces are discretised into panels and a doublet of unknown strength is placed at the 1/4-chord line of each panel. When computing the strength of each doublet a downwash point is placed on the midspan at the 3/4-chord of each box at which the kinematic boundary condition is enforced. Since linear superposition holds, all doublets can be evaluated together leading to an integral equation. This equation can then be solved a several reduced frequencies. For a more in-depth discussion of the mathematical model of the DLM and its development, the interested reader is referred to [13]. Aperiodic gust excitations such as 1-cos gusts can be described as a combination of several harmonic excitations using an inverse Fourier transform with a complex weighting function [14, 15]. Examples of aeroelastic investigations using potential theory are widespread including flutter analysis as well as gust response problems. Different linear aerodynamic approaches are compared for an aircraft in [16].

Linear potential methods neglect non-linear and viscous effects. Therefore, they are inaccurate for the prediction of transonic flows which feature shocks and boundary layer separation. Since all modern aircraft routinely operate in the transonic flight regime, it is current industrial standard to correct unsteady loads from linear potential theory using higher-fidelity aerodynamic data [17, 18]. A first approach for extending the validity of the DLM was made in 1976 by considering global aerodynamic coefficients measured on a wind tunnel model [19]. This technique was only able to directly modify global coefficients and significant changes in the steady flow field, e.g. shocks, could not be accounted for. Nevertheless, the idea of correcting results a-posteriori was established and various different methods were proposed later on. Another early correction approach using externally computed quasi-steady surface pressures is shown in [20]. It assumes the complex ratio of the unsteady velocity distribution for a given reduced frequency to the quasi-steady velocity remains unchanged when comparing transonic and subsonic results.

A comprehensive review of correction methods, their history and some applications can be found in [18]. Here only some core concepts are introduced which can be categorised in following two different ideas. On the one hand, in [21, 22] the DLM downwash matrix is pre-multiplied with a correction matrix using CFD steady pressure distributions. Fairly good results are reported for unsteady loads in the transonic regime. A further improvement was achieved by fully replacing the matrix rather than pre-multiplying it [23]. On the other hand, several approaches work on expanding the function which is integrated, also known as Kernel function, by applying a Taylor

series [24]. An extended version of this Kernel expansion is shown in [25] and slightly more advanced in [26]. Correction data is again obtained from CFD surface pressure distributions. A similar approach has been published for gust response analysis using quasi-steady CFD results [27].

Even though corrected DLM describe current industrial practice and are well established and certified, they suffer from several drawbacks. First, the process needs expert knowledge to decide how and where to correct for obtaining an optimal balance between computational cost and fidelity. Secondly, the mapping process linking the potential flow surface description to higher-fidelity results is still challenging. Thirdly, correction factors are usually introduced only at zero frequency in a quasi-steady manner, which causes deviations for dynamic responses with significant contributions from higher frequencies as obtained for short gust lengths. These issues limit the potential for automatisation and accessibility of loads from various departments in a multidisciplinary design approach, and ultimately become a limiting factor in the design of new aircraft.

1.2 Computational Aerodynamics Gust Modelling

More radical aircraft design and smaller safety margins for certification call for a higher fidelity in aerodynamic load predictions, which can be offered by directly using CFD [28,29]. With increasing computational resources, the use of steady CFD data has become omnipresent within the aircraft design in the past few years. Moreover, aerodynamic predictions from CFD clearly describes the future for unsteady aircraft loads estimation [30]. Comprehensive introductions to CFD covering various aspects, such as spatial discretisation, time integration and turbulence modelling when the Reynolds-averaged Navier–Stokes (RANS) equations are solved, can be found in well-established textbooks [31–33]. The present work focuses on gust related aspects. For the inclusion of gust disturbances during unsteady simulation, four possible approaches are introduced next. These include the resolved gust approach, the field velocity method (FVM), the split velocity method and a method based on vortex insertion using an artificial boundary plane.

The most straightforward way is the resolved gust approach where the excitation is imposed on the farfield boundary and then convected towards the airframe. However, this attempt has a few downsides. A fine mesh everywhere between the farfield and aircraft is necessary to avoid numerical dissipation of the disturbance. Compared to all other proposed methods, computational cost is significantly higher due to two reasons. First, the grid size increases because of the fine resolution required, and secondly, the simulation time is extended to convect the disturbance to the airframe. Nevertheless, if these concerns are addressed sufficiently, the approach offers two-way interaction between gust and aircraft. Especially for short gusts, this method has shown benefits

over a fixed shape approach since the shape can be altered from the main wing before interacting with the tailplane [34, 35]. In addition, the method is not only limited to atmospheric turbulence but can also be used for vortex interaction [36, 37].

The FVM is most commonly used in industry to overcome the gust modelling problem and, compared to the resolved approach, does not need to account for numerical dissipation. Inspired by [38], the method was initially proposed to numerically investigate blade-vortex interaction by including external disturbances as artificial mesh movements or velocities [39] but was extended to gust excitations after some time [40]. During each unsteady calculation step a prescribed artificial velocity is added to the mesh velocities. Even though the shape and amplitude are unaffected by numerical dissipation during the calculation, interactions between gust and airframe are only one-way. Whereas the aerodynamic excitation will alter the surface loads, the presence of the aircraft will not affect the imposed disturbance. A simplified implementation is the surface transpiration method where additional velocities are only added at surface points [41]. Since the FVM is most commonly used for CFD based gust simulations, examples are widespread from simple aerofoils [42] over different types of wings [43–46] up to full aircraft configurations [34, 47, 48].

For the split velocity method, the idea of a prescribed velocity term used to introduce gusts is kept. Instead of changing the grid velocities, the velocity and energy in the governing equations are split into a non-prescribed and a prescribed, gust-related term [49–51]. Additional source terms, emerging from the splitting, account for the airframe-to-gust-interaction. Results are shown for a symmetric aerofoil comparing all three methods just introduced. Small differences occur once the gust length is shorter than the aerofoil chord length. More recently, the split velocity method has been applied to investigate the response of a full aircraft undergoing gust excitations as defined by certification bodies and compared to results based on the FVM [52]. Even for the shortest gust length and the highest amplitude, no significant differences between the two methods have been found suggesting that the commonly applied FVM is accurate enough within an industrial design and certification context.

Besides the three gust modelling approaches just outlined, one other option should be discussed briefly. Just like the field velocity method, it is also founded on the idea of vortex generation as needed during blade-vortex interaction simulations. Instead of prescribing gust velocities, an artificial boundary plane is inserted in front of the aircraft to introduce disturbance terms [53, 54]. While the interaction between gust and structure is not restricted, similar to the resolved gust approach and split velocity method, the problem of high numerical dissipation due to large cells far away from the configuration is avoided. Still, a high resolution is needed between main wing and the tailplane. Results are presented for a symmetric aerofoil and the X-31 fighter configuration and compared with FVM results showing minor deviations at transonic speeds, short gust lengths and large amplitudes.

For methods based on linear potential theory, such as DLM, unsteady aerodynamic forces are inherently linked to structural or external excitations, while CFD on its own predicts responses for rigid airframes. Thus, aerodynamic loads obtained from CFD need to be coupled to a structural and/or flight dynamics solver to investigate multidisciplinary aeroelastic problems [55–58]. For the representation of structural deformations different approaches are possible which include the use of a finite-element model (FEM), a condensed structural model such as a beam-stick model or a modal approach [59]. The direct coupling of CFD with an FEM offers the highest level of fidelity currently in use for one-off simulations, but computational cost required for unsteady investigation is still prohibitive in an industrial design context. Instead, projecting aerodynamic forces onto structural degrees of freedoms via modes and describing the deformation by a superposition of these modes is common. This significantly reduces computational cost but assumes a linear dynamic behaviour for structural responses. Examples are available for industry relevant configurations [60, 61].

During the aircraft design, many thousands, potentially millions of unsteady load cases, defined by flight points, mass cases, control laws etc., need to be investigated. Obtaining all necessary loads directly from time-marching CFD simulations coupled to a structural dynamics solver is still impossible within an affordable time frame. Instead, within the range of their validity linearised frequency-domain (LFD) methods offer a large efficiency improvement while maintaining the accuracy of the underlying non-linear CFD model. These methods are also known as time-linearised or linear harmonic small disturbance method and are widely used within engineering. The governing equations are linearised around a non-linear steady-state solution assuming small amplitude harmonic motion. This retains all steady non-linearities such as shock waves and shock-induced boundary layer separation.

Time-linearised Euler methods were initially applied in the field of turbomachinery to model oscillatory blade motion inside a cascade [62–64]. The first harmonic of the perturbation is compared with unsteady time-marching approaches [65, 66], showing excellent agreement at several orders of magnitude reduced computational cost. Results for external flows are presented for an aerofoil undergoing forced-motion excitation [67] as well as for a wing and an aircraft in [68]. A delta wing is discussed in [69] analysing small harmonic oscillations of elastic modes and control surfaces. A significant speed-up compared with the unsteady non-linear Euler equations solved in a time-marching approach is reported throughout. Initial work solving the RANS equations has again been published in the field of turbomachinery [70], showing good agreement between numerical simulations and experimental data for stall flutter including large separation in a blade cascade. Analysing forced-motion responses for external flows, time-saving factors between one and two orders magnitude have been reported for aerofoils and wings [71–73]. A similar decrease in cost was demonstrated for a full civil aircraft at cruise conditions [74].

1.3 Reduced Order Aeroelastic Analysis

Time-linearised methods offer already a significant reduction in computational cost since the dimension of time does not need to be resolved. In fact, sometimes LFD methods are already considered as reduced order model (ROM) [72]. In this thesis ROM is defined as a modelling approach which significantly reduces the number of spatial degrees of freedom of the investigated system. Techniques to achieve this reduction in size are routinely applied in various fields dealing with huge spaces, e.g. big data analysis, image processing and data analysis in the field of psychology and economics. Considering CFD simulations, reduced order modelling has become of interest in the last two decades to reduce cost to a level comparable with potential flow aerodynamic models but also to get an insight into complex physical phenomena [75–77]. The current section focuses on methods in the field of aerodynamics and aeroelastic.

A brief introduction to model reduction is given by categorising the various methods in different groups and subgroups. ROM techniques in the field of CFD can be separated in two main groups. One group is known as system identification in which the behaviour of full order model (FOM) solver outputs, such as lift or wing tip deflection, are analysed. The resulting ROM is then explicitly constructed for these values while neglecting others. On the one hand, this offers enormous reductions in spatial dimension, while on the other hand the model needs to be generated or adapted if a different output parameter becomes of interest. For example, if the model is generate based on the lift response behaviour, information about surface pressure distributions are not available from the ROM. Methods in the field of system identification are Volterra theory [78], autoregressive-moving-average methods [42, 79] and convolution methods [80–82]. Especially for flight dynamics investigations based on global derivatives, these methods are highly efficient. The other group is projection based ROMs which offer easy access to all quantities the FOM can provide such as surface pressure distributions needed for aircraft loads investigation. The FOM system is projected onto a modal basis to achieve spatial reduction. The full underlying system behaviour is retained, but the resulting model is generally slightly larger than system identification ROMs. Within this thesis two different projection based ROM techniques are presented and different approaches in the field of projection based models are outlined in more depth.

In general, reduction techniques via projection follow two different ideas. First, for operator based model reduction the system operator is analysed to find underlying structures which are then used for model reduction. Secondly, models which observe the FOM behaviour and subsequently construct a reduced model by using the observed data. The eigenmode decomposition approach (EMD), also known as global mode analysis, is widely used in fluid mechanics as well as some applications in aeroelasticity and resulting eigenmodes can be used for an operator based model reduction [77,83]. Proper

orthogonal decomposition (POD) instead is the most common observation based model reduction technique and has been applied in various fields [84–86]. Besides these two approaches other methods such as the eigenmode realisation algorithm have been proposed and applied to either aerodynamic or aeroelastic gust response simulations [87].

In the field of more fundamental fluid dynamics, global mode analysis has been discussed for many years and impressive results have been produced [77]. The investigation of some dominant eigenmodes offers an insight into highly complex flows such as large-scale separation, transition and buffeting [88–91]. The discussion within the multidisciplinary loads and aeroelastic context, however, is different since eigenmodes are used for subspace projection techniques to investigate so far not analyse system behavior. On the one hand, for constructing a ROM of the aerodynamic part of the coupled fluid-structural problem, modes are found numerically by analysing the operator of the Navier–Stokes equations and no sampling data is needed. The full eigenspectrum of the system Jacobian matrix, or parts of it, for a very small academic problem is computed and eigenmodes are extracted. Eigenspectra and predictive capabilities of the obtained ROM are discussed for an aerofoil case solving the Euler equations in [92] and the linearised potential equations in [93]. The number of possible eigenmodes increases with the number of grid points used and thus this technique has not yet been successfully applied to construct an aerodynamic ROM for an industry relevant test case due to the overwhelming computational resources needed.

On the other hand, model reduction based on eigenmodes of the coupled aeroelastic problem was initially used in combination with linear potential methods [83] but has been extended towards CFD aerodynamics [94] by extracting a large number of eigenmodes. As mentioned this method is not possible for a large industry relevant case due to the overwhelming computational resources needed. Since for coupled fluid-structure cases mainly the eigenmodes originating from the structural side are of interest, the Schur complement method can be applied to reformulate the coupled problem. Rather than directly investigating the coupled Jacobian matrix, structural eigenmodes can be tracked while being affected by linearised CFD aerodynamics [95]. A few, a-priori defined eigenmodes can then be used for model order reduction. While excellent agreement between results from the full non-linear system and ROM is observed for free response to initial structural excitation, results are not as satisfying during gust excitation [96]. In a special scenario just one critical eigenmode is used in a centre manifold reduction to investigate transonic aeroelastic limit cycle oscillations [97].

A reduced basis for problems of very large size can be computed using POD because the system behaviour can be sampled and thus the large system Jacobian matrix is not needed [84, 98]. Also known as Karhunen-Loève method [85, 86], POD decomposes a set of data into a minimal number of modes retaining a predefined amount of energy. Excellent reviews on POD can be found in [99–101]. In fluid dynamics, POD was first used to model coherent structures in turbulent flow fields [84]. Instead of analysing the

full system numerically, the method of snapshots was adopted [98]. A small eigenvalue problem formed from samples of the FOM is solved to obtain modes. This approach was soon extended towards frequency-domain sampling data from an incompressible three-dimensional vortex lattice method [102]. During the following two decades the method gained some popularity within the aerospace community and publications are available for a wide range of problems [103–108]. Especially the extension towards linearised CFD aerodynamics to analyse the dynamic response of a pitch-plunge aerofoil should be noted [103]. Throughout, a significant reduction in computational cost is reported and the snapshot generation was identified as the largest factor for cost reduction as well as accuracy of the obtained ROM.

Balanced proper orthogonal decomposition is derived from the aforementioned technique [109]. In addition to computing snapshots on the linearised system also the adjoint formulation is analysed and controllability and observability grammians are constructed. A singular value decomposition is then applied to obtain a predefined number of modes which are highly controllable as well as observable. While this doubles up-front cost, it decreases the number of modes necessary to capture system behaviour and results in an a-priori stable ROM [110, 111]. Models equivalent to balanced POD can be obtained without the need of adjoint samples by the eigensystem realisation algorithm as shown in [112]. A ROM for gust responses based on the eigenvalue realisation algorithm has been presented for an aeroelastic aerofoil in [87] while a demonstration for an industry relevant case is currently missing.

Summarising this elucidation on reduced order modelling, several points become evident. First, the construction of a ROM is a promising way to meet challenging industrial requirements concerning time-to-solution as well as the desire of higher fidelity aerodynamic modelling. Secondly, within the loads and aeroelastics environment projection based methods are beneficial over system identification approaches since they allow access to all flow quantities of the full order simulation rather than analysing a few pre-defined outputs. Thirdly, even though various projection based model reduction techniques have been proposed, the investigation of dynamic aircraft loads in general and gust induced loads in particular has not been discussed so far. Finally and most importantly, while plenty of methods have been demonstrated using simple academic cases of canonical geometric complexity, such as aerofoils, the discussion of large industry relevant cases barely exists. Consequently, reduced order modelling for loads and aeroelastics has been investigated by academia for nearly two decades but had very limited industrial impact.

1.4 Aim of Work and Outline of Thesis

The aim of this work is to establish methods that enable the routine use of CFD based aerodynamics for gust loads during the multidisciplinary aircraft design and

certification process and thus increase the fidelity of loads significantly. These methods need to fulfil three main requirements. First, the accuracy of predicted loads should be equivalent to loads obtained from unsteady time-marching CFD simulations. Secondly, the time-to-solution needs to be reduced by at least two orders of magnitude compared to the underlying CFD model to investigate the tremendous number of different cases in an affordable time frame. Thirdly, the software tool should require as little expert knowledge as possible to incorporate more accurate gust loads for all aspect of the aircraft design in an automated fashion.

This thesis will address three principal objectives to fulfil the aforementioned challenging requirements. First, the linearised frequency domain method, which is already commonly used for flutter stability analysis, is extended towards gust excitations. This lack has been identified by several groups and initial progress was presented [113–115]. A full verification of the methods solving the RANS equations for an aerofoil as well as an aircraft are part of this thesis and have also been published in [116]. With respect to the three outlined criteria the accuracy of the underlying model is retained. Even though an initial reduction in computational cost is achieved, this is still not fully satisfactory and expert knowledge is needed to obtain unsteady loads. Secondly, an aerodynamic ROM is constructed based on POD which uses the time-linearised snapshots as an input. Since the whole flowfield is considered during the model generation all flow quantities of interest in the aircraft loads context such as surface pressure distributions can be restored at negligible cost. This work has been presented in [117,118]. The resulting ROM model can be used in an automated fashion for aerodynamic loads while accuracy is preserved and computational cost reduced further. Finally, an aeroelastic ROM is derived by combining eigenmodes of the coupled Jacobian matrix with the aerodynamic ROM just introduced to investigate an elastic aircraft under gust excitation as required by certification authorities. Results have been presented in [119]. The coupled ROM is capable to rapidly compute CFD based aerodynamic gust loads in an industrial context while little expert knowledge is needed and thus fulfils the three criteria identified as the main challenges.

Chapter 2 outlines the underlying theoretical ideas. The RANS equations are presented and their time-linearised version is shown. An extension towards gust responses is proposed by adjusting the right-hand side forcing term. Then, reduced order modelling is introduced using POD with respect to gust disturbances applying the method of snapshots. Eigenmode decomposition is discussed next using system eigenmodes which are obtained with the Schur complement formulation. Both modal bases for model reduction are combined and additional steps are presented for a unified aeroelastic model formulation which can be rapidly evaluated to obtain unsteady loads.

Chapter 3 verifies the time-linearised gust approach for several test cases. Results are presented for an aerofoil in sub- and transonic attached-flow conditions as well as in a challenging post-buffet, detached-flow situation and moreover for a large civil aircraft

at cruise conditions. The validity of the method at a broad range of reduced frequencies is ensured by comparing transfer functions of integrated coefficients. Complex-valued surface pressure distributions and influence of the gust amplitude are analysed to discuss the assumption of a dynamically linear response. In addition, 1-cos gust excitations, as defined by international certification requirements, are discussed to demonstrate the maturity of the method for industry-relevant applications. This describes a substantial step towards replacing DLM based methods in industry with their direct frequency domain based CFD equivalent.

Chapter 4 verifies the aerodynamic ROM for gust responses using POD. As before, an aerofoil and a large civil aircraft are investigated to outline the capabilities of the method with respect to reduction in degrees of freedom and the accuracy retained. Steps necessary to obtain a reduced formulation which is stable in time-domain are outlined since integrating the reduced model in time rather than solving it in frequency domain is desirable in a multidisciplinary context. The verified method is then applied to a large civil aircraft undergoing excitations as defined by international certification requirements showcasing the industrial readiness of the method. In contrast to the LFD method discussed in Chapter 3 the proposed aerodynamic model reduction enables consideration of CFD accurate loads also when a time domain formulation is essential, such as control design, and therefore increases the application range of CFD during the aircraft design and certification.

Chapter 5 discusses aeroelastic reduced order modelling. An eigenmode decomposition ROM is first introduced and the influence of approximating the aerodynamic influence when calculating coupled eigenmodes which originate from the structural subsystem is analyses. The obtained ROM is solved for gust excitation to showcase the lack of aerodynamic modes. The model derived in Chapter 4 is then combined with the aeroelastic ROM to obtain a unified formulation for coupled fluid-structure gust load analysis. Responses of the coupled ROM for a large civil aircraft are compared with FOM simulations for integrated quantities, structural deformations and surfaces pressures with good agreement. Finally, computational cost for creating and solving the ROM is discussed to highlight the industrial readiness. The proposed ROM enables the consideration of Cfd-based, gust-induced aeroelastic loads during the aircraft design and certification by solving a small sized problem which can be evaluated on a local desktop machine in seconds.

Chapter 6 concludes this thesis. The methods presented are emphasised and key achievements are highlighted. Finally, suggestions are given on how to extend and exploit the derived ROM.

Chapter 2

Theoretical Formulation

For aeroelastic gust-encounter analysis the interaction between aerodynamics and structures needs to be modelled. The first part of this chapter gives an overview of the full order modelling approaches for both subdisciplines used within this thesis. Insights are given on the aerodynamic modelling as well as the modal structural formulation consistently applied throughout.

The second part of this chapter presents two modal decomposition and projection based ROMs. First, POD is chosen to compute modes based on snapshots which are then used to construct a low dimensional aerodynamic model. Besides the classical snapshot-based method an alteration to obtain a time-domain stable system is adopted for finite-volume CFD codes. Secondly, EMD is introduced in which coupled aeroelastic eigenmodes are traced while they are affected by the fluid. Both projection ROMs are finally combined to achieve a low dimensional model for aeroelastic gust simulations which can be solved rapidly on a local desktop computer.

2.1 Full Order Modelling

This section presents the theoretical background of the full order modelling. These formulations are not only important in the sense that they were needed to compute reference solutions but moreover describe the equations which are used by the reduced order model for sampling generation as well as during the projection based model reduction. Starting with aerodynamics which are described solving the RANS equations, the formulation is transferred into frequency domain to investigate harmonic gust responses. Aperiodic time-domain signals, such as the 1-cos gusts, are computed using an incomplete inverse Fourier transform. Structural deformations are represented by applying a modal decomposition of a full finite-element description. The full order aeroelastic system is derived combining both disciplines introduced before.

2.1.1 Aerodynamic Formulation

The Navier–Stokes level of the aerodynamic modelling hierarchy is currently the most common choice for modelling aerodynamic flows of engineering interest. They are based on the continuity equation, Newton's second law of motion and the first law of thermodynamics resulting in conservation of mass, momentum and energy, respectively. Additional equations to define the fluid properties, i.e. state equation and caloric state equation, are added to close the system. Even with the massive increase in computational resources over the past few years, directly solving the Navier–Stokes equations is not possible for an industry-relevant application. Instead, the RANS equations are solved together with a turbulence model to approximate turbulent flow behaviour at high Reynolds numbers conditions.

2.1.1.1 Reynolds-averaged Navier–Stokes Equations

For the RANS equations all flow variables are expressed as the sum of a time-average and a turbulent fluctuation around a mean value [31]. Applying a time-averaging leads to the governing equations for the mean-flow variables while additional unknowns are introduced. These are the Reynolds stress tensor and the turbulent heat-flux vector, resulting in the closure problem of turbulence. In dimensionless compact notation, the system of equations for density ϱ, velocity vector $\boldsymbol{u}$ and specific total energy e_t is written as

$$\frac{\partial \varrho}{\partial t} + \nabla \cdot (\varrho \boldsymbol{u}) = 0 \tag{2.1}$$

$$\frac{\partial \varrho \boldsymbol{u}}{\partial t} + \nabla \cdot (\varrho \boldsymbol{u} \otimes \boldsymbol{u}) + \nabla p = \nabla \cdot \boldsymbol{\tau} \tag{2.2}$$

$$\frac{\partial \varrho e_t}{\partial t} + \nabla \cdot ((\varrho e_t + p)\, \boldsymbol{u}) = \nabla \cdot (\boldsymbol{\tau} \boldsymbol{u}) - \nabla \cdot \boldsymbol{h} \tag{2.3}$$

Since the five equations above contain seven unknowns, two additional equations are necessary. Assuming a perfect gas, the equation of state becomes

$$p = \frac{\varrho T}{\gamma M_r^2} \tag{2.4}$$

with temperature defined as

$$T = \gamma\,(\gamma - 1)\, M^2 \left(e_t - \frac{1}{2}\,(\boldsymbol{u} \cdot \boldsymbol{u})^{1/2} \right). \tag{2.5}$$

Applying Fourier's law of thermal conduction, the heat-flux vector $\boldsymbol{h}$ becomes

$$\boldsymbol{h} = -\frac{1}{(\gamma - 1) M^2} \left(\frac{\mu}{RePr} + \frac{\mu_t}{RePr_t} \right) \nabla T \tag{2.6}$$

with μ as dynamic viscosity and μ_t as turbulent eddy viscosity, which assumes the classical analogy between momentum and heat transfer.

Following Stokes' hypothesis for an isotropic, Newtonian fluid assuming a linear relationship between Reynolds stresses and strain-rate tensor $\dot{\boldsymbol{\epsilon}}$, i.e.

$$\dot{\boldsymbol{\epsilon}} = \frac{1}{2}\left((\nabla \boldsymbol{u}) + (\nabla \boldsymbol{u})^T\right) \tag{2.7}$$

the combined viscous and turbulent stress tensor $\boldsymbol{\tau}$ is given by

$$\boldsymbol{\tau} = 2\left(\frac{\mu}{Re} + \frac{\mu_t}{Re}\right)\dot{\boldsymbol{\epsilon}} - \frac{2}{3}\left(\frac{\mu}{Re} + \frac{\mu_t}{Re}\right)(\nabla \cdot \boldsymbol{u})\, I - \frac{2}{3}\varrho k I \tag{2.8}$$

with k as turbulent kinetic energy.

Dimensionless parameters are defined by using dimensional reference states, specifically we use Reynolds number

$$Re = \frac{\varrho_{\text{ref}}\ U_{\text{ref}}\ c_{\text{ref}}}{\mu_{\text{ref}}}, \tag{2.9}$$

Mach number

$$M = \frac{U_{\text{ref}}}{\sqrt{\gamma R T_{\text{ref}}}} \tag{2.10}$$

and Prandtl number

$$Pr = \frac{c_p\ \mu_{\text{ref}}}{\lambda_{\text{thermal}}} \tag{2.11}$$

with c_{ref} as reference length, R as gas constant, c_p as heat capacity at constant pressure and λ_{thermal} as thermal conductivity. The turbulent Prandtl number Pr_t is 0.9 and the ratio of specific heats γ is assumed to be 1.4 for air. Sutherland's law is applied to account for changes in dynamic viscosity due to changes in temperature.

Finally, a turbulence model is necessary for the RANS equations to describe turbulent flow behaviour. Different models are currently available and used in a wide range of applications [120]. A large number is based on the Boussinesq approximation which assumes an analogy between turbulent and molecular mixing. The Spalart–Allmaras model is arguably the most popular one equation model [121] and it is consistently applied within this thesis. For this particular one equation model, eddy viscosity is computed from $\mu_t = f_{v1}\varrho\tilde{\nu}$ with f_{v1} as a near wall damping function and $\tilde{\nu}$ is described by the transport equation

$$\frac{\partial \varrho\tilde{\nu}}{\partial t} + \nabla \cdot (\varrho\tilde{\nu}\boldsymbol{u}) = \mathcal{P}_{\varrho\tilde{\nu}} + \mathcal{D}_{\varrho\tilde{\nu}} + \mathcal{W}_{\varrho\tilde{\nu}} \tag{2.12}$$

where the right hand side of the equation describes production, diffusion and near wall destruction of $\tilde{\nu}$, respectively. For a more detailed discussion of turbulence modelling the interested reader is referred to [120].

The governing equations (2.1)-(2.3) and (2.12) can be expressed in conservative arbitrary Lagrangian-Eulerian form with just one vector equation as

$$\frac{\mathrm{d}}{\mathrm{d}t}\int_{\mathcal{V}(t)} \boldsymbol{w}_f \mathrm{d}V + \int_{\mathcal{S}(t)} \Big(\boldsymbol{F}(\boldsymbol{w}_f, \boldsymbol{x}, \dot{\boldsymbol{x}}) - \boldsymbol{w}_f \dot{\boldsymbol{x}}\Big) \cdot \mathrm{d}\boldsymbol{S} = \int_{\mathcal{V}(t)} \boldsymbol{Q}(\boldsymbol{w}_f, \boldsymbol{x}) \mathrm{d}V \tag{2.13}$$

where the vector $\boldsymbol{w}_f = [\varrho, \varrho\boldsymbol{u}, \varrho e_t, \varrho\tilde{\nu}]^T$ contains aerodynamic unknowns plus one entry resulting from the Spalart–Allmaras turbulence model. Directed surface elements of the boundary $\mathcal{S}$ are described by $\mathrm{d}\boldsymbol{S} = \boldsymbol{n}\mathrm{d}S$. Inviscid and viscous fluxes are denoted by $\boldsymbol{F}$ while additional source terms from the turbulence model are contained within $\boldsymbol{Q}$. Control volumes are described by $\mathcal{V}$. Changes in mesh coordinates $\boldsymbol{x}$ and their velocities $\dot{\boldsymbol{x}}$ are described by structural deformations. Using the field velocity method, gust disturbances $\boldsymbol{v}_g$ are accounted for using mesh velocities $\dot{\boldsymbol{x}}$ [40].

Applying a finite-volume discretisation, the ordinary differential equation (ODE) in semi-discrete form

$$\frac{\mathrm{d}\mathcal{V}\boldsymbol{w}_f}{\mathrm{d}t} = \boldsymbol{R}_f(\boldsymbol{w}_f, \boldsymbol{x}, \dot{\boldsymbol{x}}, \boldsymbol{v}_g) \tag{2.14}$$

is obtained where $\boldsymbol{R}_f$ denotes the non-linear fluid residual corresponding to the unknowns, and diagonal matrix $\mathcal{V}$ now contains the cell volumes.

2.1.1.2 Time-Linearisation

The difference between the vector of conservative fluid variables $\boldsymbol{w}_f$ and an equilibrium solution $\boldsymbol{w}_{f,0}$ is introduced as

$$\Delta\boldsymbol{w}_f = \boldsymbol{w}_f - \boldsymbol{w}_{f,0} \tag{2.15}$$

and accordingly for external disturbances $\Delta\boldsymbol{v}_g = \boldsymbol{v}_g - \boldsymbol{v}_{g,0}$, mesh coordinates $\Delta\boldsymbol{x} = \boldsymbol{x} - \boldsymbol{x}_0$ and mesh velocities $\Delta\dot{\boldsymbol{x}} = \dot{\boldsymbol{x}} - \dot{\boldsymbol{x}}_0$. Assuming small disturbances, a Taylor expansion is applied around the equilibrium point

$$\begin{aligned}\mathcal{V}\frac{\mathrm{d}\Delta\boldsymbol{w}_f}{\mathrm{d}t} + \boldsymbol{w}_f\frac{\mathrm{d}\Delta\mathcal{V}}{\mathrm{d}t} = \boldsymbol{R}_f(\boldsymbol{w}_{f,0}, \boldsymbol{x}_0, \dot{\boldsymbol{x}}_0, \boldsymbol{v}_{g,0}) + \frac{\partial\boldsymbol{R}_f}{\partial\boldsymbol{w}_f}\Delta\boldsymbol{w}_f + \frac{\partial\boldsymbol{R}_f}{\partial\boldsymbol{x}}\Delta\boldsymbol{x} + \dots \\ \dots \frac{\partial\boldsymbol{R}_f}{\partial\dot{\boldsymbol{x}}}\Delta\dot{\boldsymbol{x}} + \frac{\partial\boldsymbol{R}_f}{\partial\boldsymbol{v}_g}\Delta\boldsymbol{v}_g + H.O.T.\end{aligned} \tag{2.16}$$

where $\frac{\partial\boldsymbol{R}_f}{\partial\boldsymbol{w}_f} = A_{ff}$ describes the fluid Jacobian matrix. The matrices $\frac{\partial\boldsymbol{R}_f}{\partial\boldsymbol{x}}$, $\frac{\partial\boldsymbol{R}_f}{\partial\dot{\boldsymbol{x}}}$ and $\frac{\partial\boldsymbol{R}_f}{\partial\boldsymbol{v}_g}$ denote changes in fluid residual due to mesh deformation, mesh point velocities and gust excitation, respectively. All derivatives are formed around the same equilibrium point $(\boldsymbol{w}_0, \boldsymbol{x}_0, \dot{\boldsymbol{x}}_0, \boldsymbol{v}_{g0})$.

The first term on the right-hand side of the latter equation is equivalent to the non-linear steady-state flow residual which accounts for steady aerodynamic non-linearities and is assumed to be converged to machine precision. For all cases presented herein,

the steady state is converged at least 10 order of magnitude throughout. For non-converging steady states, which could indicate an underlying unsteady flow, a different route to solution must be chosen. In the field of fluid dynamics, this has been discussed widely and controversially and the reader is referred, for instance, to [77].

Subsequently, the system is transferred into frequency domain assuming $\Delta\mathbf{w}$, $\Delta\boldsymbol{x}$, $\Delta\dot{\boldsymbol{x}}$ and $\Delta\boldsymbol{v}_g$ all change harmonically in time, e.g.

$$\Delta\mathbf{w} = \hat{\boldsymbol{w}}_f e^{i\omega t} \tag{2.17}$$

Thus, Eq. (2.16) becomes after some re-arranging

$$\left(\frac{\partial \boldsymbol{R}_f}{\partial \boldsymbol{w}_f} - i\omega^* \mathcal{V}\right) \hat{\boldsymbol{w}}_f = -\frac{\partial \boldsymbol{R}_f}{\partial \boldsymbol{x}}\hat{\boldsymbol{x}} - \frac{\partial \boldsymbol{R}_f}{\partial \dot{\boldsymbol{x}}}\hat{\dot{\boldsymbol{x}}} + \boldsymbol{w}_f \frac{\mathrm{d}\Delta\mathcal{V}}{\mathrm{d}t} - \frac{\partial \boldsymbol{R}_f}{\partial \boldsymbol{v}_g}\hat{\boldsymbol{v}}_g \tag{2.18}$$

with $\hat{\boldsymbol{w}}_f$, $\hat{\boldsymbol{x}}$, $\hat{\dot{\boldsymbol{x}}}$ and $\hat{\boldsymbol{v}}_g$ denoting complex-valued Fourier coefficients. The reduced frequency ω^* is defined as

$$\omega^* = \frac{\omega c_{\mathrm{ref}}}{U_{\mathrm{ref}}} \tag{2.19}$$

where ω denotes the angular frequency. The first two forcing terms on the right-hand side are origination from structural deformations. Changes in aerodynamic residual due to a deformation of the applied spatial discretisation is denoted by $\frac{\partial \boldsymbol{R}_f}{\partial \boldsymbol{x}}\hat{\boldsymbol{x}}$ while changes in residual due to mesh velocities are contained within $\frac{\partial \boldsymbol{R}_f}{\partial \dot{\boldsymbol{x}}}\hat{\dot{\boldsymbol{x}}}$. The following derivation will primarily focus on gust disturbances described by the right-hand side term $\frac{\partial \boldsymbol{R}_f}{\partial \boldsymbol{v}_g}\hat{\boldsymbol{v}}_g$. However, techniques as introduced in Section 2.1.1.3 can also be applied to analyse structural forced motion.

Applying the chain rule, the gust-related right-hand side in Eq. (2.18) becomes

$$\frac{\partial \boldsymbol{R}_f}{\partial \boldsymbol{v}_g}\hat{\boldsymbol{v}}_g = \frac{\partial \boldsymbol{R}_f}{\partial \dot{\boldsymbol{x}}}\frac{\partial \dot{\boldsymbol{x}}}{\partial \boldsymbol{v}_g}\hat{\boldsymbol{v}}_g \tag{2.20}$$

where $\dot{\boldsymbol{x}}$ describes the mesh velocities applied to model the gust during the CFD calculation using the field velocity method (FVM). Since the relation between gust disturbance $\boldsymbol{v}_g$ and artificial mesh velocity $\dot{\boldsymbol{x}}$ is simply

$$\dot{\boldsymbol{x}} = -\boldsymbol{v}_g \tag{2.21}$$

the right-hand side term can be written as

$$\frac{\partial \boldsymbol{R}_f}{\partial \boldsymbol{v}_g}\hat{\boldsymbol{v}}_g = -\frac{\partial \boldsymbol{R}_f}{\partial \dot{\boldsymbol{x}}}\hat{\boldsymbol{v}}_g. \tag{2.22}$$

If a different method than the FVM is applied to model the gust, the term $\frac{\partial \mathbf{R}_f}{\partial \boldsymbol{v}_g}$ needs to be evaluated in accordance with the chosen approach.

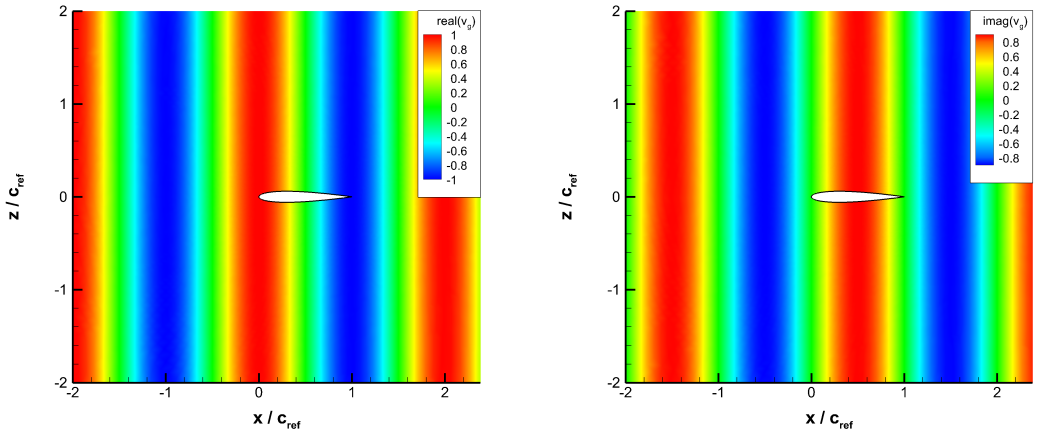

(a) Real part of $\hat{\boldsymbol{v}}_g$ (b) Imaginary part of $\hat{\boldsymbol{v}}_g$

Figure 2.1: Visualisation of complex gust vector $\hat{\boldsymbol{v}}_g$ with $\omega^* = \pi$ and $x_0 = 0$

For solving the full-order linearised frequency domain system, the matrix $\frac{\partial \mathbf{R}_f}{\partial \dot{\boldsymbol{x}}}$ is not build explicitly since only the result of the matrix-vector product $\frac{\partial \boldsymbol{R}_f}{\partial \dot{\boldsymbol{x}}}\hat{\boldsymbol{v}}_g$ is of interest. Instead, a finite-difference evaluation,

$$\frac{\partial \boldsymbol{R}_f}{\partial \dot{\boldsymbol{x}}}\hat{\boldsymbol{v}}_g = \frac{\boldsymbol{R}_f(\boldsymbol{w}_0, \boldsymbol{x}_0, \dot{\boldsymbol{x}}_0, \boldsymbol{v}_{g0} + \varepsilon\hat{\boldsymbol{v}}_g) - \boldsymbol{R}_f(\boldsymbol{w}_0, \boldsymbol{x}_0, \dot{\boldsymbol{x}}_0, \boldsymbol{v}_{g0} - \varepsilon\hat{\boldsymbol{v}}_g)}{2\varepsilon} \tag{2.23}$$

with a known gust shape vector $\hat{\boldsymbol{v}}_g$ and ε as the finite-difference step size, is used to form Eq. (2.22). The cost of two additional residual evaluations is necessary to construct the right-hand side before solving the linear system while the computational overhead of forming and storing the matrix can be avoided.

Furthermore, an analytical description of the gust shape vector is introduced as

$$\hat{\boldsymbol{v}}_g(\boldsymbol{x}, \omega^*) = v_{gz} e^{i\boldsymbol{\varphi}(\boldsymbol{x}, \omega^*)} \tag{2.24}$$

where v_{gz} and $\boldsymbol{\varphi}(\boldsymbol{x}, \omega^*)$ denote the constant vertical gust amplitude and the phase shift vector which is evaluated element-wise, respectively. The phase shift can either be obtained from a Fourier transform of a sinusoidal time-domain signal or, more easily and adopted from classical loads analysis using linear aerodynamics [59], using the expression

$$\boldsymbol{\varphi}(\boldsymbol{x}, \omega^*) = (\boldsymbol{x} + x_0)\,\frac{\omega^*}{c_{\text{ref}}} \tag{2.25}$$

where x_0 is the initial distance between gust and airframe reference point. The complex vector $\hat{\boldsymbol{v}}_g$ for a vertical gust for an aerofoil case is shown in Fig. 2.1. The definition follows the classical approach of infinitesimally extending the gust in vertical and for three-dimensional cases also in spanwise direction. Since the gust varies harmonically

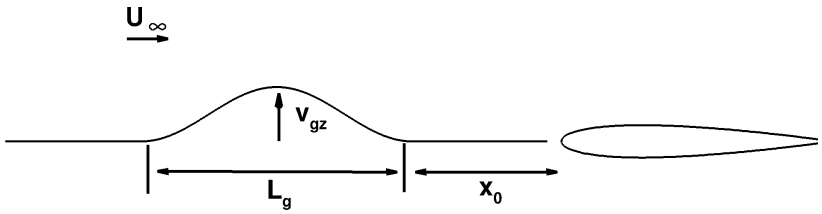

(a) Aerofoil case

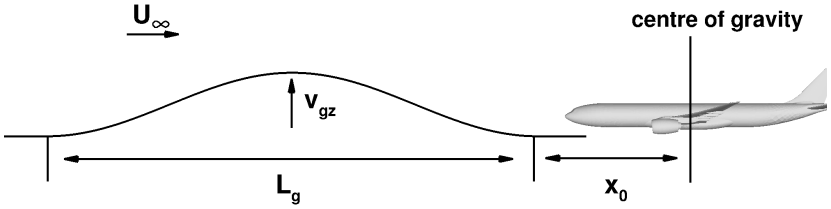

(b) Aircraft case

Figure 2.2: Sketch of 1-cos gust parameters

over the domain, the pattern reoccurs after each period and all points within the computational domain are affected.

For lateral gust excitations the expression becomes after combining Eqs. (2.24) and (2.25)

$$\hat{\boldsymbol{v}}_g(\boldsymbol{x}, \omega^*) = v_{gy} e^{i(\boldsymbol{x}+x_0)\frac{\omega^*}{c_{\text{ref}}}} \tag{2.26}$$

with v_{gy} as constant lateral gust amplitude.

2.1.1.3 Reconstruction of Aperiodic Time-Domain Signals

Solving Eq. (2.18) gives the system response to an excitation at one predefined reduced frequency which correlates to a sinusoidal gust. A 1-cos gust shape however is aperiodic and parameters are visualised in Fig. 2.2 for an aerofoil and a civil aircraft case. The magnitude over reduced frequency behaviour for a 1-cos gust as well as an additionally introduced pulse excitation is shown in Fig. 2.3(b). For both signals more than one frequency is necessary to describe the time-domain behaviour since several frequencies have a magnitude larger than zero.

Nevertheless, a frequency domain analysis can still be used to investigate aperiodic time-domain signals. Once the discrete frequency response function is calculated, results to arbitrary gust excitations can be obtained by applying a superposition in

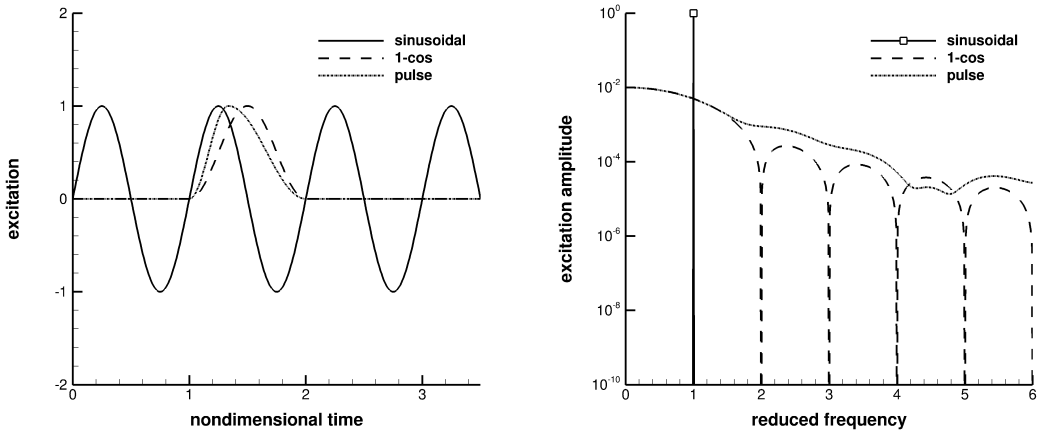

(a) Time domain (b) Frequency domain

Figure 2.3: Excitation signals represented in time and frequency domain

conjunction with a complex-valued weighting function denoted $\Xi(\omega_j^*)$

$$\Delta \boldsymbol{w}_f = \sum_j \Re\left(\Xi(\omega_j^*)\hat{\boldsymbol{w}}_{f,j} e^{i\omega_j^* t}\right) \quad \text{for} \quad j >= 0 \tag{2.27}$$

where $\Re$ describes the real part of the complex-valued coefficients. Whereas the linearised solutions $\hat{\boldsymbol{w}}_{f,j}$ are independent of the aperiodic gust shape of interest, only the weighting function needs to be re-computed using a Fourier transform on the excitation signal. This is a key strength of the LFD method since the computationally expensive part of solving Eq. (2.18) at different reduced frequencies needs to be done only once to obtain the discrete frequency response function whereas aperiodic time-domain signals can be investigated by simply recomputing the complex-valued weighting function $\Xi(\omega^*)$. The weighting function for two 1-cos gusts has been visualised in Fig. 2.4 and results from a Fourier transform of the time-domain excitation signal. The dependence of the weighting function on the gust length of interest can be seen since the shorter gust excites a longer frequency range. Whenever a pole in the magnitude occurs the phase exhibits a jump of 2π.

In general, aperiodic time-domain signals cover an infinite range of frequencies. Assuming that the magnitude of the excitation as a function of reduced frequency is decaying, an incomplete inverse Fourier transformation can be applied considering only dominant frequencies. The 1-cos excitation shows this decrease in magnitude with increasing reduced frequency. Thus, lower frequencies are more important than higher frequencies and therefore a cut-off can be defined for the reconstruction. The influence of this cut-off and the case-dependent number of retained frequencies will be discussed in detail in Chapter 3.

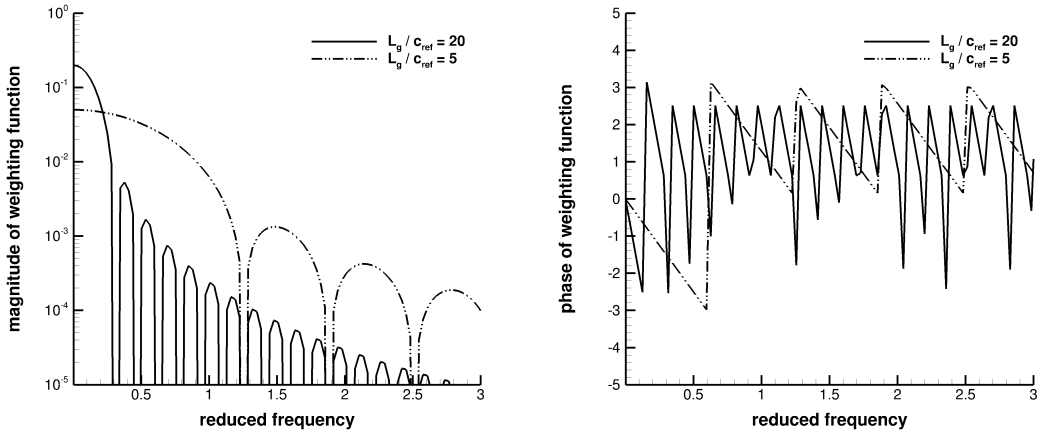

(a) Magnitude (b) Phase

Figure 2.4: Complex-valued weighting function $\Xi(\omega^*)$ for two 1-cos gusts

Instead of solving the system in frequency domain and reconstructing time-domain behaviour by using an inverse Fourier transform, also Fourier transform on a time-domain signal can be performed to obtain frequency response functions. The system response to a predefined signal is monitored in time domain and then used to compute the frequency response function for the monitored quantity. Whereas in Eq. (2.27) the linearised solutions $\hat{\boldsymbol{w}}_{f,j}$ are multiplied by the complex-valued weighting function $\Xi(\omega^*)$, now the result of the Fourier transform is divided by $\Xi(\omega^*)$. Theoretically the aperiodic 1-cos signal can be used to obtained a frequency response function using a time-domain analysis. However, it exhibits several roots and thus at least two time-domain simulations are necessary between which the gust length is altered to avoid having overlapping roots. As an alternative to the 1-cos signal, a pulse excitation can be used. The pulse excitation applied herein is a fourth order polynomial which is not symmetric with respect to the maximum value and shown in Fig. 2.3(a) [122]. Note that various other mathematical pulse descriptions are available and would also be suitable. Like the 1-cos excitation, the magnitude of the pulse excitation decreases with increasing reduced frequency. Moreover, it does not exhibit roots and thus only a single computation is necessary to compute a frequency response function.

2.1.2 Modal Structural Formulation

Structural dynamics can generally be described by

$$M\ddot{\boldsymbol{x}}_s + D\dot{\boldsymbol{x}}_s + K\boldsymbol{x}_s = \boldsymbol{f} \tag{2.28}$$

where M, D and K denote mass, damping and stiffness matrix, respectively, and $\boldsymbol{f}$ is the aerodynamic forcing term. All structural coordinates are described by $\boldsymbol{x}_s$ and

are in the order of several hundreds of thousands when using an FEM model. In this work, structural behaviour is modelled using a modal structural model. Therefore, the eigenvalues and eigenvectors of Eq. (2.28) are computed neglecting the damping term and the aerodynamic force term on the right-hand side. Resulting modes are stored in the matrix $X_s = [\boldsymbol{\chi}_1, \boldsymbol{\chi}_2, \ldots, \boldsymbol{\chi}_m]$ and are used in a Galerkin projection such that

$$\boldsymbol{x}_s = X_s \boldsymbol{\eta} \tag{2.29}$$

where $\boldsymbol{\eta}$ is the vector of modal amplitudes. The number of retained modes m is chosen based on engineering experience and is typically between 10 and 100.

Substituting Eq. (2.29) in (2.28) and projecting with X_s^T gives

$$\mathcal{M}\ddot{\boldsymbol{\eta}} + \mathcal{D}\dot{\boldsymbol{\eta}} + \mathcal{K}\boldsymbol{\eta} = X_s^T \boldsymbol{f} \tag{2.30}$$

with $\mathcal{M}$, $\mathcal{D}$ and $\mathcal{K}$ as modal mass, damping and stiffness matrix. Modes are scaled to obtain an identity modal mass matrix which results in angular structural frequencies squared on the diagonal of the modal stiffness matrix. Modal structural damping is neglected. Surface deformations of several modes of a large civil aircraft, together with the undeformed surface, are visualised in Fig. 2.5. Even though the modal analysis is performed for the whole aircraft, each mode mainly affects a certain part. In Figs 2.5(a), 2.5(d) and 2.5(f) the wing is deformed by a first bending, a second bending and torsion, respectively. The tail is the main region of influence in Figs. 2.5(c) and 2.5(e). In- and outboard deformations of the pylons and nacelles are shown in Fig. 2.5(b).

Rewriting Eq. (2.30) as a first order ordinary differential equation gives

$$\frac{\mathrm{d}\boldsymbol{w}_s}{\mathrm{d}t} = \boldsymbol{R}_s(\boldsymbol{w}_s, \boldsymbol{w}_f) \tag{2.31}$$

in which the modal coordinates are concatenated in $\boldsymbol{w}_s = [\boldsymbol{\eta}^T, \dot{\boldsymbol{\eta}}^T]^T$. The structural residual vector $\boldsymbol{R}_s$ is

$$\boldsymbol{R}_s(\boldsymbol{w}_s, \boldsymbol{w}_f) = \begin{bmatrix} 0 & I \\ -\mathcal{M}^{-1}\mathcal{K} & 0 \end{bmatrix} \boldsymbol{w}_s + \begin{pmatrix} 0 \\ X_s^T \boldsymbol{f} \end{pmatrix}. \tag{2.32}$$

Transforming Eq. (2.31) in frequency domain yields

$$\left(A_{ss} - i\omega^* I\right) \hat{\boldsymbol{w}}_s = \hat{\boldsymbol{b}}_s \tag{2.33}$$

where A_{ss} denotes the structural Jacobian matrix

$$A_{ss} = \begin{bmatrix} 0 & I \\ -\mathcal{M}^{-1}\mathcal{K} & 0 \end{bmatrix} \tag{2.34}$$

(a) Bending dominated mode

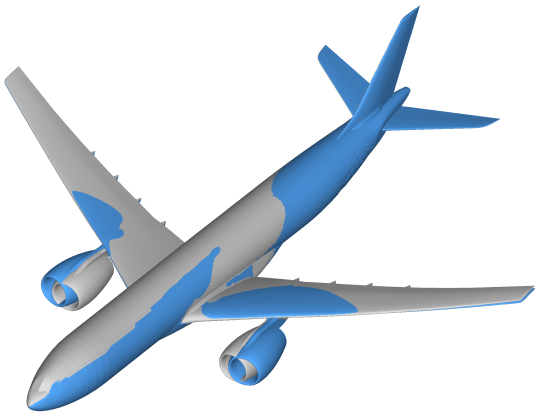

(b) Nacelle dominated mode

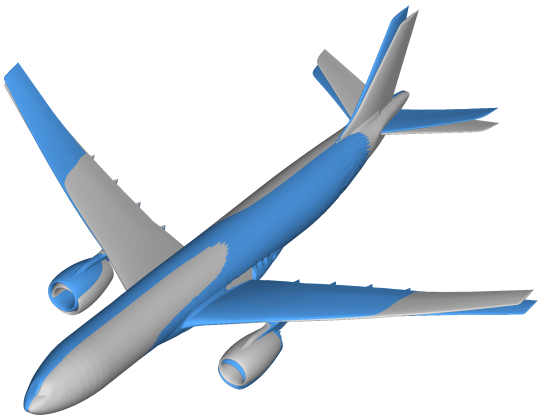

(c) Tail mode

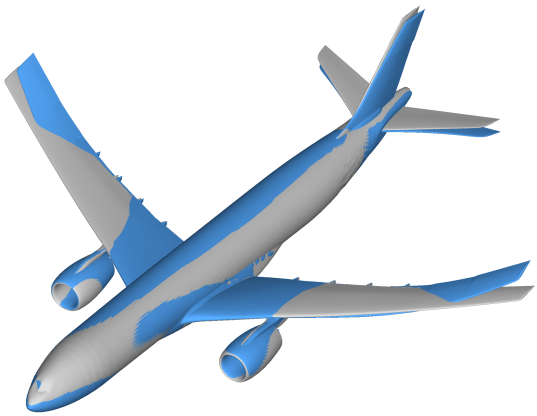

(d) Second bending dominated mode

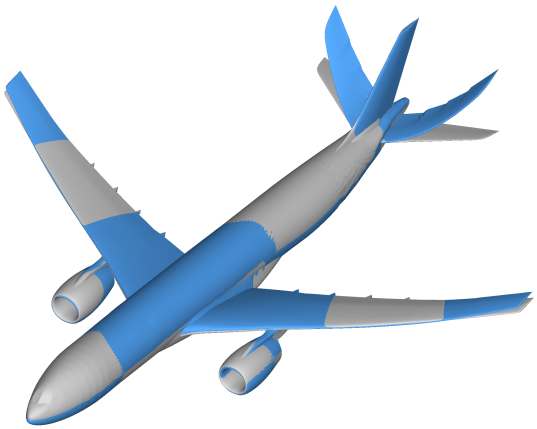

(e) Second tail mode

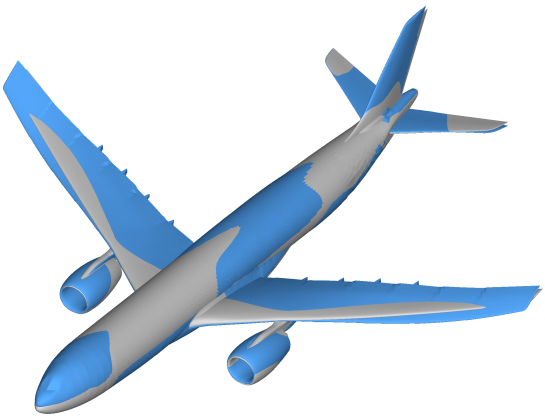

(f) Torsion dominated mode

Figure 2.5: Representative 'in-vacuum' structural mode shapes projected onto aerodynamic surface with reference shape in light grey

and $\hat{\boldsymbol{b}}_s = \left(0, X_s^T \hat{\boldsymbol{f}}\right)^T$ describes an aerodynamic harmonic excitation projected onto the structural modes.

Classical gust response analysis is performed using Eq. (2.33) and the technique presented in Section 2.1.1.3 to analysis 1-cos gust responses [59]. Note that aerodynamic influences in this formulation are solely in the right-hand-side forcing term and thus projected onto structural modes. While the source of the aerodynamic forces such as linear potential theory or CFD is arbitrary, aerodynamic quantities are not directly available once the system is solved. Instead, aerodynamic values of interest, e.g. surface pressure distributions need to be reconstructed. This can be avoided by analysing the coupled aeroelastic system directly as introduced next.

2.1.3 Coupled Aeroelastic Formulation

Recalling the aerodynamics in Eq. (2.14) and assuming structural excitation is described by Eq. (2.31) yields

$$\frac{\mathrm{d}\mathcal{V}\boldsymbol{w}_f}{\mathrm{d}t} = \boldsymbol{R}_f(\boldsymbol{w}_f, \boldsymbol{w}_s, \boldsymbol{v}_g). \tag{2.35}$$

A coupled aeroelastic formulation is obtained by combining Eq. (2.31) and (2.35)

$$\frac{\mathrm{d}\mathcal{V}\boldsymbol{w}}{\mathrm{d}t} = \boldsymbol{R}(\boldsymbol{w}, \boldsymbol{v}_g) \tag{2.36}$$

with $\boldsymbol{w} = [\boldsymbol{w}_f^T, \boldsymbol{w}_s^T]^T$ containing both aerodynamic and structural degrees of freedom. The diagonal cell volume matrix $\mathcal{V}$ has been padded with an identity matrix for all modal structural degrees of freedom. Applying a first order Taylor expansion yields

$$\mathcal{V}\frac{\mathrm{d}\boldsymbol{w}}{\mathrm{d}t} = \boldsymbol{R}(\boldsymbol{w}_0, \boldsymbol{v}_{g,0}) + \frac{\partial \boldsymbol{R}}{\partial \boldsymbol{w}}\boldsymbol{w} + \frac{\partial \boldsymbol{R}}{\partial \boldsymbol{v}_g}\boldsymbol{v}_g \tag{2.37}$$

where $\boldsymbol{R}(\boldsymbol{w}_0, \boldsymbol{v}_{g,0})$ is the coupled non-linear steady residual. Note that the term $\boldsymbol{w}\frac{\mathrm{d}\mathcal{V}}{\mathrm{d}t}$ containing the influence of changes in cell volume for the fluid degrees of freedom is now part of the coupled Jacobian matrix $\frac{\partial \boldsymbol{R}}{\partial \boldsymbol{w}}$ to simplify the notation.

The coupled system is transferred into frequency domain by assuming harmonic motion, giving

$$\left(\frac{\partial \boldsymbol{R}}{\partial \boldsymbol{w}} - i\omega^*\mathcal{V}\right)\hat{\boldsymbol{w}} = \hat{\boldsymbol{b}} \tag{2.38}$$

where $\hat{\boldsymbol{b}}$ describes a complex-valued right-hand side forcing term. For gust excitations this term becomes

$$\hat{\boldsymbol{b}} = \begin{pmatrix} \frac{\partial \boldsymbol{R}_f}{\partial \dot{\boldsymbol{x}}}\hat{\boldsymbol{v}}_g \\ 0 \end{pmatrix}. \tag{2.39}$$

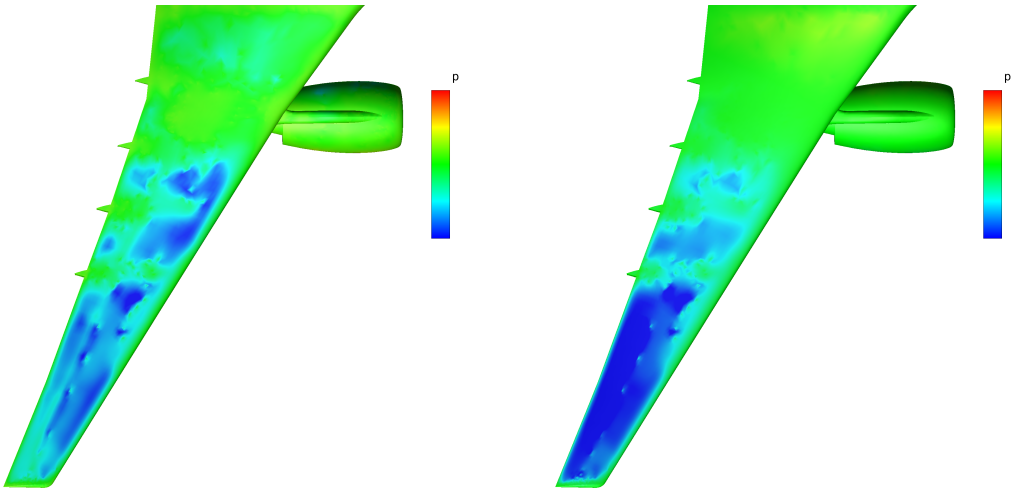

(a) Displacement part of matrix A_{fs} (b) Matrix A_{sf}

Figure 2.6: Visualisation of coupling matrices A_{fs} and A_{sf} for first bending dominated mode

The matrix A can be written as

$$A = \begin{bmatrix} \frac{\partial \boldsymbol{R}_f}{\partial \boldsymbol{w}_f} & \frac{\partial \boldsymbol{R}_f}{\partial \boldsymbol{w}_s} \\ \frac{\partial \boldsymbol{R}_s}{\partial \boldsymbol{w}_f} & \frac{\partial \boldsymbol{R}_s}{\partial \boldsymbol{w}_s} \end{bmatrix} = \begin{bmatrix} A_{ff} & A_{fs} \\ A_{sf} & A_{ss} \end{bmatrix} \tag{2.40}$$

The first entry in the double subscript denotes the differentiated residual and the second entry denotes the differentiation variable. For example, $\frac{\partial \boldsymbol{R}_f}{\partial \boldsymbol{w}_f}$ describes the fluid residual differentiated with respect to the fluid variables resulting in the fluid Jacobian matrix A_{ff}. Consequently, A_{ss} denotes the structural Jacobian matrix.

The two coupling matrices A_{fs} and A_{sf} are visualised for the first wing bending dominated mode in Fig. 2.6. The matrix A_{fs} describes the fluid response due to a surface deformation, which follows the mode shape of interest propagated through the domain due to mesh deformation. If the wing bends, mainly the outboard wing region is affected and the strongest fluid response is between leading edge and shock location. The matrix A_{sf} instead describes the dependence of the aerodynamic force, projected onto the structural modes, on the fluid unknowns. After forming this derivative no pressure terms are retained and columns/rows in the matrix A_{sf} in primitive variables simply becomes the mode shape times the surface normals in primitive form multiplied by a scaling factor which consists out of the reference length to the power of four and the density. This factor arises out of the nondimensionalisation of the system and is necessary for a consistent force transfer between structures and aerodynamics. Since the system is solved for conservative variables an addition transformation is necessary. Analysing the resulting transformed and scaled matrix, the region of highest influence is directly related to the area of highest deflection at the wing tip.

2.1.4 Practical Implementation Details

This section will focus on practical implementation aspects of the full order modelling approaches. General implementation challenges arising from the ambition of investigating industrial relevant cases using well established industrial software shall be discussed here. Additional details are given on the numerical settings applied to solve the aeroelastic system. Moreover, key technologies enabling the usage of the LFD method on large scale test cases will be outlined.

Even though Eq. (2.36) describes a closely coupled aeroelastic system, the aerodynamic and structural subsystems for time-marching reference solutions are solved loosely coupled in this work. On the one hand, this reflects the current industrial reality of highly specialised tools for different subdiscipline and allows the combination of different aerodynamic and structural solvers. On the other hand, computational cost increases and a framework is necessary to handle the aerodynamic and structural coupling. The FlowSimulator which is the current standard within Airbus and DLR is used herein for data handling and driving the aeroelastic simulations [123]. Additional detail on the applied aerodynamic and structural solver are given next.

The aerodynamic equations are solved using the DLR-TAU code [124] of which validations are available in the literature for steady [125] as well as unsteady cases [125,126]. Whereas in [125] limit cycle oscillations of an aeroelastic wing are compared between the TAU code and experimental data with good agreement, in [126] numerical and experimental results are compared for generic gust responses. Time-marching RANS simulations were performed and good agreement has been found for integral values and surface pressure distribution in both validation cases. However, with respect to gust responses further validation might be needed which includes appropriate flight test data to ensure accurate predictions of the herein applied full order model solvers. Nevertheless, all improvements achieved within the underlying FOM solvers will automatically be inherited to the generated ROMs.

As aforementioned this thesis focuses on the RANS equations in conjunction with the Spalart–Allmaras turbulence model [121]. Inviscid fluxes are discretised with a central scheme with the scalar artificial dissipation of Jameson, Schmidt and Turkel [127]. Exact gradients used for viscous and source terms in the turbulence model are computed using the Green–Gauss approach. Steady-state solutions are obtained using the backward Euler method with lower-upper Symmetric–Gauss–Seidel iterations [128] and local time-stepping. Convergence is accelerated applying either 3w or a 2v multigrid scheme based on the case of interest.

As outlined in Section 2.1.2 structural deformations are represented using a modal approach. A modal analysis is performed on the FEM and an appropriate number of modes are considered during coupled simulations. Within industrial simulation cycles the number of retained modes is usually $\mathcal{O}(100)$ and contain all dominant features

such as wing bending and torsion or nacelle deformation, control surface deflections as well as fuselage bending. Note that the coordinate systems describing structural movement in Eq. (2.14) and (2.28) are generally not the same ($\boldsymbol{x} \neq \boldsymbol{x}_s$). Whereas the aerodynamic coordinates $\boldsymbol{x}$ are defined by the CFD grid points, $\boldsymbol{x}_s$ is defined by the FEM discretisation. The coupled Eq. (2.36), however, assumes that there is a connection between both coordinates system. Thus, modal structural excitations X_s are interpolated onto the CFD surface grid in a pre-processing step [129]. Arising volume mesh deformations due to structural deformations are calculated applying the radial basis function method [130].

For coupled time-marching aeroelastic simulations data exchange can either be done on a subiteration level or in a staggered scheme [131]. Within this work the coupled equations are consistently solved using subiterations since larger time-steps are possible without introducing numerical errors but the data exchange needed for each time step is increased. The DLR-TAU code uses a dual time-stepping combined with the second-order backward differentiation formula to integrate the aerodynamic equations in time whereas the structural equations are integrated applying a Beta–Newmark scheme [132]. Computational efficiency of unsteady time-marching simulations for the aerodynamic part is increased using a Cauchy convergence criterion on the change of the drag coefficient if appropriate. Since the structural system is in the order of $\mathcal{O}(100)$ no additional speed up is necessary. Gusts are modelled using the field velocity approach which introduces an artificial mesh velocity [40] during the CFD system solve. The velocity term is added to the governing equations and is prescribed based on the gust excitation while no additional deformation of the computational grid is required. However, the geometric conservation law is fully accounted for which includes velocities arising from the FVM.

Additional detail on forming and solving the aerodynamic LFD system described in Eq. (2.18) is discussed next. While forming of the right-hand side using finite difference is already addressed in-depth in Section 2.1.1.2, also forming of the fluid Jacobian matrix and solving of the linearised system is not trivial and has a significant impact on the computational efficiency. The DLR-TAU follows a first-discretise-then-linearise, matrix-forming approach with an analytical, hand-differentiated fluid Jacobian matrix. This enables efficient computation of the large but sparse matrix also for complex test cases. The interested reader is referred to [73] for a more detailed discussion and the analytical derivation. Even though theoretically various method like directly inverting the system would be possible for solving the large but sparse linear system, this task should not be underestimated for cases of industrial relevance since the number of degrees of freedom scales with the discretisation points. Directly inverting the system Jacobian matrix quickly becomes a memory bottleneck and, thus, a sparse iterative linear solver is consistently used herein. More specifically, a generalised conjugate residual solver with deflated restarting is applied which has shown computational benefits over

the more traditional generalised minimal residual approach [133]. Moreover, for preconditioning a block incomplete lower-upper factorisation of the Jacobian matrix with zero level of fill-in is applied [134].

As part of this work several alterations to the DLR-TAU code were necessary to enable full order model gust analysis. For the LFD method the finite-difference forming of the right-hand side gust forcing term and the assembling of the linearised system was added. Moreover, scripts were generated to efficiently perform the forward and inverse Fourier transform to analyse a-periodic time-domain gust signals. This work has been exchanged with the DLR and is now available as part of the official TAU release. In addition, subiterations for coupled fluid-structure problems have been enabled which needed changes within the FlowSimulator coupling framework as well as directly in the CFD code. These changes have not been fully adopted from the DLR but have been partially included.

Note that the LFD method for gust responses in the DLR-TAU code is currently only implemented for the aerodynamic subsystem. However, an extension towards a fluid-structure coupled system is possible by expanding the Jacobian matrix as shown in Section 2.1.3 but not straightforward. Initial investigations concerning aeroelastic frequency domain gust response analysis for an airfoil have been performed using an in-house code in [135].

2.2 Reduced Order Modelling

Even though the transformation to frequency domain reduces the computational cost for obtaining unsteady loads compared to a time-marching approach, the resulting system is still large. For application in an industrial environment, also a reduction of the spatial dimensions is necessary. Therefore, two reduced order modelling techniques are introduced next. Both reduce the number of degrees of freedom in Eq. (2.14) or Eq. (2.36) significantly by applying either a Galerkin or a Petrov-Galerkin projection. The first method is POD for which modes are computed based on system response samples. The second technique is EMD in which eigenmodes of the coupled system Jacobian matrix are computed and then used for model reduction. Finally, a strategy is outlined to combine both modal sets to investigate coupled aeroelastic responses.

2.2.1 Proper Orthogonal Decomposition

Excellent reviews on POD are published and offer a more in-depth, theoretical description of the method [99, 101]. Here an overview is provided. POD is a modal decomposition technique which extracts modes by optimising the mean square of the variables of interest [77]. A minimal number of modes results from decomposing an ensemble of data trying to capture a predefined amount of energy. Applying POD a

small number of basis vectors is used to represent changes in the state-space variable $\boldsymbol{w}_f$. These basis vectors are also known as empirical eigenfunctions, POD vectors or most commonly POD modes. Deviations in $\boldsymbol{w}_f$ are expressed by a linear combination of modes

$$\Delta \boldsymbol{w}_f = \Phi_{\mathrm{POD}} \boldsymbol{z} \tag{2.41}$$

where Φ_{POD} contains all POD modes which are orthogonal to one another and $\boldsymbol{z}$ denotes the reduced space variable.

Since the size of A is too large for the classical POD method, the method of snapshots is applied instead [98]. Thus, the full order model is analysed at k discrete reduced frequencies by solving Eq. (2.18), while neglecting structural excitations and adjusting the reduced frequency

$$\left(A_{ff} - i\omega_j^* \mathcal{V}\right) \hat{\boldsymbol{w}}_{f,j} = -\frac{\partial \boldsymbol{R}_f}{\partial \boldsymbol{v}_g} \hat{\boldsymbol{v}}_g(\omega_j^*) \quad \text{for} \quad j = 1, \ldots, k \tag{2.18 revisited}$$

Solutions $\hat{\boldsymbol{w}}_{f,j}$ are stored as columns in the snapshot matrix S as

$$S = \left[\hat{\boldsymbol{w}}_{f,1}, \ldots, \hat{\boldsymbol{w}}_{f,k}, \overline{\hat{\boldsymbol{w}}}_{f,1}, \ldots, \overline{\hat{\boldsymbol{w}}}_{f,k}\right] \tag{2.42}$$

together with their corresponding complex conjugates $\overline{\hat{\boldsymbol{w}}}_{f,j}$. It is assumed that entries in the matrix S represent a vector of signals related to the full-order system. The POD basis, also known as Karhunen–Loève basis, minimises the error of approximating an entry in this snapshot matrix using k or less modes. This optimal convergence offered from the Karhunen–Loève basis has been presented in several different publications and the interested reader is referred to the literature [101, 103]. The POD basis

$$\Phi_{\mathrm{POD}} = S\mathrm{V} \tag{2.43}$$

is obtained by maximising the projection of snapshots onto the POD modes, which leads to the eigenvalue problem

$$S^H S \mathrm{v}_j = \mu_j \mathrm{v}_j \quad \text{for} \quad j = 1, \ldots, k \tag{2.44}$$

When $V = [\mathrm{v}_1, \mathrm{v}_2, \ldots, \mathrm{v}_k]$ is scaled for orthonormality, all POD modes need to be divided by $\sqrt{\mu_j}$ to achieve $\Phi_{\mathrm{POD}}^H \Phi_{\mathrm{POD}} = I$. Eigenvalues μ_j are real and positive because $S^H S$ is a Hermitian matrix. The relative information content contributed to the system by a certain mode, also often referred to as energy, is given by

$$r_i = \mu_i \left(\sum_{j=0}^{k} \mu_j \right)^{-1} \quad \text{for} \quad i = 1, \ldots, k \tag{2.45}$$

This can be used to decrease the number of modes further by only considering those with a high relative information content.

Slightly different to Eq. (2.44), also the cell volume can be considered when forming the matrix product,

$$S^H \mathcal{V} S \mathrm{v}_j = \mu_j \mathrm{v}_j \quad \text{for} \quad j = 1, \ldots, k \tag{2.46}$$

Dividing modes by $\sqrt{\mu_j}$ gives $\Phi_{\mathrm{POD}}^H \mathcal{V} \Phi_{\mathrm{POD}} = I$. Including the cell volume during the mode calculation has been suggested in [136] to increase stability of the resulting ROM. The characteristics of the POD model, however, do change. Cells with a small volume become less important resulting in a more global flowfield representation.

The aerodynamic system given in Eq. (2.16) is reduced by substituting Eq. (2.41) and applying a Galerkin projection

$$\Phi_{\mathrm{POD}}^H \Phi_{\mathrm{POD}} \dot{\boldsymbol{z}} = \mathcal{A}_{\mathrm{POD}} \boldsymbol{z} + \Phi_{\mathrm{POD}}^H \mathcal{V}^{-1} \frac{\partial \boldsymbol{R}_f}{\partial \boldsymbol{v}_g} \boldsymbol{v}_g \tag{2.47}$$

where $\mathcal{A}_{\mathrm{POD}} = \Phi_{\mathrm{POD}}^H \mathcal{V}^{-1} A \Phi_{\mathrm{POD}}$ denotes the reduced Jacobian matrix. The term $\Phi_{\mathrm{POD}}^H \Phi_{\mathrm{POD}}$ becomes an identity matrix I due to the applied scaling. If the cell volume is considered when computing POD modes, the reduced system becomes

$$\Phi_{\mathrm{POD}}^H \mathcal{V} \Phi_{\mathrm{POD}} \dot{\boldsymbol{z}} = \mathcal{A}_{\mathrm{POD}} \boldsymbol{z} + \Phi_{\mathrm{POD}}^H \frac{\partial \boldsymbol{R}_f}{\partial \boldsymbol{v}_g} \boldsymbol{v}_g \tag{2.48}$$

with $\mathcal{A}_{\mathrm{POD}} = \Phi_{\mathrm{POD}}^H A \Phi_{\mathrm{POD}}$ and $\Phi_{\mathrm{POD}}^H \mathcal{V} \Phi_{\mathrm{POD}} = I$. Both systems above can be solved rapidly in frequency domain to investigate the response of a rigid airframe under gust excitation. For time-domain analysis, however, the former system tends to become unstable whereas the latter is more likely to be stable [136]. In fact all POD ROMs herein derived from POD modes solving Eq. (2.46) are stable.

2.2.2 Eigenmode Decomposition

The second presented model reduction approach is eigenmode decomposition for which characteristic eigenvalues and corresponding eigenvectors of A are used and is also based on projection. Especially for phenomena where just a few eigenmodes are sufficient to describe the dynamic behaviour of the system, this technique is beneficial compared to proper orthogonal decomposition. The system space is reduced by the EMD to a subspace spanned by eigenvectors instead of approximating a subspace using POD modes. This offers several advantages but also has a few downsides. For POD models, stability of the ROM can not be ensured a-priori, whereas EMD models are inherently stable if the FOM is stable. Moreover, in the context of aeroelasticity, each structural mode of interest results in one or two degrees of freedom in the ROM. In addition, the eigenmode of the coupled aeroelastic system offers insight into the underlying physical behaviour. Even though not discussed in detail in this thesis, the eigenmode tracing

procedure outlined below can be used for bifurcation analysis and thus flutter analysis. More details on this can be found in [137]. One downside is, that constructing a coupled aeroelastic POD basis can be computationally more efficient when comparing the offline model construction process since for the eigenmode tracing individual samples are necessary for all modes. However, this requires a fully coupled formulation which is typically not available for industrially applied CFD solvers.

The mathematical approach for model reduction based on EMD is introduced next and some assumptions for reducing the computational cost are outlined. Right and left eigenvectors $\boldsymbol{\phi}_j$ and $\boldsymbol{\psi}_j$ are calculated by solving the eigenvalue problems

$$A\boldsymbol{\phi}_j = \lambda_j \mathcal{V}\boldsymbol{\phi}_j \quad \text{and} \quad A^T\boldsymbol{\psi}_j = \overline{\lambda}_j \mathcal{V}\boldsymbol{\psi}_j \quad \text{for} \quad j = 1, \ldots, m \tag{2.49}$$

for which the number m is far smaller than the initial system size. Theoretically it is possible to solve the eigenvalue problem above either directly or with a shift-invert method. This becomes computationally prohibitive, if not impossible, for industry relevant cases due to the many million degrees of freedom of the CFD model applied. Considering Eq. (2.40), the coupled direct and adjoint eigenvalue problems can be rewritten as

$$A\boldsymbol{\phi}_j = \begin{bmatrix} A_{ff} & A_{fs} \\ A_{sf} & A_{ss} \end{bmatrix} \boldsymbol{\phi}_j = \lambda_j \mathcal{V}\boldsymbol{\phi}_j \quad \text{for} \quad j = 1, \ldots, m \tag{2.50}$$

$$A^T\boldsymbol{\psi}_j = \begin{bmatrix} A_{ff}^T & A_{sf}^T \\ A_{fs}^T & A_{ss}^T \end{bmatrix} \boldsymbol{\psi}_j = \overline{\lambda}_j \mathcal{V}\boldsymbol{\psi}_j \quad \text{for} \quad j = 1, \ldots, m \tag{2.51}$$

where also the eigenvectors $\boldsymbol{\phi}_j$ and $\boldsymbol{\psi}_j$ are partitioned in fluid and structural contributions. The Schur complement method is used to determine eigenmodes originating from the structural block A_{ss}. This assumes that eigenvalues of A_{ff} are not of interest for the system behaviour. Therefore, the small nonlinear eigenvalue problems can be derived for right and left structural eigenpairs

$$S(\lambda_j)\boldsymbol{\phi}_{s,j} = \lambda_j \boldsymbol{\phi}_{s,j} \quad \text{and} \quad S^T(\lambda_j)\overline{\boldsymbol{\psi}}_{s,j} = \lambda_j \overline{\boldsymbol{\psi}}_{s,j} \tag{2.52}$$

where the matrix $S(\lambda_j)$ is the Schur complement of A_{ff} in A

$$S(\lambda_j) = A_{ss} - A_{sf}(A_{ff} - \lambda_j \mathcal{V})^{-1} A_{fs} \tag{2.53}$$

The first term on the right-hand side of the latter equation, A_{ss}, describes the structural part of the eigenvalue problem whereas the second term, $A_{sf}(A_{ff} - \lambda_j \mathcal{V})^{-1} A_{fs}$, contains the aerodynamic influence on the system. Assuming a modal structural model, the size of the nonlinear eigenvalue problem is small. Note that the diagonal cell volume matrix $\mathcal{V}$ for the aerodynamic system can also be included within the aerodynamic Jacobian matrix by forming its inverse. While the placing of the matrix $\mathcal{V}$ has no influence on the

resulting right eigenvector $\boldsymbol{\phi}_j$, all entries of the left eigensolution $\boldsymbol{\psi}_j$ are also multiplied with the inverse of the cell volume matrix $\mathcal{V}$ if this matrix is included in A_{ff}.

Newton's method is applied to solve Eq. (2.52) using structural frequencies as an initial guess to the eigenvalue [95]. Within each Newton iteration, the aerodynamic influence needs to be evaluated by solving the large aerodynamic system $(A_{ff}-\lambda_j\mathcal{V})^{-1}A_{fs}$. Even though this is possible it quickly becomes computationally inefficient.

Different levels of approximation have been proposed in the past to decrease computational cost using the Schur complement formulation [137]. All of them approximate the aerodynamic influence term $A_{sf}(A_{ff}-\lambda_j\mathcal{V})^{-1}A_{fs}$. The most simplistic way, is to use the linearised frequency domain formulation and sample the aerodynamic influence using an imaginary shift only

$$A_{sf}(A_{ff}-\lambda_j\mathcal{V})^{-1}A_{fs} \approx A_{sf}(A_{ff}-i\omega^*\mathcal{V})^{-1}A_{fs} = Q(\omega^*) \tag{2.54}$$

in a pre-computation step. Note that the matrix $Q(\omega^*)$ is obtained by solving the linear system separately for each mode at all desired reduced frequencies. The system to solve then becomes

$$\Big(A_{ss}-Q(\Im(\lambda_j))\Big)\boldsymbol{\phi}_{s,j} = \lambda_j\boldsymbol{\phi}_{s,j} \tag{2.55}$$

where $\Im(\lambda_j)$ denotes the imaginary part of the traced eigenvalue. During the Newton iteration a surrogate model is used to interpolate between the samples in $Q(\omega^*)$ rather than solving the full aerodynamic system. This approach is closely related to the p-k method used for classical flutter analysis [59]. Similar to the p-method used for flutter investigation, also a complex-valued shift can be used for pre-sampling

$$A_{sf}(A_{ff}-\lambda_j\mathcal{V})^{-1}A_{fs} \approx A_{sf}(A_{ff}-(\sigma+i\omega^*)\mathcal{V})^{-1}A_{fs} = K(\sigma+i\omega^*) \tag{2.56}$$

and during the following tracing procedure

$$\Big(A_{ss}-P(\lambda_j)\Big)\boldsymbol{\phi}_{s,j} = \lambda_j\boldsymbol{\phi}_{s,j}. \tag{2.57}$$

Besides these two aforementioned methods, more complex approaches using Taylor expansions are discussed in some detail in [137] but have not been considered herein.

Whereas the structural entries of $\boldsymbol{\phi}_j$ and $\boldsymbol{\psi}_j$ are readily available after solving Eqs. (2.52), the aerodynamic entries need an additional linear system solve per mode using the eigenvalue as a complex shift

$$(A_{ff}-\lambda_j\mathcal{V})\boldsymbol{\phi}_{f,j} = A_{fs}\boldsymbol{\phi}_{s,j} \tag{2.58}$$

and accordingly for the adjoint solution

$$(A_{ff}^T-\overline{\lambda}_j\mathcal{V})\boldsymbol{\psi}_{f,j} = A_{sf}^T\boldsymbol{\psi}_{s,j} \tag{2.59}$$

Collecting the eigenvectors, the right and left modal matrices are formed as

$$\Phi_{\mathrm{EMD}} = \left[\boldsymbol{\phi}_1, \ldots, \boldsymbol{\phi}_m, \overline{\boldsymbol{\phi}}_1, \ldots, \overline{\boldsymbol{\phi}}_m\right] \quad \text{and} \quad \Psi_{\mathrm{EMD}} = \left[\boldsymbol{\psi}_1, \ldots, \boldsymbol{\psi}_m, \overline{\boldsymbol{\psi}}_1, \ldots, \overline{\boldsymbol{\psi}}_m\right] \tag{2.60}$$

Eigensolutions originating from the structure appear as complex conjugate pairs and these complex conjugates are added to the modal basis at no additional cost. Furthermore, the eigenvectors are normalised to fulfil the biorthonormality condition

$$\Psi_{\mathrm{EMD}}^H \mathcal{V} \Phi_{\mathrm{EMD}} = I \tag{2.61}$$

The system can than be reduced by expressing changes in the state-space variable $\Delta \boldsymbol{w}$ as a linear combination of modes

$$\Delta \boldsymbol{w} = \Phi_{\mathrm{EMD}} \boldsymbol{z} \tag{2.62}$$

A Petrov–Galerkin projection is applied on Eq. (2.37) using the EMD modes and accounting for the normalisation in Eq. (2.61)

$$\dot{\boldsymbol{z}} = \mathcal{A}_{\mathrm{EMD}} \boldsymbol{z} + \Psi_{\mathrm{EMD}}^H \frac{\partial \boldsymbol{R}}{\partial \boldsymbol{v}_g} \boldsymbol{v}_g \tag{2.63}$$

with $\mathcal{A}_{\mathrm{EMD}} = \Psi_{\mathrm{EMD}}^H A \Phi_{\mathrm{EMD}}$ as reduced Jacobian matrix. This reduces the initial semi discrete ODE with many millions degrees of freedom to an ODE with $\mathcal{O}(100)$ degrees of freedom which can be analysed rapidly on a local desktop computer.

Since the bi-modal basis applied contains left and right eigenvectors of the full order Jacobian matrix A, the reduced matrix $\mathcal{A}_{\mathrm{EMD}}$ is equal to the diagonal matrix Λ which contains the computed eigenvalues. If Eq. (2.52) is not solved directly since an approximation of the aerodynamic influence is applied to reduce computational cost, the obtained eigenvalues are no longer exact eigenvalues of A. However, comparing $\mathcal{A}_{\mathrm{EMD}}$ with Λ the quality of the approximation can be investigated. Computational cost for forming the EMD ROM can be further decreased by assuming $\mathcal{A}_{\mathrm{EMD}} = \Lambda$, since forming and projecting the large, full order Jacobian matrix can be omitted.

Within the fluid dynamics community the analysis of the initial value problem besides the eigenvalue problem has been identified to be substantial to fully describe the system response behaviour [77, 138]. Due to the non-normal nature of the fluid Jacobian matrix A_{ff}, which gets emphasised within the coupled fluid-structure case because of A_{fs} and A_{sf}, eigenfunctions of A are nonorthogonal. Thus the short- and long-term temporal behaviour might significantly differ [139]. Whereas the long-term system response is governed by the decay rate of the least stable eigenfunction, the short-term response can be analysed utilizing the initial value problem and reveals information about the transient energy growth behaviour, also known as peaking within the control community [140]. As a good starting point for nonmodal stability analysis

the interested reader is referred to [139]. Note that, so far results have been presented for cases with significantly smaller length- and time-scales as well as Reynolds numbers than the herein investigated examples. Thus, extending the eigenmode based response analysis pursued herein towards a transient growth analysis will increase the knowledge-base further and push reduced order modeling as well as transient growth analysis another step forward. Moreover, the adjoint solutions for eigenmodes of interest are also already compute for the projection of the ROM.

2.2.3 Combined Model Basis

An aeroelastic ROM is constructed to investigate the influence of gust excitation on flexible structures by unifying the two, just introduced, bases as

$$\Phi = [\Phi_{\mathrm{POD}}\ ,\ \Phi_{\mathrm{EMD}}] \quad \text{and} \quad \Psi = [\Psi_{\mathrm{POD}}\ ,\ \Psi_{\mathrm{EMD}}] \tag{2.64}$$

where $\Psi_{\mathrm{POD}} = \Phi_{\mathrm{POD}}$. Only the aerodynamic subsystem is considered to identify Φ_{POD} and thus all POD modes are padded with zero entries in the structural part to match the dimension of the coupled system.

Describing the change in state-space vector $\Delta\boldsymbol{w}$ by a linear combination of unified modes as before

$$\Delta\boldsymbol{w} = \Phi\boldsymbol{z} \tag{2.65}$$

and substituting in Eq. (2.16), gives after performing a Petrov–Galerkin projection

$$\Psi^H\mathcal{V}\Phi\dot{\boldsymbol{z}} = \Psi^H A\Phi\boldsymbol{z} + \Psi^H\frac{\partial\boldsymbol{R}}{\partial\boldsymbol{v}_g}\Delta\boldsymbol{v}_g \tag{2.66}$$

The reduced Jacobian matrix $\Psi^H A\Phi$ can be dissected into terms originating from the initial POD and EMD models as well as additional coupling terms as

$$\Psi^H A\Phi = \begin{bmatrix} \mathcal{A}_{\mathrm{POD}} & \mathcal{A}_{\mathrm{coupling,1}} \\ \mathcal{A}_{\mathrm{coupling,2}} & \mathcal{A}_{\mathrm{EMD}} \end{bmatrix} \tag{2.67}$$

Whereas the diagonal matrices are equivalent to the aforementioned reduced matrices of both initial ROMs the coupling terms are resulting from the gust and structure interaction. In contrast to the EMD ROM in which the reduced Jacobian matrix could be approximated using the diagonal matrix Λ the unified formulation inherently needs forming and projecting of A since the aerodynamic and coupling terms are not a-priori known.

Since biorthonormality is no longer fulfilled for the coupled model ($\Psi^H\mathcal{V}\Phi \neq I$) an additional step is performed to the system. Even though strickly speaking not necessary this conversion enables the usage of standard time-domain solution techniques. The left modal matrix Ψ is pre-multiplied with the inverse of $\Psi^H\mathcal{V}\Phi$. The resulting time-domain

representation of the coupled reduced system is

$$\dot{\boldsymbol{z}} = \mathcal{A}\boldsymbol{z} + (\Psi^H \mathcal{V} \Phi)^{-1} \Psi^H \frac{\partial \boldsymbol{R}}{\partial \boldsymbol{v}_g} \Delta \boldsymbol{v}_g \tag{2.68}$$

where $\mathcal{A} = (\Psi^H \mathcal{V} \Phi)^{-1} \Psi^H A \Phi$. While multiplying with the inverse changes the projection based on Ψ, the reduction described by Φ remains unchanged. This technique results in a small ROM which can be used to investigate coupled aeroelastic gust responses in a rapid fashion.

2.2.4 Practical Implementation Details

This section will focus on practical implementation aspects of the reduced order modelling approaches. As already discussed for the FOM the aerodynamic and structural systems are solved only loosely coupled during time-marching and LFD analysis which creates some challenges for the coupled ROM construction. As for the LFD method, fluid Jacobian matrix A_{ff} is provided from the DLR-TAU and additional details are given in Section 2.1.4. The coupling block A_{fs} is computed using central finite differences for each structural 'in-vacuum' mode of interest whereas the matrix A_{sf} is analytically formed. The structural matrix A_{ss} is trivial since a modal decomposition of the structural system has been performed initially and is used as starting point. Whereas the Galerkin projection for the aerodynamic POD based ROM is straightforward using only the fluid subsystem, the Petrov-Galerkin projection is performed stepwise by first projecting each subblock of the matrix A and then second combining them for a fully coupled aeroelastic ROM.

Moreover, during the ROM construction the reduction of gust influence terms is needed. This includes the matrix $\partial \boldsymbol{R}/\partial \boldsymbol{v}_g$ in Eq. (2.68). While for the LFD solves, the explicit construction can be avoided using a finite differencing approach with a known gust shape vector, for the ROM the matrix is formed explicitly. Since an analytical derivation is not available, a sweep of central finite-differences of the form

$$-\frac{\partial \boldsymbol{R}}{\partial \boldsymbol{v}_g} = \frac{\partial \boldsymbol{R}}{\partial \dot{\boldsymbol{x}}} = \frac{\boldsymbol{R}_f(\boldsymbol{w}_0, \boldsymbol{x}_0, \dot{\boldsymbol{x}}_0, \boldsymbol{v}_{g0} + \varepsilon \dot{\boldsymbol{x}}) - \boldsymbol{R}_f(\boldsymbol{w}_0, \boldsymbol{x}_0, \dot{\boldsymbol{x}}_0, \boldsymbol{v}_{g0} - \varepsilon \dot{\boldsymbol{x}})}{2\varepsilon} \tag{2.69}$$

is used. Computational cost is reduced by disturbing grid-point velocities $\dot{\boldsymbol{x}}$ of all points that are neither first nor second neighbour of another disturbed point. The set of disturbed points defines the columns of the matrix, whereas the resulting non-zero residual entries define the rows. This approach follows a graph coloring which is available for example in [141] and has also been applied for evaluating the Jacobian and Hessian matrix [142]. For a second-order accurate scheme this procedure is demonstrated on a Cartesian grid in Fig. 2.7. Following a first finite-difference evaluation shown in Fig. 2.7(a), a new set of, as yet undisturbed, grid points is selected. This

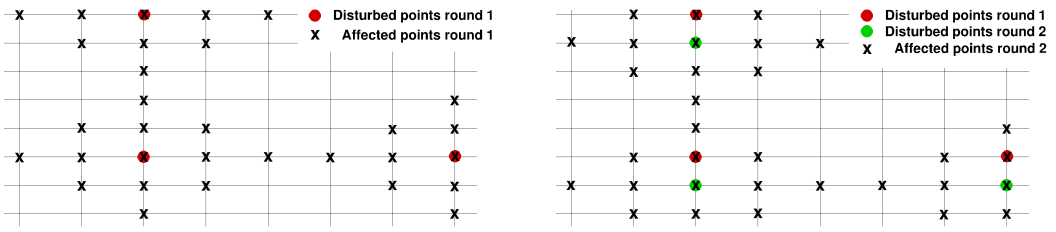

(a) First finite-difference evaluation

(b) Second finite-difference evaluation

Figure 2.7: Demonstration of finite-difference approach for forming $\partial \mathbf{R}/\partial \boldsymbol{v}_\mathrm{g}$

procedure is repeated until all points have been disturbed once. Even though the procedure is demonstrated using a Cartesian grid, the computational grids of all test cases presented herein are hybrid. Depending on the partitioning applied, $\mathcal{O}(50)$ and $\mathcal{O}(200)$ finite-difference evaluations are required to construct the full matrix for the aerofoil and aircraft test cases, respectively. This implementation can easily be adjusted for lateral gusts by perturbing the y-velocity instead of the z-velocity. Combined lateral and vertical excitations are then simulated using linear superposition.

Since a linear Taylor expansion is used, the assumption of a dynamically linear response also extends to integrated quantities, such as lift and moment coefficient. Thus, changes in global coefficients, e.g. change in lift coefficient ΔC_L, can be computed by forming the partial derivative $\partial C_L/\partial \boldsymbol{w}$ using steady state information only and then substituting with Eq. (2.65)

$$\Delta C_L = \frac{\partial C_L}{\partial \boldsymbol{w}} \Delta \boldsymbol{w} = \frac{\partial C_L}{\partial \boldsymbol{w}} \Phi \boldsymbol{z} = \frac{\partial C_L}{\partial \boldsymbol{w}_f} \Phi_f \boldsymbol{z}_f + \frac{\partial C_L}{\partial \boldsymbol{w}_s} \Phi_s \boldsymbol{z}_s \tag{2.70}$$

This enables the analysis of global coefficients without the need of reconstructing the surface solution from the ROM data. This formulation accounts for changes in global coefficients due to aerodynamic as well as structural degrees of freedom.

Needed infrastructure for the ROM analysis were created within this work. This includes the projection of the system Jacobian matrix, the computation and projection of the gust influence matrix, the projection of linearised coefficient responses as well as an overall python-based framework to efficiently handle the different datasets. The created ROM framework can be used to generate and solve either aerodynamic or aeroelastic ROMs conveniently. Especially the forming of the POD and EMD basis has been eased and a facility to combine both modal sets has been programmed. Moreover, post-processing functions have been created to reconstruct FOM results for global coefficients, instantaneous surface pressure and full flowfield solutions.

2.3 Summary on Theoretical Formulation

The theoretical formulations for the full and reduced order models are derived in this chapter. Computational aerodynamic modelling is discussed introducing the Reynolds-averaged Navier–Stokes equations. The system is transferred in frequency-domain after applying a first-order Taylor expansion. The gust induced right-hand side forcing term is focused on next and an analytical derivation is given. The reconstruction of aperiodic time-domain signals, as the key strength of the frequency-domain method, is exemplified. A discrete frequency response function can be computed once by solving the linearised system at several reduced frequencies. Afterwards, a large number of different aperiodic signals can be analysed applying an incomplete inverse Fourier transform. This significantly reduces the computational cost compared to an unsteady time-marching simulation while assuming dynamically linear behaviour. Next, a modal structural formulation is outlined and a coupled aeroelastic system is derived.

In the second part two projection based model reduction techniques, namely proper orthogonal decomposition and eigenmode decomposition, are introduced to reduce the spatial degrees of freedom. Details are given on how to generate a stable time-domain model for proper orthogonal decomposition by considering the cell volume of the CFD formulation. For the eigenmode decomposition model different ideas on how to approximate the aerodynamic influence on the coupled eigenvectors are briefly discussed. Finally, both modal bases are combined and used for a Petrov–Galerkin projection. The resulting small sized system can be utilised to rapidly analyse aeroelastic gust response problems on a local desktop machine.

Chapter 3

Linearised Gust Aerodynamics

The herein proposed time-linearised method, also known as linearised frequency-domain (LFD) method, for gust response simulations is verified in this chapter analysing sinusoidal and aperiodic gust responses for an aerofoil and a large civil aircraft. Derivatives of aerodynamic coefficients and complex-valued surface pressures are compared for time- and frequency-domain approaches at several reduced frequencies. Aperiodic gust excitations, specifically 1-cos gusts, are investigated using an incomplete inverse Fourier transform.

In Section 3.1 results are presented for three different aerofoil test cases including a post-buffet, detached-flow case. In Section 3.2 an industry-relevant aircraft configuration is investigated. After the verification, the techniques are applied to conditions arising from certification requirements to demonstrate the technical readiness. Computational cost is quantified to discuss the efficiency gain of the time-linearised method compared to an unsteady time-marching simulation. Finally, the influence of dynamic non-linearities occurring while analysing aforementioned conditions is outlined. The majority of results presented in this chapter has been published in [116].

Whereas forced-motion simulations using linearised CFD are already established and attracted industrial interest, the herein presented gust response method would enable industry to completely replace DLM based processes for unsteady aerodynamic loads in a straightforward fashion. Necessary loads can be computed in frequency domain and used at various stages of the aircraft design and certification process without major changes in the process chain.

A schematic representation of the LFD method for gust response simulations is given in Fig. 3.1. The LFD method, in contrast to a time-marching method, can be split in two stages. First, the system is analysed for sinusoidal gust excitations by solving Eq. (2.18) at several reduced frequencies. This is computationally expensive since a large but sparse linear system of equations needs to be analysed. Therefore it is typically done on a high performance computing system and it is referred to as offline stage. During the offline phase the Jacobian matrix A_{ff} which is independent of gust

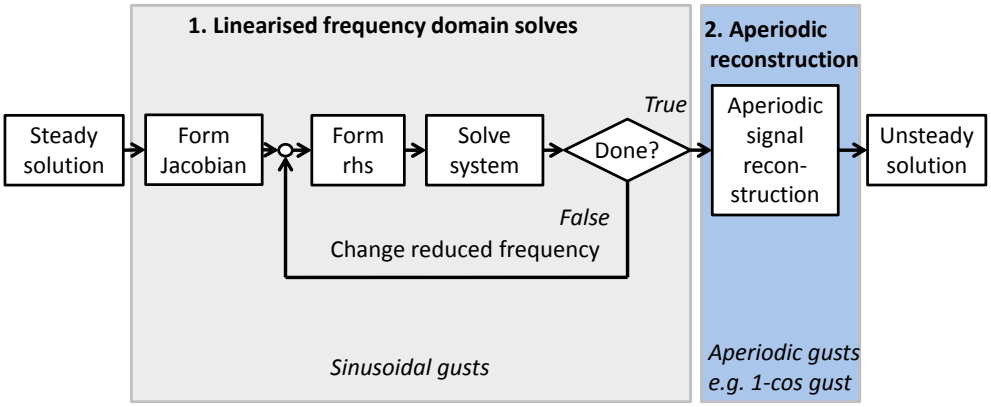

Figure 3.1: Schematic representation of linearised frequency-domain method

excitations is formed, the right-hand side gust forcing term is computed using finite differences and the resulting large but sparse linear system is solved. Secondly, these sinusoidal gust responses are utilised to investigate aperiodic time-domain signals such as 1-cos gusts, as discussed in Section 2.1.1.3. Since only the weighting coefficients need to be computed the aperiodic reconstruction can be done rapidly on a local computing system and is also known as online stage.

3.1 NACA0012 Aerofoil Cases

Results are presented for a NACA0012 aerofoil using a mesh consisting of 70,000 grid points with a first wall-normal spacing of one or less in wall units throughout. The whole computational domain with a farfield distance of 45 chord lengths is shown in Fig. 3.2(a). In Fig. 3.2(b), structured boundary layer cells around the leading edge are displayed. Two attached-flow cases (case 1 and 2) and one post-buffet, detached-flow case (case 3) are investigated with a constant Reynolds number of 10 million. Mach number and angle of attack are summarised in Tab. 3.1. The grid requirements are based on the most challenging test case 3 such that the change in steady lift coefficient is below 0.1% when further refining the mesh. Case 1 and 2 have been performed with the same mesh to ensure consistency even though a coarser resoluation might have been possible to fulfil the same lift convergence criterion.

The unsteady time-domain solver settings applied are shown in Tab. 3.2 and additional details are presented in the Section 2.1.4. For the investigation of sinusoidal excitations, the unsteady time-step size is chosen indirectly by defining the number

Table 3.1: Flow conditions of NACA0012 aerofoil cases

test case	Mach number	angle of attack (deg)
case 1	0.3	0.0
case 2	0.8	0.0
case 3	0.8	3.0

Table 3.2: Time-domain numerical parameters of aerofoil cases

	excitation	cases 1 & 2	case 3
Abort density residual	all	10^{-3}	10^{-5}
Cauchy convergence criterion	all	✓	×
Multigrid-cycle scheme	all	3w++	sg
Time-steps per period	sine	64	128
Number of periods	sine	10	15
Time-step size	1-cos	0.02	0.02
Number of time-steps	1-cos	3000	3000
Time-step size	pulse	0.01	0.01
Number of time-steps	pulse	12000	12000

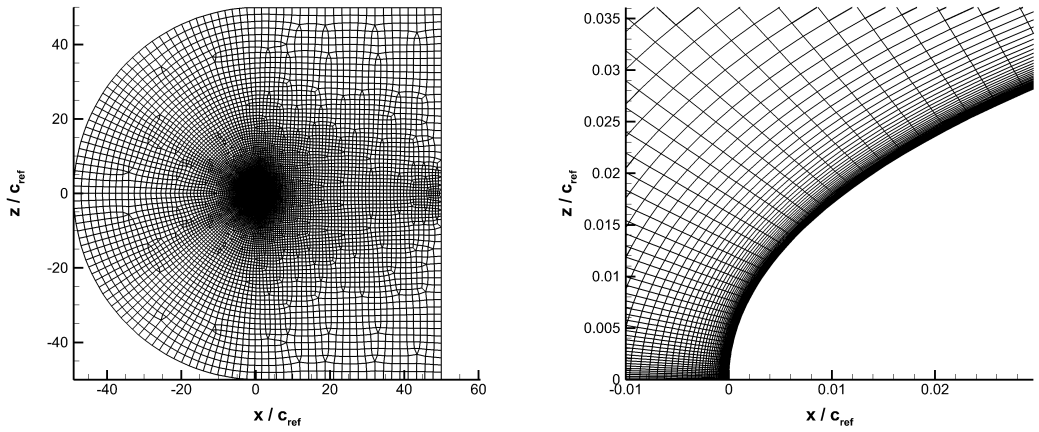

(a) Whole computational domain

(b) Boundary layer resolution

Figure 3.2: Computational grid of aerofoil cases

of steps per period. Analysing 1-cos gust excitations, time-step size and number of time steps follow from preliminary numerical experiments to ensure an error in the lift coefficient value below 1% at all time-steps. For pulse excitations the number of steps is increased by a factor of four with the time-step size halved compared with 1-cos excitations. When a Cauchy convergence criterion is applied, a tolerance of 10^{-8} for the relative error of the drag coefficient is used since this coefficient is more sensitive than the lift coefficient. In addition, an abort criterion based on the density residual is applied thoughout.

Table 3.3: Frequency-domain numerical parameters of aerofoil cases

	cases 1 & 2	case 3
Number of Krylov vectors	30	40
Number of deflation vectors	10	15
Abort density residual	10^{-8}	10^{-8}

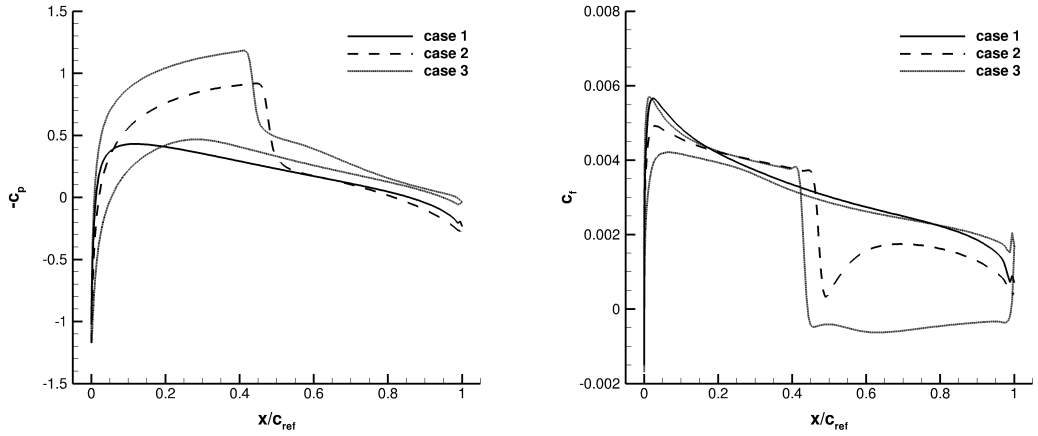

(a) Surface pressure distribution

(b) Skin-friction distribution

Figure 3.3: Steady-state surface pressure and skin-friction distributions for aerofoil cases. (case 1: $M = 0.3$, $\alpha_0 = 0°$, $Re = 10e^6$, case 2: $M = 0.8$, $\alpha_0 = 0°$, $Re = 10e^6$, case 3: $M = 0.8$, $\alpha_0 = 3°$, $Re = 10e^6$)

Linear systems are solved using a generalised conjugate residual solver with deflated restarting and further details are given in Section 2.1.4. The linear convergence criteria applied to the density residual as well as the number of Krylov and deflation vectors used are given in Tab. 3.3. The higher number of vectors for aerofoil case 3, compared to cases 1 and 2, accounts for the increased stiffness of the linear system caused by the substantial shocked-induced separation. Note that this increases the memory needed for solving the system but not necessarily the runtime.

Steady-state surface pressure distributions for all cases are shown in Fig. 3.3(a) after converging the density residual to machine precision. Case 1 is purely subsonic and thus the large suction area around the leading edge dominates the flow topology. In contrast, both transonic-flow cases (case 2 and 3) contain a strong shock at roughly 45% chord length. In case 3 the shock causes the flow to detach, resulting in a negative skin friction coefficient from the shock foot to the trailing edge as presented in Fig. 3.3(b).

3.1.1 Periodic Sinusoidal Gust Excitation

The LFD method is verified at several reduced frequencies by comparing frequency response functions of the lift coefficient to equivalent time-domain (TD) results. Instead

of producing TD solutions separately for each frequency of interest by analysing individual sinusoidal excitations, a pulse signal is used to excite all relevant frequencies during one unsteady time-marching simulation. A Fourier transform of the resulting unsteady lift coefficient is performed and complex-valued Fourier coefficients are weighted by the Fourier transform of the pulse excitation signal. A dynamically linear response is ensured by setting the gust excitation velocity v_{gz} to 0.001% of the freestream velocity. The finite-difference step-size for the evaluation of the right-hand side term is set to $\varepsilon = 0.0001$. Nearly perfect agreement between both simulation methods is observed throughout for real and imaginary parts as well as magnitude and phase as seen in Fig. 3.4. Real and imaginary parts for both attached-flow cases show only positive values in the investigated frequency range, whereas a change of sign in the real part and a maximum in the imaginary part is present for case 3 at a reduced frequency of about 0.5. This behaviour causes a change in sign of the phase while the magnitude exhibits a peak at this reduced frequency. Similar behaviour has been presented for forced-motion simulations close to the buffet onset [91, 143, 144].

Complex-valued surface pressure distributions for all three aerofoil cases obtained from LFD simulations are compared with their corresponding TD counterparts in Fig. 3.5 for a randomly chosen reduced frequency of 0.2. Results from TD are produced applying a Fourier transform to the instantaneous surface pressures, omitting the initial transient response. All values are normalised by the gust excitation amplitude. The harmonic change in gust velocity can be seen as a local change in angle of attack throughout the flow field. Note that in contrast to a pitching movement the change in angle of attack at, for example, the leading and trailing edge is not the same and depends on the investigated gust length. As expected from a change in angle of attack, maximum responses in the subsonic case are located around the leading edge in real as well as imaginary parts and excellent agreement between both simulations is observed in Figs. 3.5(a) and 3.5(b). For case 2 the highest amplified region is around the shock location, as shown in Figs. 3.5(c) and 3.5(d) for real and imaginary parts correlating to the dominating physical behaviour, which is a downstream shock motion with increasing angle of attack. In contrast to case 2, the NACA0012 aerofoil in case 3 exhibits an inverse shock motion which means that with increasing angle of attack the shock is moving upstream since the area of shock induced separation is increasing. In the complex-valued surface pressure plots this can be seen in the change of sign for the imaginary part around the shock location. Even though, looking at the steady and unsteady behaviour in combination, this is a highly non-linear phenomenon, the dynamical contribution to it is purely linear. Thus coinciding results are achieved as visualised in Figs. 3.5(e) and 3.5(f) and demonstrate the validity of the method even in severe flow situations if a purely dynamically linear response is investigated.

The amplitude of the lift coefficient over gust amplitude is shown in Fig. 3.6. The TD responses consider the first harmonic only and are normalised using the linearised

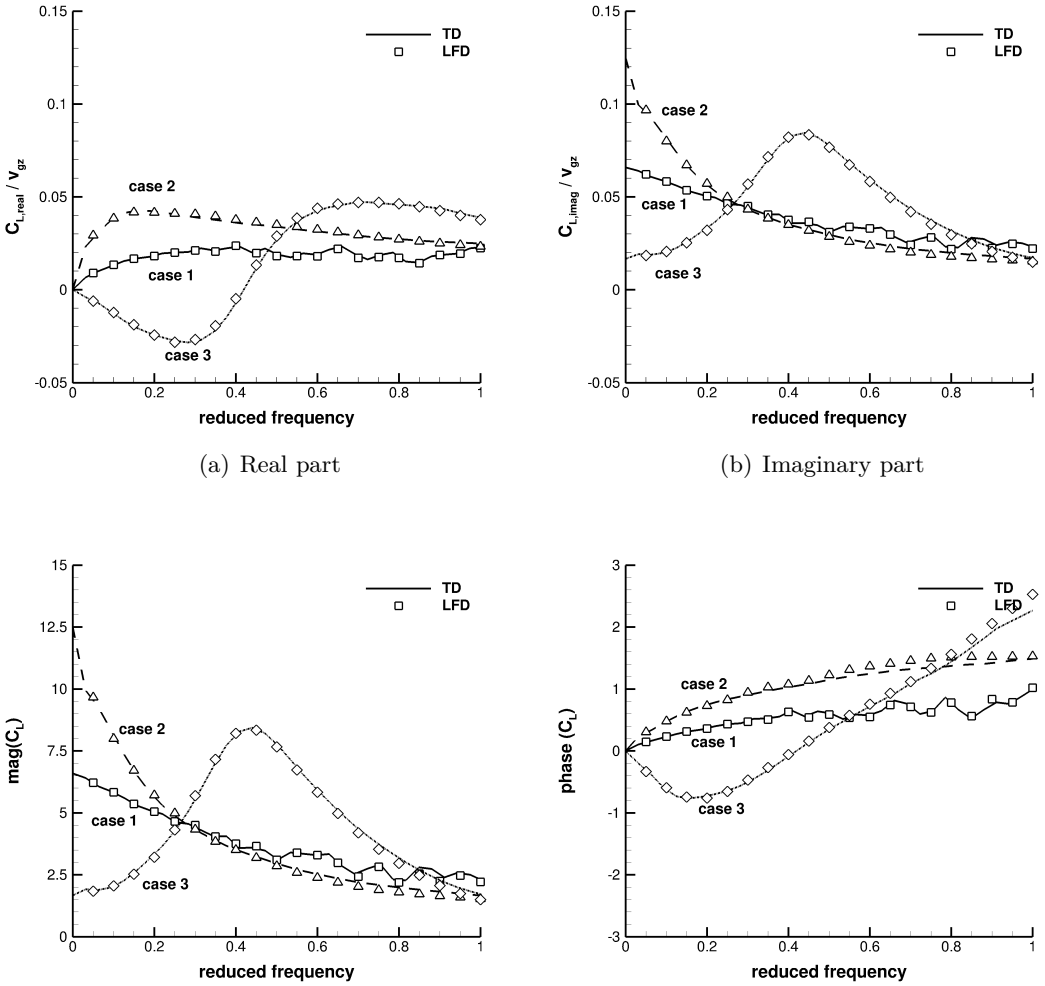

(a) Real part

(b) Imaginary part

(c) Magnitude

(d) Phase

Figure 3.4: Frequency response functions of lift coefficient for aerofoil cases. (case 1: $M = 0.3$, $\alpha_0 = 0°$, $Re = 10e^6$, case 2: $M = 0.8$, $\alpha_0 = 0°$, $Re = 10e^6$, case 3: $M = 0.8$, $\alpha_0 = 3°$, $Re = 10e^6$)

response. Naturally, a constant line is obtained from the LFD approach whereas non-linear time-marching solutions start to differ with increasing gust amplitude. These differences are a measure of non-linearity induced by the gust amplitude. For all cases, results overlap for very small gust amplitudes, demonstrating that the linearised method is capable of fully reproducing dynamically linear responses regardless of non-linearities in the steady-state solution. With increasing amplitude of gust excitation, the resulting magnitude of the lift coefficient decreases in cases 1 and 3, while for the transonic attached-flow case 2 no significant drop is observed. Once amplitudes are high enough to cause either significant shock movement or separation, the unsteady lift increases in cases 1 and 2. In case 3 on the other hand, the separation area grows with higher gust

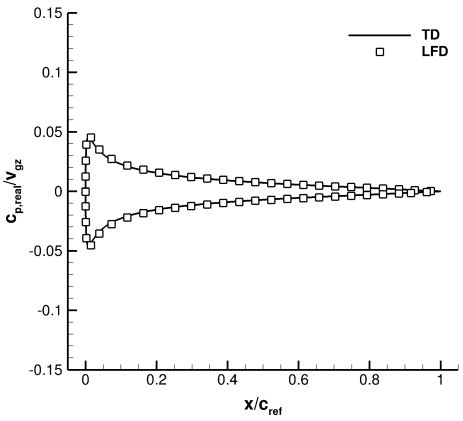

(a) Real part case 1
$M = 0.3$, $\alpha_0 = 0°$, $Re = 10e^6$

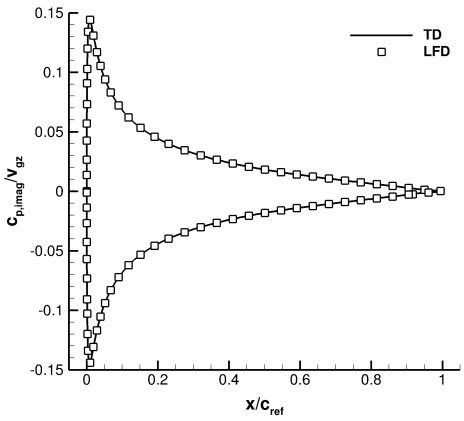

(b) Imaginary part case 1
$M = 0.3$, $\alpha_0 = 0°$, $Re = 10e^6$

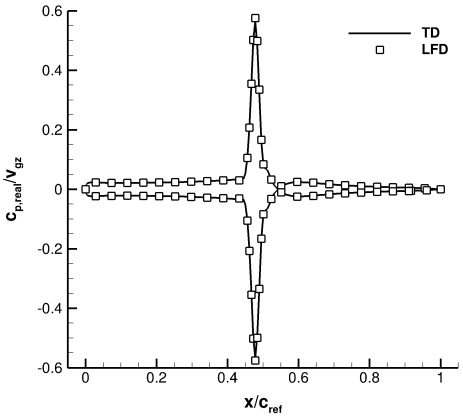

(c) Real part case 2
$M = 0.8$, $\alpha_0 = 0°$, $Re = 10e^6$

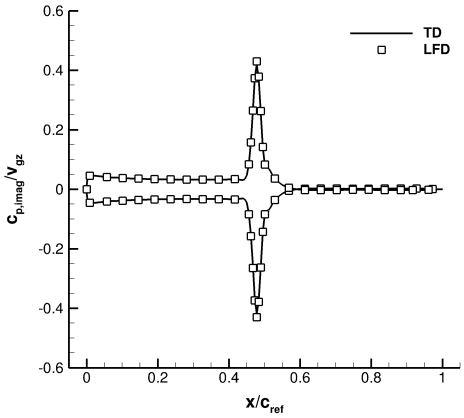

(d) Imaginary part case 2
$M = 0.8$, $\alpha_0 = 0°$, $Re = 10e^6$

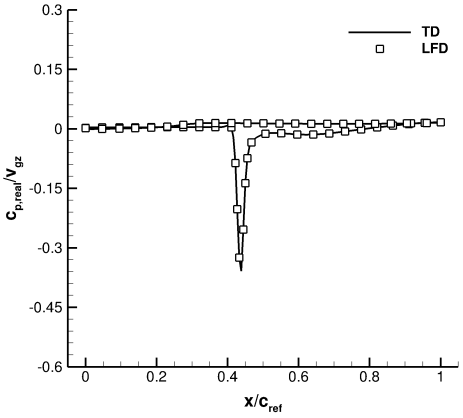

(e) Real part case 3
$M = 0.8$, $\alpha_0 = 3°$, $Re = 10e^6$

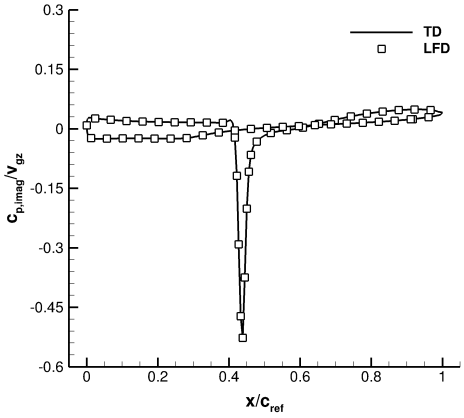

(f) Imaginary part case 3
$M = 0.8$, $\alpha_0 = 3°$, $Re = 10e^6$

Figure 3.5: Complex-valued surface pressure coefficients for sinusoidal gust at $\omega^* = 0.2$

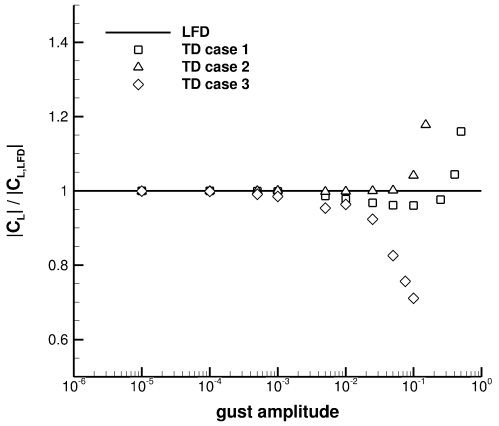

Figure 3.6: Amplitude of lift coefficient over gust amplitude for sinusoidal gust with $\omega^* = 0.2$. (case 1: $M = 0.3$, $\alpha_0 = 0°$, $Re = 10e^6$, case 2: $M = 0.8$, $\alpha_0 = 0°$, $Re = 10e^6$, case 3: $M = 0.8$, $\alpha_0 = 3°$, $Re = 10e^6$)

amplitudes and thus generated lift is reduced. For amplitudes higher than the once shown the time-domain method was no longer able to converge to a solution using the applied numerical settings.

In terms of computational cost, one individual frequency-domain solve is between one to two orders of magnitude faster than the corresponding sinusoidal non-linear time-marching solution for both attached-flow cases. While unsteady time-marching simulations are highly sensitive to the investigated flow topology, resulting in increased computational cost at severe flow conditions, the frequency-domain approach is much less sensitive provided a robust linear solver is applied. Indeed, even higher time-saving factors are achieved for case 3 in the range of three to four orders of magnitude. This is mainly related to the increased number of inner iterations necessary at each time step to ensure a sufficient convergence of the density residual. Note that a robust linear solver is necessary to solve linear system at severe flow conditions efficiently and performance will be different if a more simplistic approach than the herein used generalised conjugate residual solver with deflated restarting is applied.

3.1.2 Aperiodic 1-cos Gust Excitation

Responses to aperiodic 1-cos gust excitations are obtained by an incomplete inverse Fourier transform of several discrete frequency-domain results in conjunction with a complex-valued weighting function as outlined in Section 2.1.1.3. The influence of the reduced frequencies, retained during the inverse Fourier transform, is analysed first. Time-domain signals and their corresponding frequency-domain counterparts for different gust lengths are shown in Fig. 3.7. With decreasing gust length the affected

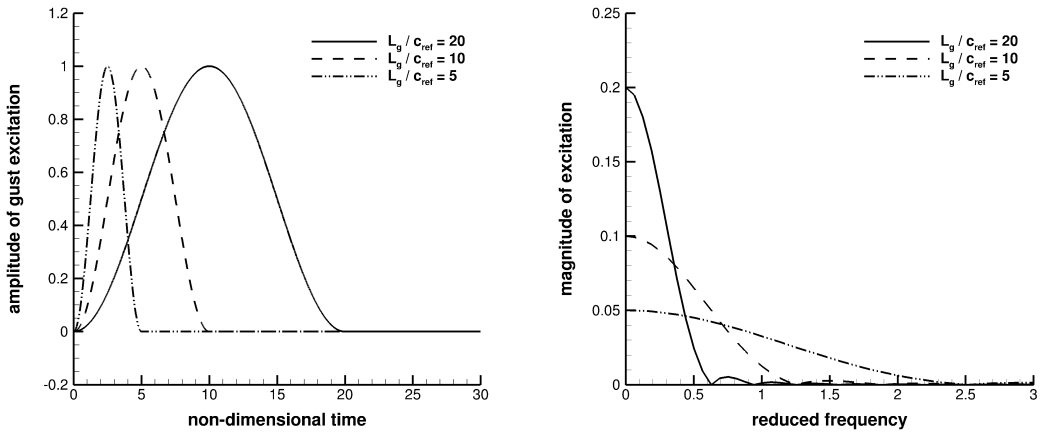

(a) Time-domain representation

(b) Frequency-domain representation

Figure 3.7: Time- and frequency-domain representation for three different gust lengths

frequency range increases and thus differently spaced and/or more samples are necessary.

Detailed results for two different gust lengths for case 1 with a constant gust amplitude of 1% of the freestream velocity are shown in Fig. 3.8. With the spacing kept constant at $\Delta\omega^* = 0.0648$ and sampling always starting at $\omega^* = 0$, the number of frequencies n_{ω^*} is analysed for 15, 30 and 45 samples. For the shorter gust length, a higher number of frequency-domain results is necessary to accurately predict loads since higher frequencies are important, whereas with increasing gust length the relevant frequency range is reduced. Thus, 45 equally spaced reduced frequencies are needed for $L_\mathrm{g}/c_\mathrm{ref} = 5$ to achieve an error

$$\frac{\Delta C_{L,LFD,max} - \Delta C_{L,TD,max}}{\Delta C_{L,TD,max}} \tag{3.1}$$

below 1%. This number decreases to 15 for $L_\mathrm{g}/c_\mathrm{ref} = 20$ for a similar error when comparing time-marching and LFD results.

The influence of the step size $\Delta\omega^*$ is analysed next. The number of frequencies is kept constant at 15 while the step size is varied using $\Delta\omega^* = 0.0648$, 0.1296 and 0.1944. Results for case 1 are shown in Fig. 3.9. For $\Delta\omega^* = 0.0648$ results are equivalent to the aforementioned ones with good agreement only for the longer gust. With increasing step size, the relative error on the maximum lift coefficient decreases for $L_\mathrm{g}/c_\mathrm{ref} = 5$ while the opposite effect is observed for $L_\mathrm{g}/c_\mathrm{ref} = 20$. Whereas the relative error for the short gust with a step size of $\Delta\omega^* = 0.1944$ drops below 1%, a deviation of around 3% is obtained for the longer gust since the low frequency range needed for longer gusts is underrepresented. All subsequent results are produced using 45 frequencies, $\omega_0^* = 0$ and a spacing of $\Delta\omega^* = 0.0648$ to accurately predict loads for a wide range of gust

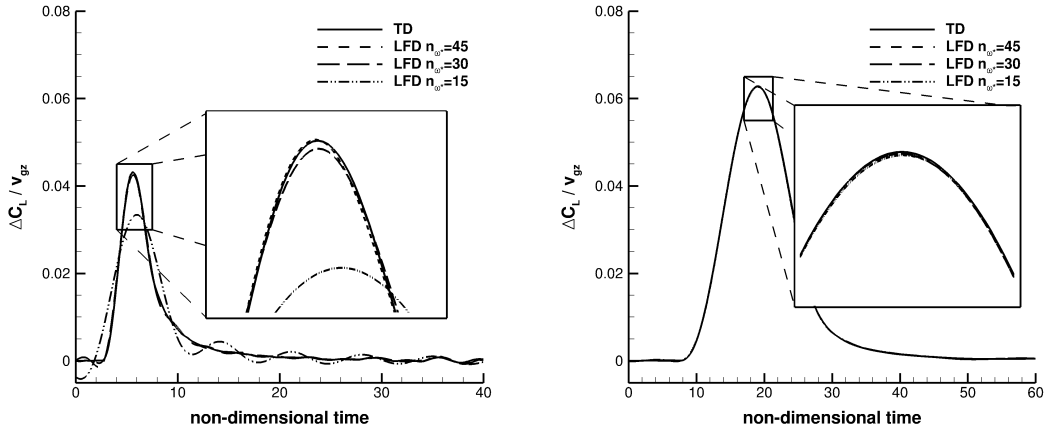

(a) $L_g/c_{ref} = 5$ (b) $L_g/c_{ref} = 20$

Figure 3.8: Change in lift coefficient scaled by gust amplitude due to 1-cos gusts for case 1 with varying numbers of retained frequencies. The spacing is kept constant at $\Delta\omega^* = 0.0648$. $M = 0.3$, $\alpha_0 = 0°$, $Re = 10e^6$

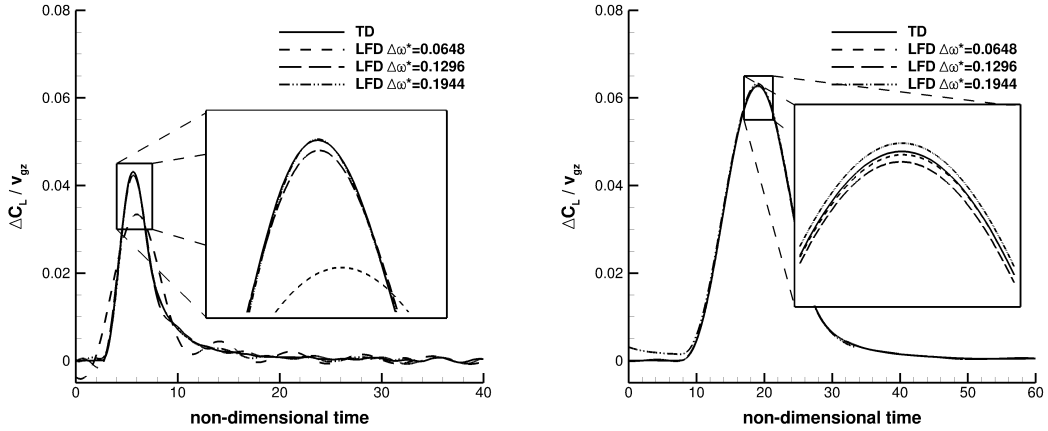

(a) $L_g/c_{ref} = 5$ (b) $L_g/c_{ref} = 20$

Figure 3.9: Change in lift coefficient scaled by gust amplitude due to 1-cos gusts for case 1 with varying frequency spacing. $M = 0.3$, $\alpha_0 = 0°$, $Re = 10e^6$

lengths. However, the choices of ω_0^*, $\Delta\omega^*$ and n_{ω^*} highly depend on the aperiodic gust of interest analysed afterwards. While herein presented values show excellent agreement for 1-cos gusts, the analysis of a different excitation signal might result in different sampling strategy. Moreover, if an infinite range of reduced frequencies is necessary to accurately capture the time-domain behaviour, the frequency-domain method might still be possible but less efficient.

LFD responses for the two other cases are shown in Fig. 3.10 in comparison to the corresponding unsteady time-marching results for non-dimensional gust lengths of

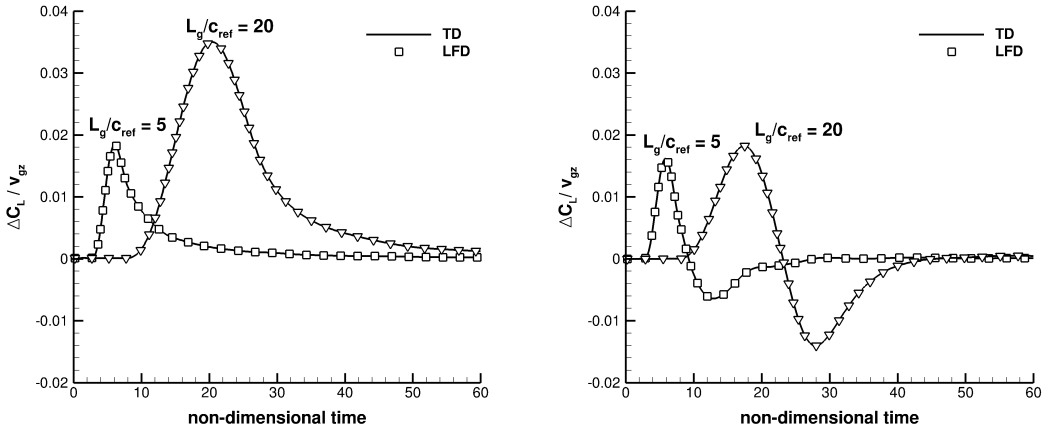

(a) case 2 $M = 0.8$, $\alpha_0 = 0°$, $Re = 10e^6$ (b) case 3 $M = 0.8$, $\alpha_0 = 3°$, $Re = 10e^6$

Figure 3.10: Change in lift coefficient scaled by gust amplitude for 1-cos gusts with different gust lengths

$L_g/c_{ref} = 5$ and 20. While the gust amplitude for the transonic, attached-flow case is 1% of the freestream velocity, the detached-flow case 3 requires a reduced value of 0.001% of the freestream velocity to ensure a dynamically linear response. Overall good agreement between the solution methods for all gust lengths is observed. This is particularly interesting since case 3 shows a significantly different physical behaviour compared with case 2. Close to the maximum lift coefficient the inverse shock motion starts to dominate the behaviour and the separation area increases as outlined before. Thus the change in lift coefficient reduces drastically and even becomes negative around a non-dimensional time of 10 and 20 for the short and long gust respectively.

Computational cost, if 45 sinusoidal samples are computed, is equivalent to one unsteady time-marching simulation. Based on this sampling data, various gust parameters of interest, e.g. shape, length and off-set, can be analysed at minimal extra cost provided the active frequency range is covered. On the contrary, the time-domain analysis needs to be redone for each change in gust parameter.

3.2 Large Civil Aircraft Case

The next test case is a large civil aircraft representative of a double-aisle wide-body long-range passenger aircraft. The computational mesh consists of 130,000 points on the surface and nearly 8 million points throughout the computational domain. It has been provided from the industrial partner of this work an can be seen as representative of a mesh which would be used in industry since it offers a reasonable trade-off between achieved accuracy and needed run-time. No grid convergence study has been performed herein but higher resolution of the flowfield due to a finer grid would automatically

be inherited from the linearised method. Thus, even though results presented might not be "mesh-converged", they are still suitable for the verification of the proposed method. A comparison to experimental results was not possible during the course of this thesis since the envisioned wind tunnel test in a transonic tunnel has been moved further and unfortunately was not finished in time. Moreover, results for gust responses at a flight altitude of 10 km would need measured flight test data for comparison. Due to the "theoretical" nature of the investigated aircraft these are not available. Nevertheless, the focus of this work was to establish reduced order modeling techniques based on time-marching RANS simulations which are independent of the validity of the underlying CFD solver. For consideration of resulting loads within the aircraft design and certification process the validation of the applied CFD solver will be necessary and shall not be underestimated.

A steady-state solution at a Mach number of 0.85 and an altitude of 10 km is obtained using an elastic trimming procedure based on Broyden's method [145], which balances lift and weight and ensures zero pitching moment. The steady simulation includes 94 structural modes to represent elastic deformation. Some selected modes are highlighted in Fig. 2.5 and have been discussed previously. An artificial mode for the horizontal tail plane deflection is used for trimming and shown in Fig. 3.11(a). For the steady aeroelastic trimming process an initial CFD solution is computed by driving the density residual a few orders of magnitude. Resulting surface forces are projected onto the structural modes and the structural deformations are obtained by a superposition of all modes. For the lift and moment trimming, the horizontal tail plane deflection and angle of attack are iteratively adjusted until the desired coefficients are reached. For all mesh deformations, HTP and elastic changes, the radial basis function method to deform the computational grid [130] is applied to convect the surface changes into the volume grid. The trimming loop is stopped either when the desired coefficients are reached or once the a-priori defined maximum number of iterations is exceeded. Here, a total of 6 iterations steps are performed until the global coefficients are reached. Since both sets of equations, aerodynamic and structure, are solved independently, data is exchanged after each individual step has finished. Note that the trimming works independent of the initial conditions given for angle of attack and HTP deflection. However, an appropriate initial guess can significantly speed-up the convergence. Thus the initial guess for the angle of attack is obtained by trimming the aircraft without elastic deformations first and then starting the coupled trimming loop. The rigid trimming process is part of the DLR-TAU code and is started at zero degrees angle of attack.

The resulting surface deflections compared to the initial untrimmed shape are shown in Fig. 3.11 with the initial-shape in light blue. The wing bends upwards and also twisted towards the wing tip due to the aerodynamic force as expected for a backward-swept wing. The horizontal tail plane has been rotated downwards by approximately 2 degrees to counter the pitching moment induced from the main wing. Even though

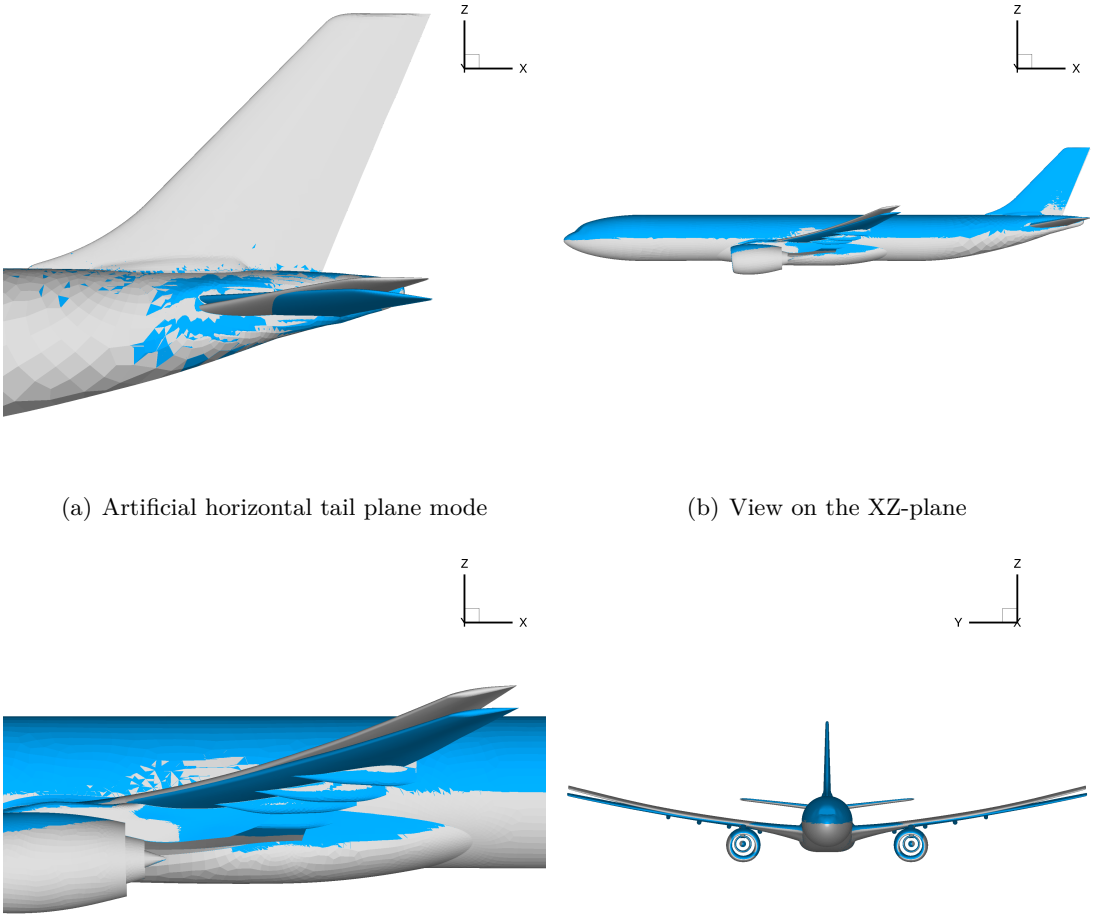

(a) Artificial horizontal tail plane mode

(b) View on the XZ-plane

(c) View on the XZ-plane - zoom on wing

(d) View on the YZ-plane

Figure 3.11: Artificial horizontal tail plane mode and surface deformation of jig and flight shape which is obtained using the steady aeroelastic trimming process

the HTP mainly counters the pitching moment, it still contributes slightly to the lift trimming. Only minor deformations are present on the fuselage. The final surface mesh, after driving the density residual to converge seven orders of magnitude, is visualised in Fig. 3.12(a). A strong shock along the wingspan at roughly 70% chord length can be seen in the steady surface pressure distribution in Fig. 3.12(b). Furthermore, the effects of the first wing bending mode in conjunction with the wing torsion mode cause a decrease of sectional lift towards the wing tip. The horizontal tail plane is deflected downwards during the trimming process but, due to the aircraft angle of attack, a strong suction area around the leading edge but no shock formation is observed.

Unsteady time-domain solver settings for the aircraft test case are summarised in Tab. 3.4. As for the aerofoil, the unsteady time-step size for all sinusoidal investigations

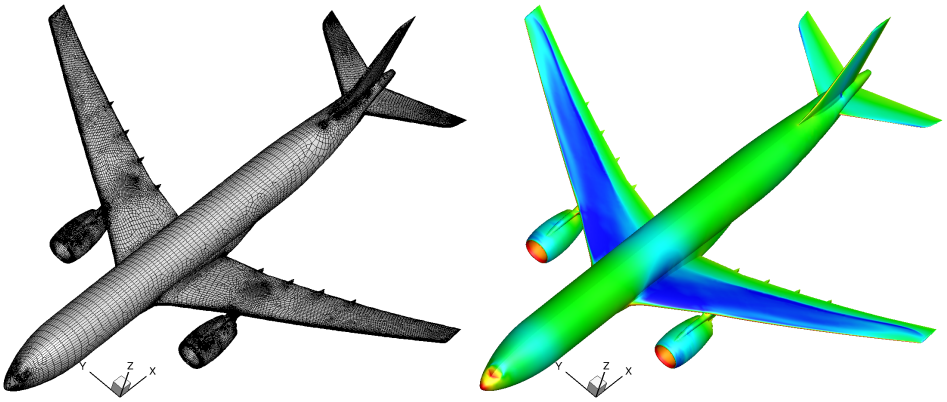

(a) Surface point distribution

(b) Steady surface pressure distribution $M = 0.85$, $H = 10km$, $\alpha_0 \approx 2.5°$

Figure 3.12: Civil aircraft surface mesh and steady-state surface pressure coefficient

Table 3.4: Time-domain numerical parameters for aircraft case

	excitation	value
Abort density residual	all	10^{-3}
Multigrid cycle scheme	all	2v
Time-steps per period	sine	128
Number of periods	sine	15
Time-step size	1-cos	0.0015 s
Number of time-steps	1-cos	1280
Time-step size	pulse	0.000725 s
Number of time-steps	pulse	5120

is chosen indirectly by defining the number of steps per period. Analysing 1-cos gust excitations, time-step size and number of time-steps follow from numerical experiments, results of which are outlined in this chapter. For pulse excitations the number of steps is increased by a factor of four while the time-step size is halved compared to a 1-cos excitation. Nevertheless, the pulse method is significantly more efficient computing a transfer function than several individual sinusoidal responses. In addition to an abort criterion based on the density residual, a Cauchy convergence criterion is applied throughout with a tolerance of 10^{-8} for the relative error of the drag coefficient chosen as control variable. Note that this rather strict convergence criterion is used to ensure accurate results even for small gust amplitudes.

Parameters for the LFD system solves are given in Tab. 3.5. A more detailed study of the influence of the abort density residual applied is presented in Sec. 3.2.1. The number of vectors is based on results presented in [133] and is chosen such that a constant number of Krylov vectors can be used for all reduced frequencies of interest.

Table 3.5: Frequency-domain numerical parameters for aircraft case

	value
Number of Krylov vectors	100
Number of deflation vectors	20
Abort density residual	10^{-6}

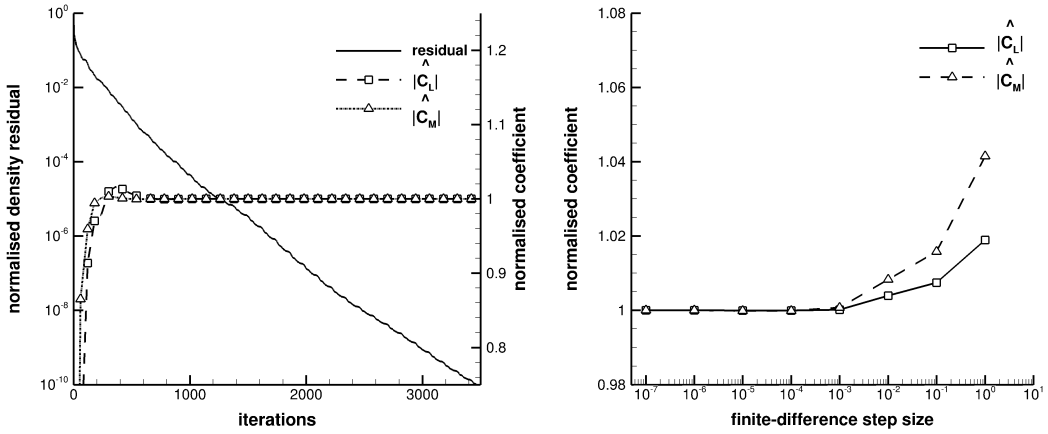

(a) Convergence behaviour

(b) Influence of finite-difference step size

Figure 3.13: Numerical study of frequency-domain gust approach for aircraft case. $M = 0.85$, $H = 10km$, $\alpha_0 \approx 2.5°$

3.2.1 Periodic Sinusoidal Gust Excitation

The convergence behaviour of the density residual as well as the complex-valued coefficients of lift and pitching moment are analysed, while solving the frequency-domain system for a vertical gust with a randomly chosen reduced frequency of 0.53. Results are presented in Fig. 3.13(a) with coefficients normalised by their converged values. Once the residual has converged five orders of magnitude, both coefficients remain essentially unchanged. Therefore, if only integrated loads are of interest, simulations can be stopped earlier, resulting in an additional time saving of 50% compared with fully converging the system. For the remainder of the discussion, the density residual is driven to drop six orders of magnitude, ensuring converged solutions for integrated loads as well as surface pressures.

Investigating the same reduced frequency as before, the influence of the finite-difference step size ε, when forming the right-hand side in Eq. (2.23), is analysed. Figure 3.13(b) shows the magnitudes of lift and pitching moment coefficients, normalised to converge towards one, for a range of finite-difference step sizes. Results independent of the step size are obtained below 10^{-3} for both coefficients, while larger values result in increasing magnitudes with a higher impact on the moment. A value of 10^{-4} is applied throughout in the following to ensure step-size independent results.

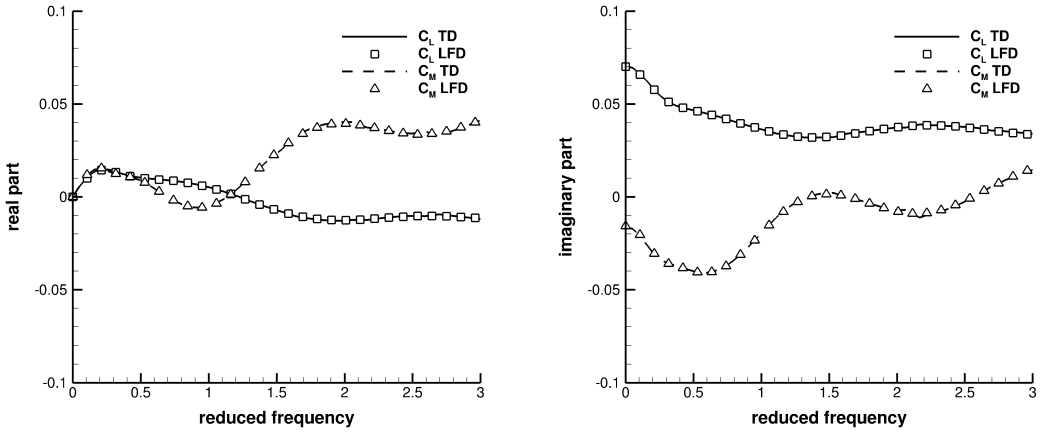

(a) Real part

(b) Imaginary part

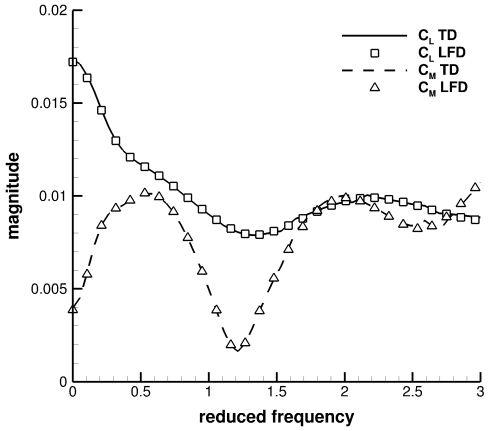

(c) Magnitude

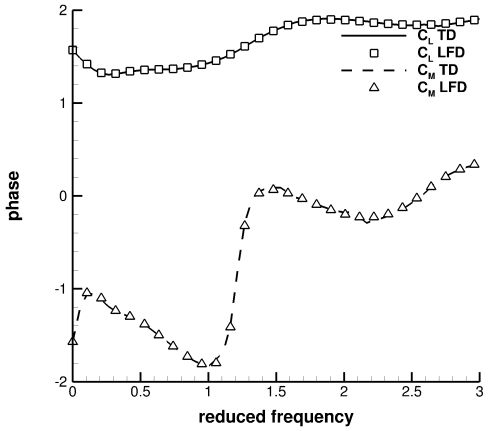

(d) Phase

Figure 3.14: Frequency response functions of lift and moment coefficients for aircraft case. $M = 0.85$, $H = 10km$, $\alpha_0 \approx 2.5°$

Comparing frequency response functions of lift and pitching moment coefficients, the accuracy of the presented method is shown at several reduced frequencies for the three-dimensional test case. Similar to the aerofoil test cases, a gust pulse excitation is used to obtain the frequency response function with just one unsteady time-marching simulation. A Fourier transform of the unsteady coefficients of lift and pitching moment is performed and resulting complex-valued Fourier coefficients are weighted by the Fourier transform of the input signal. The vertical amplitude v_{gz} of the excitation during the time-marching simulation is set to 0.001% of the freestream velocity, which ensures a linear dynamic response. Real and imaginary parts as well as magnitude and phase of the coefficients, presented in Fig. 3.14, are in good agreement at all frequencies between time- and frequency-domain predictions.

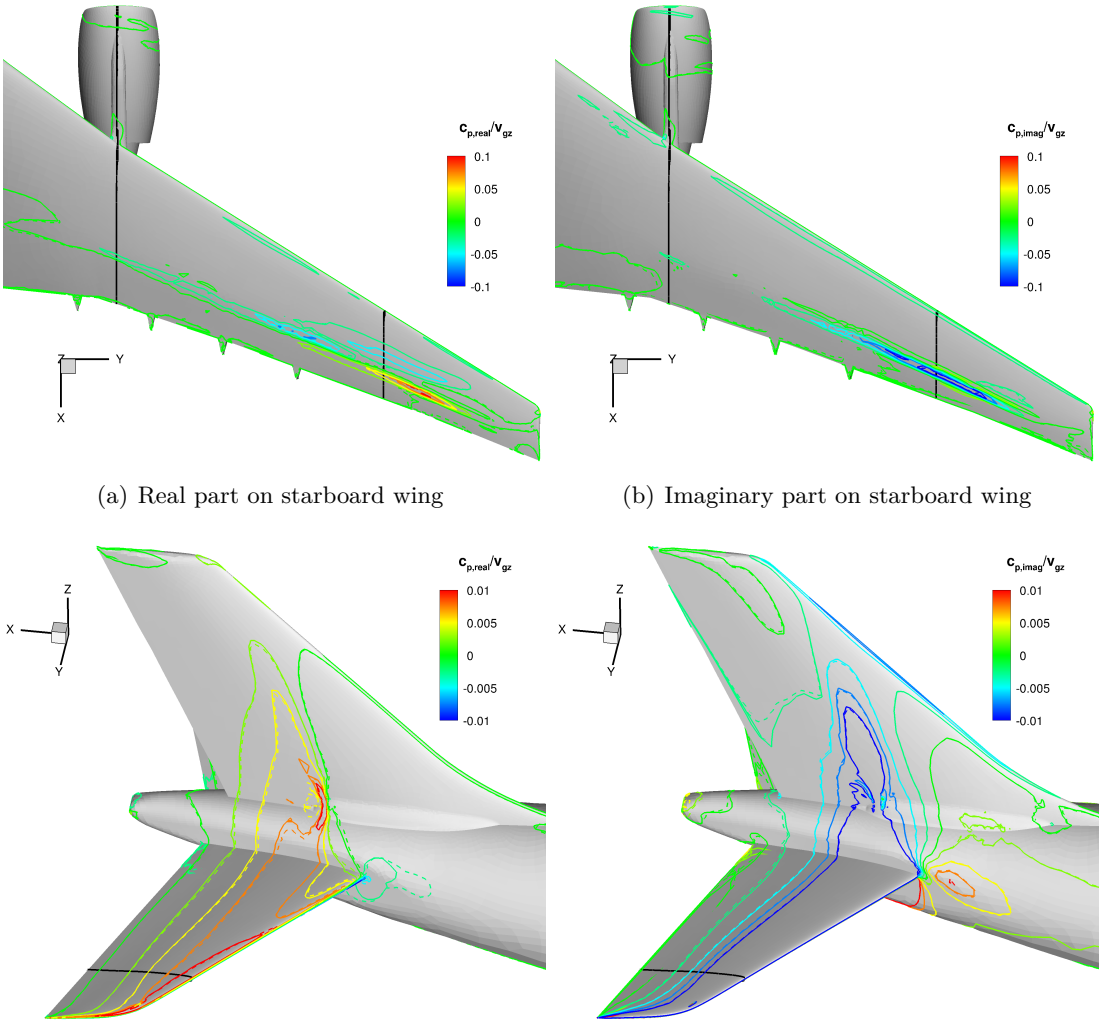

(a) Real part on starboard wing

(b) Imaginary part on starboard wing

(c) Real part on tail

(d) Imaginary part on tail

Figure 3.15: Complex-valued surface pressures for vertical sinusoidal gust at $\omega^* = 0.53$ showing time- and frequency-domain results as solid and dashed lines, respectively. Black lines indicate locations of extracted sections. $M = 0.85$, $H = 10km$, $\alpha_0 \approx 2.5°$

Complex-valued surface pressure distributions are compared at a reduced frequency of 0.53 to analyse the LFD gust method in more detail. Reference time-domain solutions are generated simulating a vertical sinusoidal gust with an excitation amplitude $v_{gz} = 0.001\%$ of the freestream velocity for 15 periods and then performing a Fourier transform on the instantaneous surface pressures during the final period. Frequency-domain solutions on the other hand are readily available once the linear system is solved. Starboard-wing results are presented in Figs. 3.15(a) and 3.15(b) for real and imaginary parts with solid and dashed lines denoting time- and frequency-domain solutions, respectively. Even at challenging flow topologies good agreement between both methods is obtained. Around the shock at 70% chord length on the upper surface

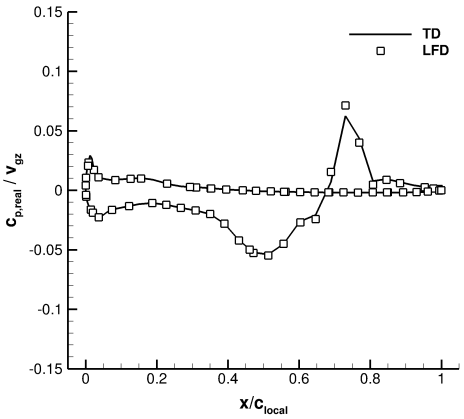

(a) Real part at 75% semi-wingspan

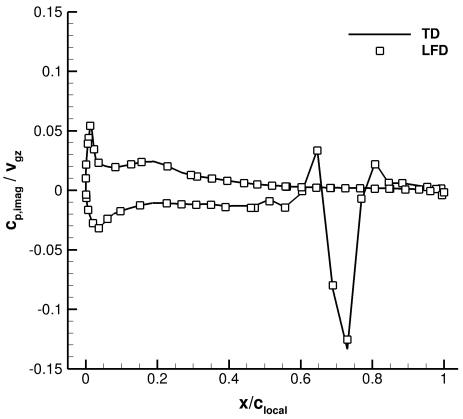

(b) Imaginary part at 75% semi-wingspan

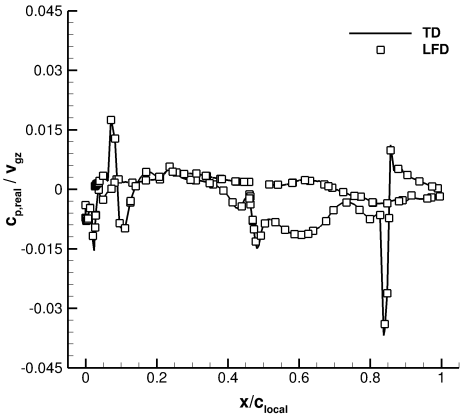

(c) Real part at 32% semi-wingspan

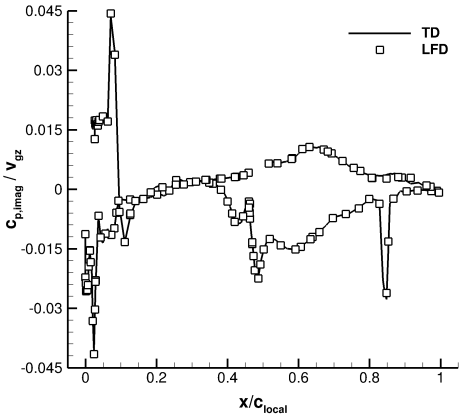

(d) Imaginary part at 32% semi-wingspan

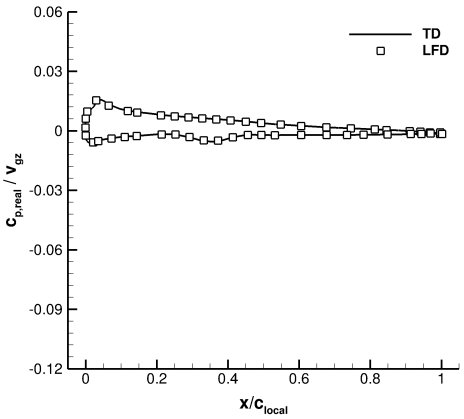

(e) Real part at 75% semi-HTP span

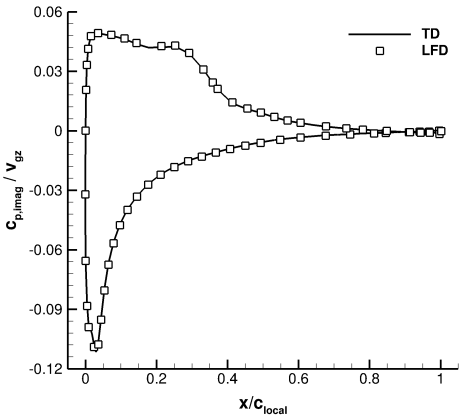

(f) Imaginary part at 75% semi-HTP span

Figure 3.16: Sectional complex-valued surface pressure distributions for vertical sinusoidal gust at $\omega^* = 0.53$. $M = 0.85$, $H = 10km$, $\alpha_0 \approx 2.5°$

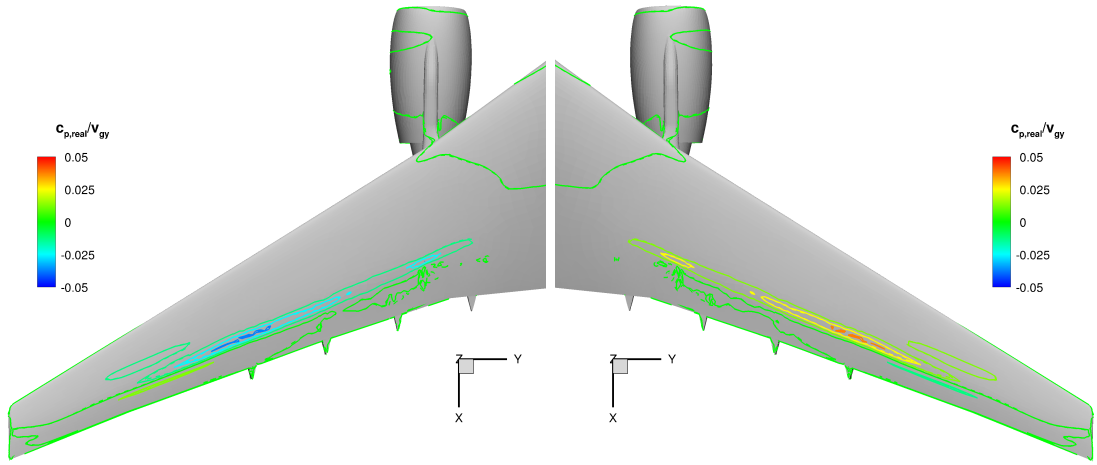

(a) Real part on port wing

(b) Real part on starboard wing

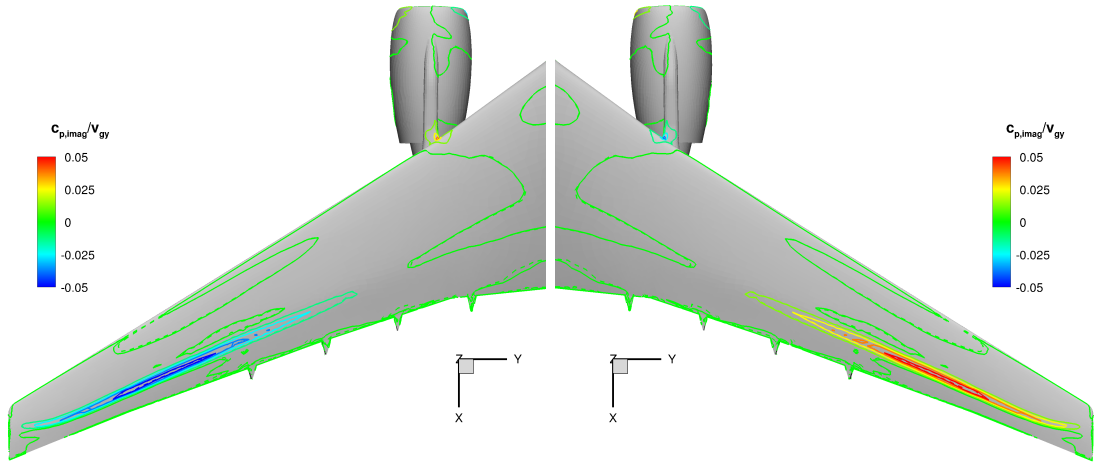

(c) Imaginary part on port wing

(d) Imaginary part on starboard wing

Figure 3.17: Complex-valued surface pressures for lateral sinusoidal gust at $\omega^* = 0.53$ showing time- and frequency-domain results as solid and dashed lines respectively. $M = 0.85$, $H = 10km$, $\alpha_0 \approx 2.5°$

the highest pressure perturbations occur, again with no differences between the simulations. Excellent agreement is observed also around the wing-pylon junction, which causes complex flow behaviour due to vortices. In addition, results are compared for the HTP and fin in Figs. 3.15(c) and 3.15(d) with similar good agreement. Highest perturbations are located around the leading edge caused by the suction area since no shock formation is present.

Results are further compared by extracting slices from the wing and HTP surfaces, the locations of which are indicated by black lines in Fig. 3.15. Real and imaginary parts are normalised by the excitation amplitude, while the x-axis is scaled by the local chord length. Figures 3.16(a) and 3.16(b) present complex-valued pressures for the first slice

at 75% semi-wingspan, showing good agreement between the two simulation techniques. Some minor differences occur between LFD and TD simulations at the shock location for both real and imaginary components. The second location at 32% semi-wingspan investigates surface pressures at the junction of wing, pylon and nacelle. Results for real and imaginary parts are displayed in Figs. 3.16(c) and 3.16(d). Note that internal nacelle surfaces are ignored for visualisation purposes. Even in this challenging flow region results from both methods are in excellent agreement. The third slice is located at 75% semi-HTP span and results are presented in Figs. 3.16(e) and 3.16(f). In contrast to previous sections on the wing, no shock formation is present, thus maximum values for real and imaginary part appear around the suction region for both methods.

The generality of the approach is shown by analysing also lateral gust response behaviour at a reduced frequency of 0.53. As before, complex-valued surface pressure distributions are discussed. Time-domain solutions are generated simulating a sinusoidal gust with a lateral excitation amplitude v_{gy} of 0.001% of the freestream velocity. Since for lateral gusts the flow topology is no longer symmetric, port and starboard wing results are visualised in Fig. 3.17 for real and imaginary parts with solid and dashed lines denoting time- and frequency-domain solutions, respectively. Highest values still occur around the shock at 70% chord length but differ in sign between port and starboard wing. Overlapping results between the two simulation methods are achieved, independent of the complexity of the steady flow field. Results for the HTP and VTP as well as different reduced frequencies have been analysed and are similarly satisfactory.

3.2.2 Aperiodic 1-cos Gust Excitation

The frequency-domain gust response approach for the large civil aircraft is now used to investigate dynamic responses to realistic 1-cos gusts. Three gust lengths of $L_g = 18$, 116 and 214 m are analysed representing the shortest, a medium and the longest value of all gust lengths as defined by the European Aviation Safety Agency in CS 25.341 [5]. A time- and frequency-domain representation is given in Fig. 3.18 showing that the shortest gust length of $L_g = 18$ excites reduced frequencies up to nearly 5. Amplitudes are chosen in accordance with the certification requirements and are in the order of 5% of the freestream velocity. First, the influence of the chosen time-step size for all TD simulations is investigated for a 1-cos gust with $L_g = 116$ m with results shown in Fig. 3.19. Whereas doubling the time-step size from its baseline value of 0.0015 s induces an error of 0.75% on the maximum lift coefficient, halving the time-step size results in a difference of 0.015%. Thus, the applied baseline time-step offers a reasonable trade-off between computational cost and achieved accuracy.

Frequency-domain sampling data is produced at 15 reduced frequencies ω^* between 0 and 3 to cover the frequency range of interest. The change in lift coefficient for all three gust lengths is shown in Fig. 3.20. If the gust amplitude is set to 0.001% of the

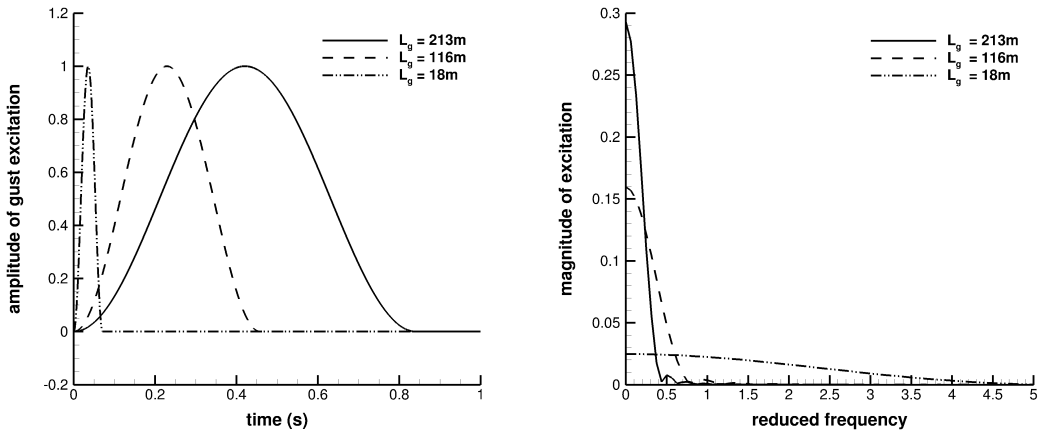

(a) Time-domain representation

(b) Frequency-domain representation

Figure 3.18: Time- and frequency-domain representation for three different gust lengths as defined by the European Aviation Safety Agency in CS 25.341

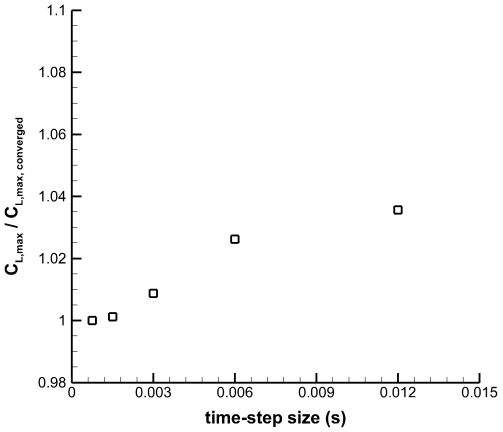

Figure 3.19: Influence of unsteady time-step size for 1-cos gust with $L_g = 116$ m. $M = 0.85$, $H = 10km$, $\alpha_0 \approx 2.5°$

freestream velocity, perfect agreement between a (then-linearised) time-domain simulation and LFD is obtained for $L_g = 214$ m, once scaling the amplitude accordingly. Similar behaviour is expected for the other gust lengths. While still a fair match is observed for the shortest gust length of $L_g = 18$ m, minor differences in the maximum lift coefficient as well as during lift decay are present for longer gusts. These discrepancies are caused by a dynamically non-linear response near the maximum lift coefficient during the time-marching simulation since an increasing gust length results in a larger gust amplitude due to the certification requirements [5]. The frequency-domain approach assumes a dynamically linear response and is overpredicting the maximum lift coefficient. It should be noted, once dynamically non-linear phenomena are present, the

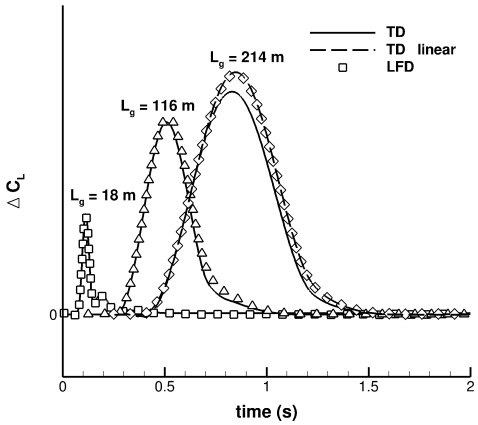

Figure 3.20: History of aircraft lift coefficient response for different 1-cos gusts. $M = 0.85$, $H = 10km$, $\alpha_0 \approx 2.5°$

LFD method is strictly speaking not valid since the assumption of linear superposition is no longer fulfilled.

For $L_g = 116$ m the relative surface pressure difference at maximum lift coefficient is displayed in Fig. 3.21(a) showing values below 1% nearly everywhere on the surface. Since a non-linear shock motion and a corresponding amplitude decrease occur during the time-domain analysis, the highest positive as well as negative differences of around 10% arises close to the steady shock location. In addition, some minor discrepancies of 5% are present around the leading edge caused by the same amplitude mechanism. In addition, the change in vertical force F_z and bending moment M_x is shown over the center wing-box axis in Fig. 3.21(b). Whereas for the force only minor differences are visible close to the fuselage, the change in moment differs more significantly. This is directly related to the surface pressure differences primarily around the shock location discussed earlier. The positive and negative error in the surface pressures cancel out when the spanwise force is calculated while for the moment this is not the case. Nevertheless, the LFD method predicts forces as well as moments conservatively.

Computational cost is presented for the two approaches in Tab. 3.6. All simulations were performed on the UK based high power computing facility ARCHER[1] using 192 standard compute cores. Since the computational time for a TD 1-cos simulation depends on the investigated gust length, the average time is taken and normalised to 1 as the reference. The time of 0.21 for the LFD covers the entire solution time for all 15 linear system solves including the calculation of the right-hand side vector and forming of the Jacobian matrix. Subsequent reconstruction of global coefficients and surface pressure distributions is negligibly low. Thus, the LFD method already offers a speed-up factor of roughly 5 compared to a single 1-cos time-marching response. As

[1]Advanced Research Computing High End Resource.

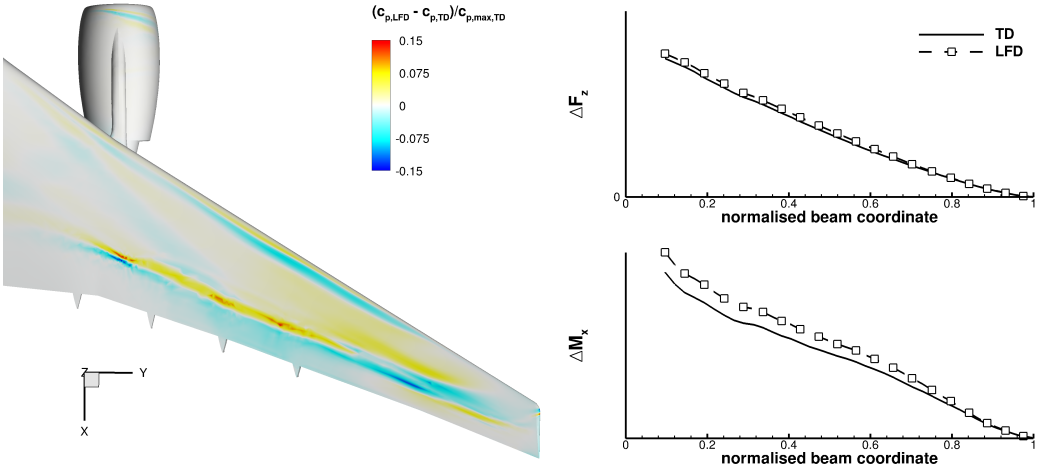

(a) Difference in surface pressure

(b) Vertical force and bending moment

Figure 3.21: Surface-pressure difference and maximum aerodynamic loads on the wing for $L_g = 116$ m. $M = 0.85$, $H = 10km$, $\alpha_0 \approx 2.5°$

Table 3.6: Comparison of computational cost for aircraft case

Task	Cost
Time-domain simulation (one gust length)	1
Frequency-domain sampling (all samples)	0.21
a) Rebuilding global coefficients	–
b) Rebuilding surfaces pressure distributions	–

discussed in detail above, the frequency-domain solutions can be recycled to investigate an arbitrary time-domain signal, as long as the excited frequency range is covered. Unsteady time-marching simulations on the other hand need to be repeated for each change in gust parameter. According to [146] a number of 30 different gust lengths at a given flight condition should be analysed during the certification process. Hence, the LFD approach offers a speed-up of two orders of magnitude compared to unsteady time-domain simulations for all gust lengths of interest.

The presented frequency-domain method for gust responses has shown excellent results for the analysis of 1-cos gusts while reducing computational cost significantly. However, some assumptions are introduced which define limitations of this approach. First, a point of linearisation is necessary. Whereas in this work a converged steady solution is obtained for all investigated cases, this is not guaranteed in general. Whereas, in a loads and aeroelastic context for commercial aircraft, this is a minor concern, for a military configuration which is highly vortex dominated, the existence of such a steady solution becomes less likely. Secondly, the applied incomplete inverse Fourier technique offers savings in computational cost since only an a-priori known range of reduced frequencies need to be considered. As seen in Fig. 3.7 for 1-cos gusts, mainly

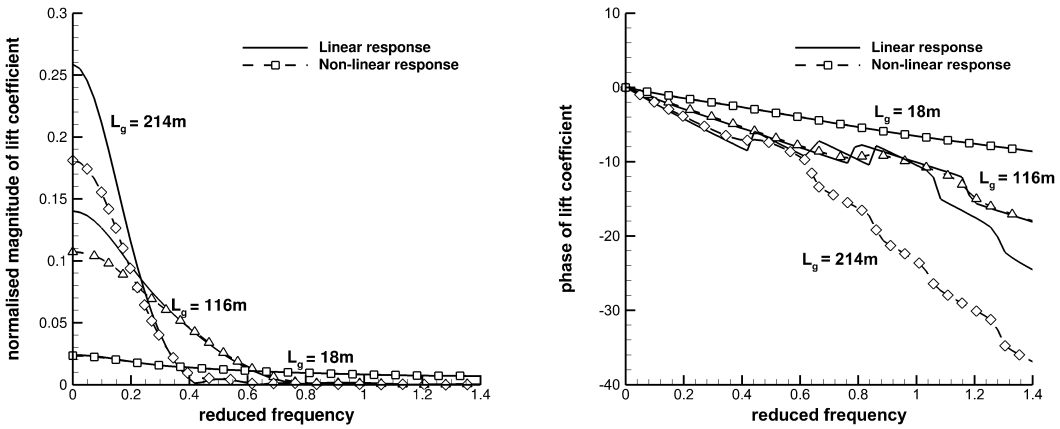

(a) Normalised magnitude

(b) Phase

Figure 3.22: Fourier transformation of linear and non-linear aircraft response to vertical gusts

small reduced frequencies are important while high frequencies can be omitted. For time-domain signals of interest which affect an infinite or a very large frequency range, the incomplete inverse Fourier technique can still be applied but the computational benefit will be reduced. Thirdly, the linearisation assumes that only infinitesimally small amplitudes are investigated and the dynamic response behaviour is purely linear. However, for gust response simulations in which amplitudes are defined by CS 25.341 dynamically non-linear behaviour is expected since gust amplitudes are in the range of 5% of the freestream velocity. Therefore, these influences will be analysed in more detail next for the large civil aircraft.

A Fourier transform of the unsteady but linear and non-linear lift-coefficient time history is performed and results are presented in Fig. 3.22. The magnitude is scaled by the gust amplitude and freestream velocity. The linear excitation amplitude is 0.001% of the freestream velocity and the non-linear amplitude is defined by CS 25.341. As mentioned before, for the shortest gust length the occurring non-linearities are only local and not visible in the integrated loads neither for magnitude nor phase. For the medium and long gust, non-linearities affect the magnitude response for low frequencies, causing the response to decrease. Concerning the phase behaviour shown in Fig. 3.22(b), for $L_g = 214$ m the phase starts to differ once the magnitude becomes nearly zero and thus is unimportant during the incomplete inverse Fourier transform. For $L_g = 116$ m only some minor deviations are visible for the phase around the poles of the excitation.

As visible when analysing the aforementioned results, the LFD method overpredicts loads compared to time-marching simulations once non-linearities occur. Even though all cases presented within this thesis show this behaviour, it can not be guaranteed unconditionally. In fact, at severe flow conditions, such as large flow separation, it is possible that results are no longer predicted conservatively since the dynamically

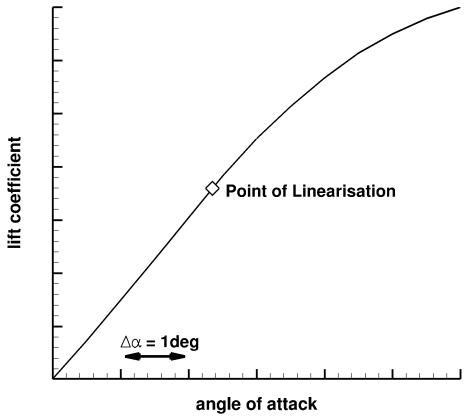

Figure 3.23: Steady lift coefficient over angle of attack for aircraft case

non-linear behaviour can cause the flow characteristics to change. For example dynamically non-linear shock motion can cause flow separation which results in negative lift coefficients and is not represented by any kind of dynamically linear analysis. A very simplistic estimation can be obtained when analysing the steady change in lift coefficient over angle of attack, since gust excitations primarily cause a change in angle of attack. An example for the civil aircraft, including the point of linearisation, is shown in Fig. 3.23 and contain several angles of attack which are of interested from an aircraft design point of view. Since all of them are either within the linear slope of the curve or before the maximum lift coefficient, the linearised frequency domain method is expected to predict loads conservatively.

3.3 Summary on Time-Linearised Gust Aerodynamics

This chapter has presented results to verify the LFD method for gust excitations. Responses to various sinusoidal gusts are first computed to reconstruct an arbitrary gust encounter, utilising a complex-valued superposition in conjunction with an incomplete inverse Fourier transform. In comparison with an unsteady time-marching approach computational cost is significantly reduced by two orders of magnitude when running a sufficient number of gust lengths. Results are presented for a NACA0012 aerofoil at three different flow conditions and a large civil aircraft. Excellent agreement compared with unsteady time-marching simulations is observed both for integrated aerodynamic coefficients and complex-valued surface pressures. The influence of retained frequencies during the incomplete inverse Fourier transform for 1-cos gust reconstruction is discussed. In addition, for the aircraft case, responses to characteristic 1-cos gusts as defined by international certification authorities are reconstructed from sinusoidal responses and compared with corresponding non-linear time-marching simulations.

The proposed approach enables industry to fully change current DLM based unsteady loads prediction process to CFD. Due to the frequency-domain evaluation of aerodynamic quantities, significant time-saving factors can be demonstrated compared to time-marching methods while steady non-linearities are retained. Therefore, this method presents a substantial step towards fully establishing CFD for the computation of unsteady loads during the aircraft design and certification process. However, the system size is still large and expert knowledge in CFD is necessary to obtain accurate loads. During the aircraft design and certification process, which has always been multidisciplinary, CFD accurate loads are desirable without the need of expert knowledge and by only analysing a small sized system. Thus, projection based reduced order modelling for aerodynamics is discussed next. This not only decreases the number of degrees of freedom but moreover allows the efficient analysis of coupled aeroelastic problems by extending the system with structural degrees of freedom.

Chapter 4

Aerodynamic Model Reduction

This chapter presents an aerodynamic reduced order model for gust analysis. The LFD method introduced in Chapter 3 is applied to generate samples of the full order model efficiently at several reduced frequencies. POD is then used to obtain a modal basis onto which the linearised operator of the RANS equations is projected. The first test case investigated is an aerofoil at transonic flow conditions. The influence of retained energy in the modal basis is discussed in-depth and a method to stabilise the reduced system is shown. The second case is the large civil aircraft near cruise condition, which is analysed to demonstrate the maturity of the method and to outline challenges of up-scaling and efficiency gains for an industry relevant test case.

Since the large system size is reduced, it enables the consideration of CFD accurate loads in a wide range of multidisciplinary applications such as aeroelasticity and aeroservoelasticity in a straightforward fashion. Especially in time-critical processes the presented model reduction allows the inclusion of non-linear aerodynamic affects. Aerodynamic loads are available within seconds without the need of correction factors for gust loads analysis.

A schematic representation of the aerodynamic model reduction approach is given in Fig. 4.1. As for the LFD method the approach consists of two stages, a construction and a solving stage. Whereas the former stage works on the FOM and is performed offline, the latter is evaluated online. Initially samples of the FOM are computed using the LFD method which is discussed in detail in Chapter 3. Thus, the upper left computing snapshots block becomes the sampling block of the LFD method when zoomed in. During the construction two steps are performed. First, modes are computed using POD with an appropriate scaling. Secondly, full-order matrices such as the system Jacobian matrix and the gust influence matrix are projected onto the modal basis in a Galerkin sense. Once the model construction is finished, the resulting small sized system can be evaluated rapidly for various different gusts. All outlined steps will be analysed in the following using the two aforementioned test cases and additional details including a volume-weighting approach for stabilisation will be discussed.

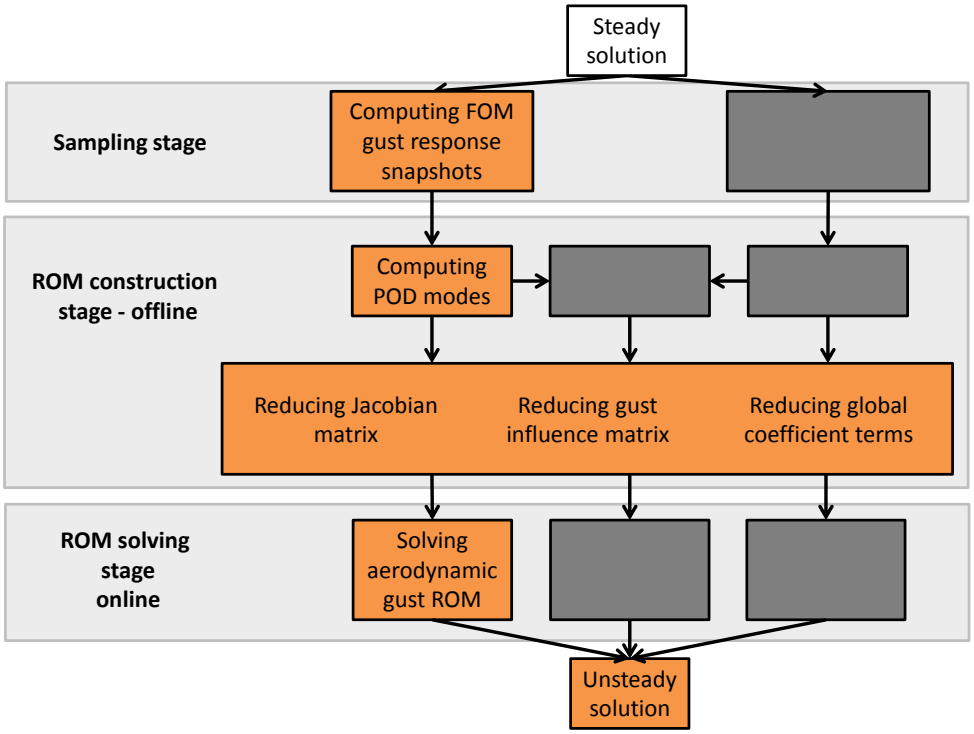

Figure 4.1: Schematic representation of aerodynamic model reduction approach

4.1 NACA0012 Aerofoil Case

A NACA0012 aerofoil is analysed in this section. The computational grid is the same as presented in Chapter 3 and is shown in Fig. 3.2. The investigated flight condition is case 2 with parameters given in Table 3.1. The altitude has been adjusted to 10 km which changes the Reynolds number to 6.8 million compared to the aerofoil cases in Chapter 3. Parameters for time-marching FOM analysis as well as LFD sample generation are given in Table 3.2 and 3.3, respectively.

POD needs a representative set of full order model data to construct a small sized model while preserving the accuracy of the underlying system. Generally, samples can be computed in time or frequency domain. The LFD method is applied throughout because of its superior computational efficiency compared with a time-marching approach as demonstrated in Chapter 3. Also the number of required samples is significantly reduced. Typically, about 20 frequency-domain samples are sufficient rather than $\mathcal{O}(1000)$ time slices using a time-marching evaluation of the full order system. Sample generation in time domain is usually performed using an a-priori defined training signal which covers a large range of frequencies in a single time-marching simulation [147]. In fact, a possible time-domain training signal here would be the pulse excitation used in Chapter 3 to efficiently evaluate the accuracy of the LFD method. During the computation several if not all time-step solutions could stored and then used as sampling data for the modal basis either directly or after a Fourier transform.

For the aerofoil case, the system response is sampled at $k = 20$ reduced frequencies ω_j^* between $\omega_0^* = 0$ and $\omega_{max}^* = 2$ using a power lower

$$\omega_j^* = \omega_0^* + \left(\frac{j}{k}\right)^2 \omega_{max}^* \quad \text{for} \quad j = 0, \ldots, k \tag{4.1}$$

This sampling strategy has been found beneficial over uniformly distributed frequencies since it reflects the Fourier transform of 1-cos gusts with small frequencies generally being more important than large ones as shown in Section 2.1.1.3 and for several gust lengths in Fig. 3.7. Note that a signal which activates a different frequency spectrum than 1-cos would call for an adjusted sampling strategy.

For forming the ROM basis, complex conjugates of the snapshots can be included at no additional cost. While this is essential if the resulting ROM is analysed in time domain, it is not necessary for a frequency-domain based representation since the frequency-domain ROM only needs the response at positive frequencies. A time-domain model on the other hand also needs the response at negative frequencies to give consistent results. This can be seen when looking at a Fourier transformation on a time-domain signal. It decomposes the signal in negative as well as positive frequencies. First, results will be presented for a frequency-domain ROM formulation to highlight the significant reductions in size. Secondly, also complex conjugates will be included and additional steps necessary for a stable time-domain modal basis will be outlined.

4.1.1 Classical Proper Orthogonal Decomposition Method

The relative information content, see Eq. (2.44), of all 20 POD modes is presented in Fig. 4.2(a) with the sum scaled to one. The first mode contains 99% of the energy indicating that the vast majority of the dynamic behaviour is described by the first mode. From mode 16 on the corresponding relative information content is 7 orders of magnitude smaller than the first one. These modes have a negligible contribution to the reconstruction of the full order model behaviour.

The magnitude of pressure for chosen POD modes is presented in Fig. 4.2 while selected modes are highlighted in Fig. 4.2(a). All modes indicate the shock location as the region with the highest fluctuations. This correlates to the physical behaviour which is dominated by the unsteady shock motion and also reflects the results shown in the underlying LFD samples in Fig. 3.5. Note that the POD modes are constructed based on samples between a reduced frequency of 0 and 2 and therefore highlight areas of importance throughout this frequency range and not only at a single frequency as shown in Fig. 3.5. From the second mode on, fluctuations in other regions of the flowfield are observed such as the leading edge suction area and the area downstream of the shock wave. However, the contribution of these is significantly smaller compared to the shock. Moreover, the shock is enlarged inside the computational domain as well as

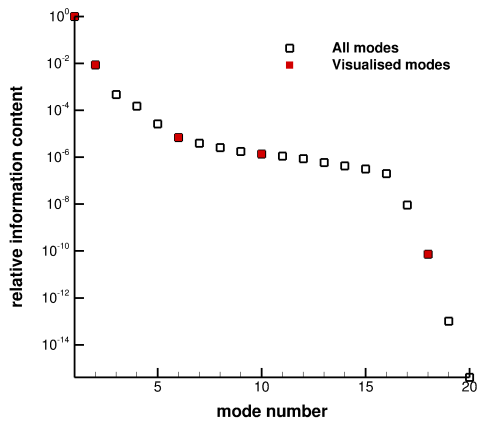

(a) Relative information content

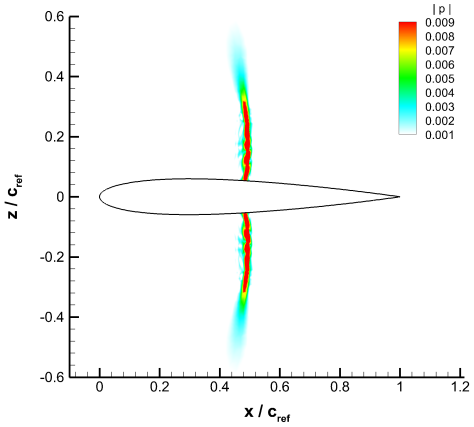

(b) Mode 1

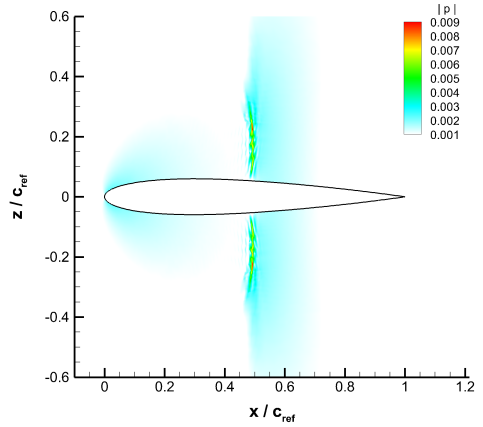

(c) Mode 2

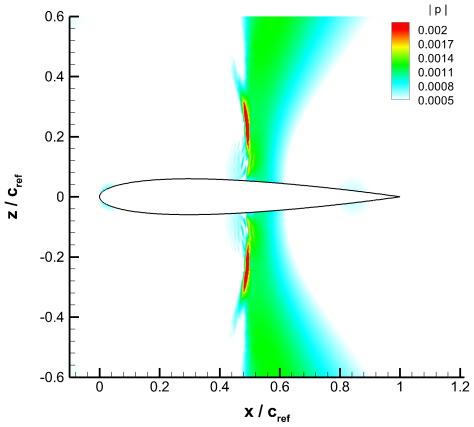

(d) Mode 6

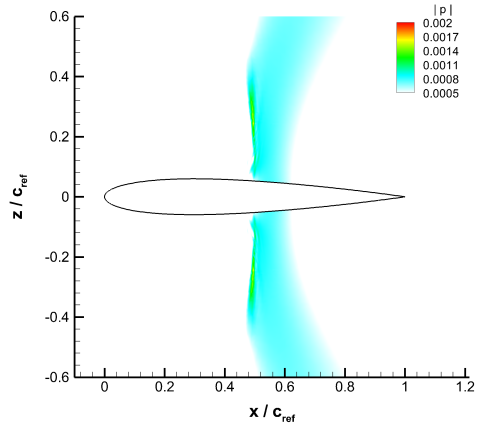

(e) Mode 10

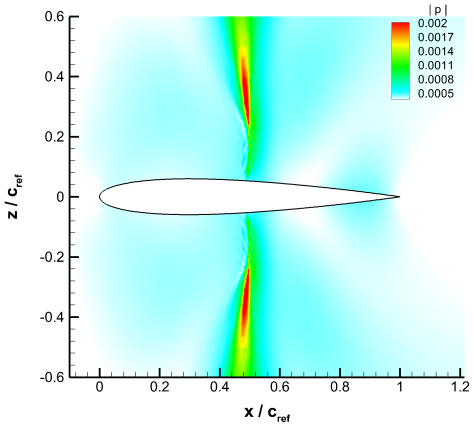

(f) Mode 18

Figure 4.2: Magnitude of non-dimensional pressure for several POD modes.
$M = 0.8$, $\alpha_0 = 0°$, $Re = 6.8e^6$

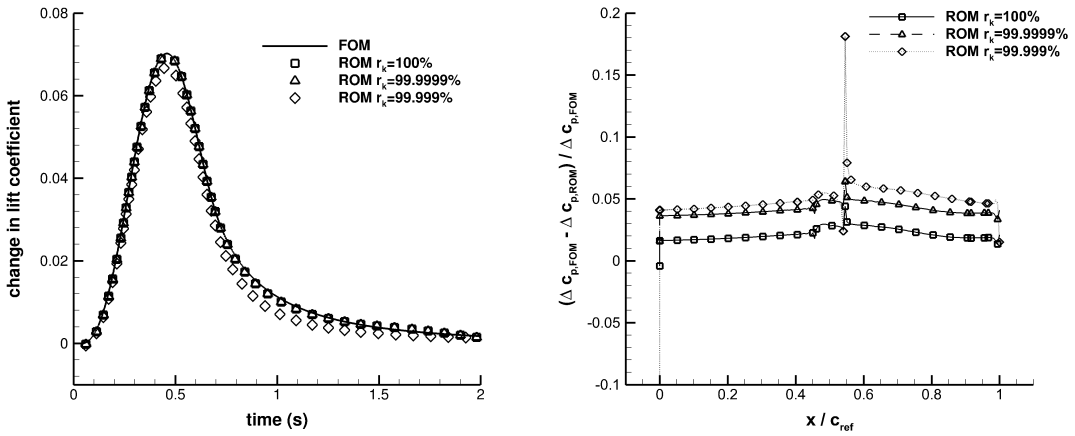

(a) Change in lift coefficient

(b) Change in surface pressure distribution

Figure 4.3: Aerofoil POD ROM response with different amounts of relative information content analysing a 1-cos gust with $L_g = 20c_{ref}$. $M = 0.8$, $\alpha_0 = 0°$, $Re = 6.8e^6$

downstream which means that fluctuations besides the shock movement are captured within the modes but rated as less important to the overall physical gust response behaviour. Since all information contained in the initial sampling is represented in the modes, small scale fluctuations are present. This is in particular the case for mode 18 upstream of the shock.

The POD ROM is constructed by projecting the linearised operator of the RANS equations onto the small modal basis retaining different levels of relative information content. All resulting ROMs are unstable in time domain since the projected Jacobian matrix has eigenvalues with positive real part (compare Fig. 4.5). However in frequency domain, the linearised small system can still be solved. Due to the small matrix size and consequent possible direct solution techniques, the number of resolved frequencies can be freely chosen. Here 300 equally spaced reduced frequencies are applied between 0 and 2 and time-domain behaviour is reconstructed using the inverse Fourier technique outlined in Section 3.1.2. The influence of the retained relative information content is shown in Fig. 4.3 for a gust length of $L_g = 20\ c_{ref}$ and an amplitude of $v_{gz} = 0.01\ U_\infty$. As in Chapter 3 the small amplitude is chosen to ensure a dynamically linear behaviour of the time-marching reference solution. The change in lift coefficient is presented in Fig. 4.3(a). When all modes are retained the reduced system size is equivalent to the number of underlying samples and has 20 degrees of freedom. By subsequently reducing the energy content considered during the model construction, the size of the ROM reduces further. For example, for 99.9999% of the energy 13 modes are included and with 99.999% only 7 modes are retained. The FOM behaviour for changes in lift coefficient is accurately predicted by the ROMs with 20 and 13 modes. With only 7 modes, some minor deviations are present around the maximum lift value and during

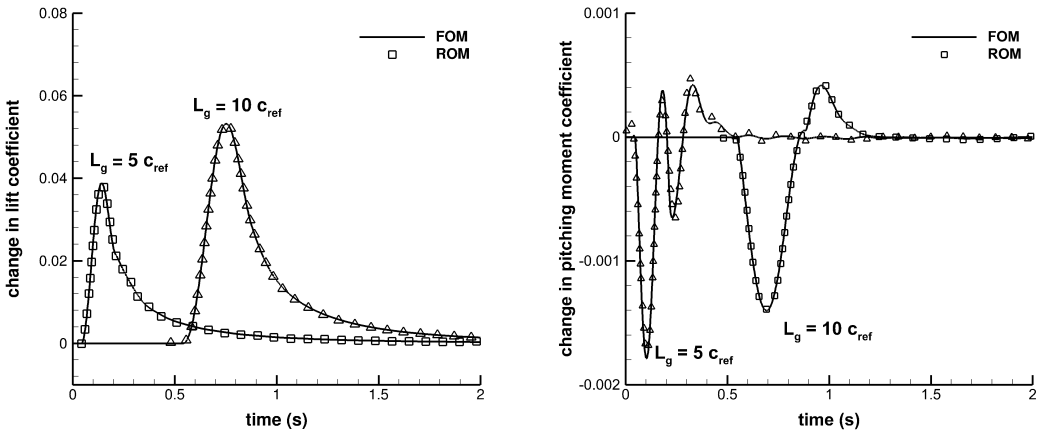

(a) Change in lift coefficient

(b) Change in pitching moment coefficient

Figure 4.4: Aerofoil POD ROM response for different gust lengths. $M = 0.8$, $\alpha_0 = 0°$, $Re = 6.8e^6$

the lift decay. It should be highlighted, that the entire CFD solution including all points in the flowfield are considered during the model forming and the flowfield at all points can be reconstructed from the ROM with just a matrix-vector product. Thus, the surface pressure distributions at the peak lift location are available at no additional cost and can be consulted to evaluate the accuracy of the ROM. The error in surface pressure distributions at the point of the maximum lift coefficient, calculated using

$$\text{error} = (\Delta c_{p,FOM} - \Delta c_{p,ROM})/\Delta c_{p,FOM} \tag{4.2}$$

between full and reduced model is visualised in Fig. 4.3(b). For all three ROMs the maximum error is below 0.2 and the average error below 0.05 with deviations mainly present around the shock location.

The amount of retained energy is set to be 100% for the following investigations to ensure the highest level of accuracy possible. The obtained reduction in size is from 350,000 to 20 degrees of freedom which can be solved on a local desktop computer within fractions of seconds. Besides the gust length of $L_g = 20\ c_{ref}$, also two other gust lengths are analysed to demonstrate that the ROM can be used for a wide range of different gust parameters without recomputing. Results are shown in Fig. 4.4 for $L_g = 10\ c_{ref}$ and $L_g = 5\ c_{ref}$ with excellent agreement between FOM and ROM for changes in lift as well as pitching moment coefficient.

While significant reduction in degrees of freedom with a high level of accuracy is demonstrated above, the presented POD model has a drawback. When analysing the eigenspectrum of the reduced Jacobian matrix $\mathcal{A} = \Phi_{POD}^H A \Phi_{POD}$ in Fig. 4.5, it is evident that the resulting reduced order model is unstable. In fact, non-existing stability

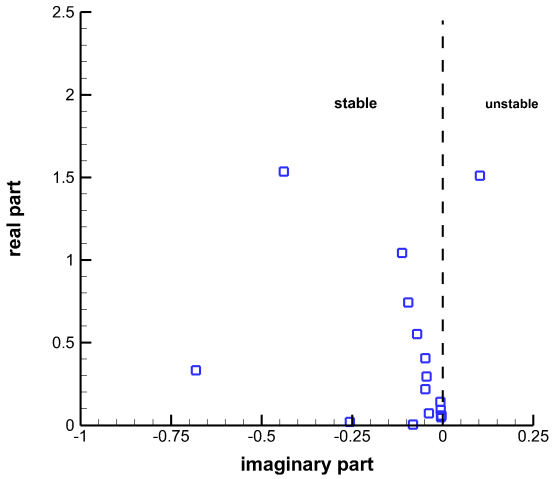

Figure 4.5: Eigenspectrum of reduced Jacobian matrix $\mathcal{A} = \Phi_{POD}^{H} A \Phi_{POD}$ for aerofoil POD ROM. $M = 0.8$, $\alpha_0 = 0°$, $Re = 6.8e^6$

for POD based models in the field of fluid dynamics is well known and has been discussed for example in [136,148]. It has been concluded that the underlying dot product used in Eq. (2.44)(i.e. $S^H S$) is the source as well as the solution to the numerical instability of the ROM. If the classical L2 norm and its corresponding dot product is used the resulting POD modes are not physical since all conservative variables are accounted for during the forming of $S^H S$. Thus, the resulting model does not have a consistent physical dimension such as energy or velocity and violates conservation which results in the non-existing stability. Note that, even though the relative information content is also often referred to as energy it is not an energy in the physical sense. Different dot products have been proposed over the years to perform a more physical evaluation of modes. Even though good results have been reported for Euler equations [149], this change in dot product calls for major modifications of the underlying CFD code since several degrees of freedom are aggregated. Especially for an established industry-grade code such as DLR-TAU, used in this work, this is impractical. Instead, in [136] it has been proposed to consider the cell volume $\mathcal{V}$ when forming the POD correlation matrix $S^H \mathcal{V} S$ as it is done in Eq. (2.46). Since no alterations in the original CFD code are necessary for this operation, this method is applied in the following for the POD based gust ROM to give a stable time-domain system.

4.1.2 Volume-weighted Proper Orthogonal Decomposition Method

The relative information content for the POD ROMs solving Eqs. (2.44) and (2.46) is shown in Fig. 4.6. Since complex conjugates of all samples are included the number of possible modes is increased to 39. The sample at reduced frequency zero is purely real and has no complex conjugate. When weighting with the cell volume, the relative

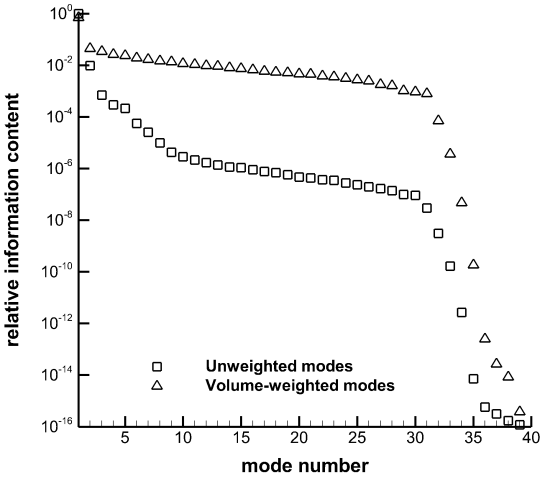

Figure 4.6: Relative information content of POD modes with and without weighting by cell volumes for aerofoil case. $M = 0.8$, $\alpha_0 = 0°$, $Re = 6.8e^6$

information content of the first mode decreases to around 75% from 99%. The difference between the first and second mode is more than one order of magnitude independent of the cell volume scaling. When computing the correlation matrix $S^H \mathcal{V} S$ the influence of all points is multiplied by their corresponding cell volume decreasing the influence of the boundary layer because cells are small in this region. Thus, the model reduction is considered to be more global resulting in the energy to be more distributed between several modes rather than clustered in the first few.

The magnitude of pressure is compared for the three different modes between both models showing the flowfield around the aerofoil in Fig. 4.7. The maximum value has been scaled to one to analyse differences in the activated flowfield regions rather than investigating the scaling of the modes. For the first mode in Figs. 4.7(a) and 4.7(b), the shock position is the only affected region and the influence of the volume scaling is negligible. Therefore, both ROMs identify the shock as the dominant flow feature for the presented test case. As already stated above, this correlates to the physical behaviour as well as the underlying LFD samples. For the sixth mode, differences are clearly visible. The volume-weighted mode affects the flow upstream of the shock whereas the unweighted mode is still largely dominated by the shock. This reflects the statement of a more global representation of the flowfield when applying a volume-weighted POD basis since physical behaviour besides the shock position gets accounted for from higher rated modes. For mode 18 only small deviations are present at several locations around the aerofoil for the unweighted ROM. The volume-weighted ROM includes the shock as well as the regions around the leading edge and downstream of the shock. When comparing the relative information content of mode 18, the unweighted model is four orders of magnitude smaller which indicates that its importance for the

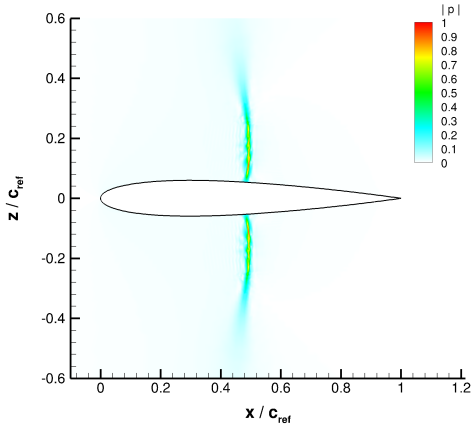

(a) Mode 1 - unweighted

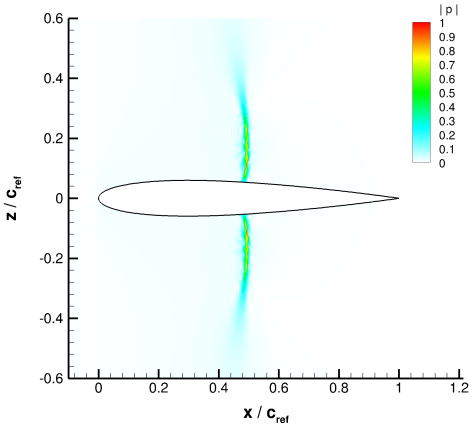

(b) Mode 1 - volume-weighted

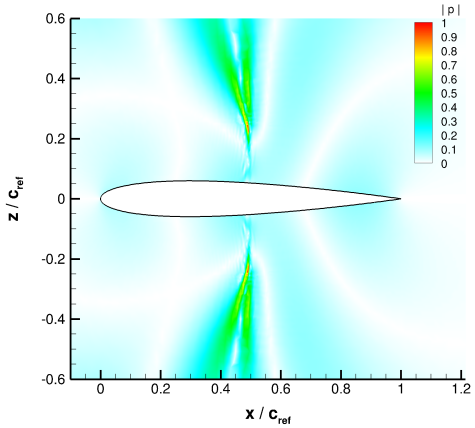

(c) Mode 6 - unweighted

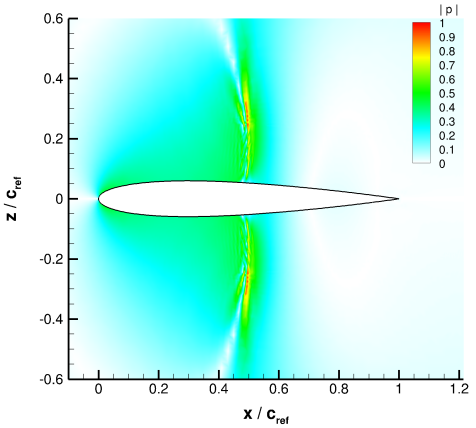

(d) Mode 6 - volume-weighted

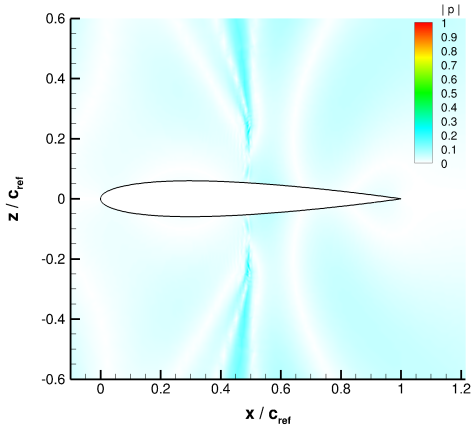

(e) Mode 18 - unweighted

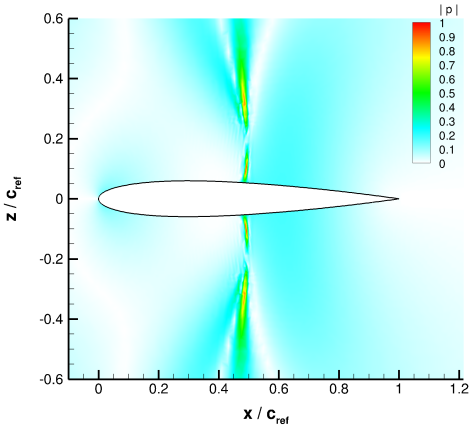

(f) Mode 18 - Volume-weighted

Figure 4.7: Magnitude of pressure for several unweighted and volume-weighted POD modes. $M = 0.8$, $\alpha_0 = 0°$, $Re = 6.8e^6$

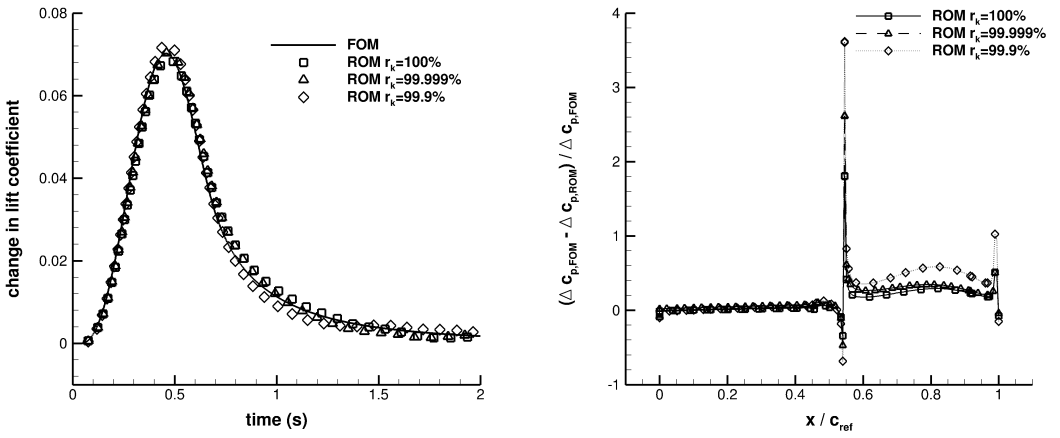

(a) Change in lift coefficient

(b) Change in surface pressure distribution

Figure 4.8: Volume-weighted POD ROM response with different amounts of relative information content analysing a 1-cos gust with $L_g = 20\ c_{ref}$. $M = 0.8$, $\alpha_0 = 0°$, $Re = 6.8e^6$

reconstruction of the unsteady flow behaviour is significantly smaller than the volume-weighted mode 18.

Next, the predictive capabilities as well as the possible reductions in size are analysed for the volume-weighted POD model. When comparing the unweighted and volume-weighted ROMs with an energy content of 99.9999%, the volume-weighted ROM roughly triples in size to 32 instead of 11 modes. However, in comparison with the FOM size of 350,000, these difference in ROM size are negligible since both the unweighted and the volume-weighted ROM can be analysed on a local desktop computer in fractions of seconds. The change in lift coefficient for all three volume-weighted ROMs compared to the FOM reference solution is shown in Fig. 4.8(a) with good agreement. Some minor oscillations around the peak value as well as during the lift decay are present regardless of the energy content. When analysing the error for the change in surface pressure distribution at the time-step of the maximum lift coefficient, as shown in Fig. 4.8(b), the largest error is around the shock location as for the unweighted ROM. The size of the error increased to roughly 2 for all modes and nearly 4 with only 32 modes. Moreover, the pressure distribution downstream of the shock is not as well captured as in Fig. 4.3(b) with maximum error values of 0.5 differing slightly between upper and lower surface. Hence, increasing the stability of the volume-weighted ROM, the accuracy is sacrificed. Therefore, if only loads are of interest the unweighted ROM should be used whereas the volume-weighted ROM offers a reasonable trade-off between accuracy and stability in case a time-domain analysis is inevitable.

The ROM all possible 39 modes is used to predict responses to gusts with $L_g = 5\ c_{ref}$ and $L_g = 10\ c_{ref}$. Results for changes in lift coefficient as well as pitching moment are shown in Fig. 4.9. For the change in lift coefficient, good agreement between FOM

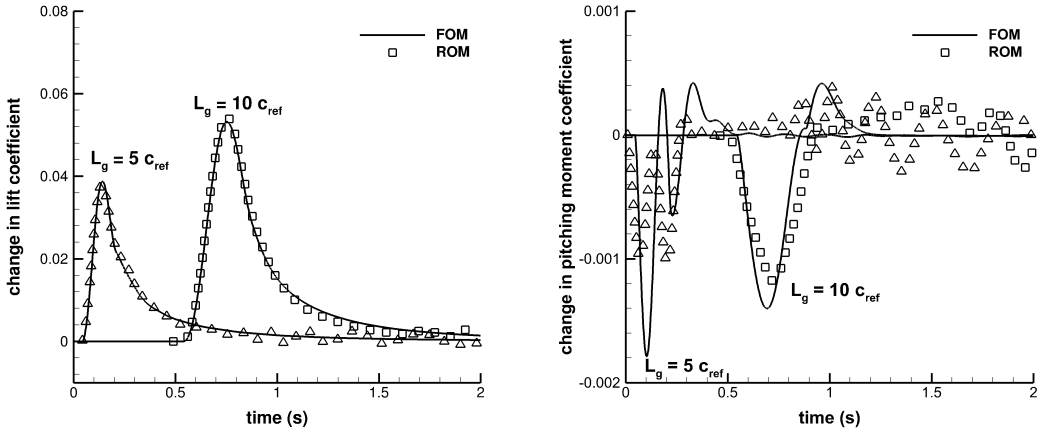

(a) Change in lift coefficient

(b) Change in pitching moment coefficient

Figure 4.9: Volume-weighted POD ROM response for different gust lengths. $M = 0.8$, $\alpha_0 = 0°$, $Re = 6.8e^6$

and ROM is observed with values slightly overpredicted for the longer gust length and slightly underpredicted for the shorter gust length. In addition, both responses exhibit some minor oscillations during and after the lift decay. The change in pitching moment coefficient is not as accurately predicted. While overall trends are captured, peak values corresponding time-steps are not matching. In addition, oscillations, occurring during the lift decay, are more pronounced. As visible in Fig. 4.8(b), the shock becomes more smeared and the pressure distribution downstream of the shock is not accurately predicted. The impact on the lift coefficient is small but the pitching moment starts to deviate stronger from the FOM reference solution. Especially for the shortest gust length, neither peak values nor the overall trend is accurately captured. However, for an aerofoil the moment coefficient response behaviour is strongly dominated by the correct prediction of local features, whereas for a full aircraft configuration the moment coefficient is mainly driven by the force on the wing in conjunction with the force on the tail plane. Since the accuracy of the force prediction (compare lift coefficient response) is still good, it is expected and will be shown later on, that the influence of the volume weighting on the global moment coefficient is less severe.

Comparing both methods, using the unweighted, classical POD method offers stronger reductions in size and results are slightly more accurate. However, the resulting ROM is unstable and thus the system can only be solved in frequency domain. If only a loads analysis is of interest, this is not an issue since a-periodic frequency-domain techniques can be applied to investigate aperiodic time-domain signals. If a stable time-domain model is necessary, for example in a multidisciplinary control design context, the cell volume can be considered when forming the correlation matrix $S^H \mathcal{V} S$ leading to the volume-weighted POD formulation. While stability is now ob-

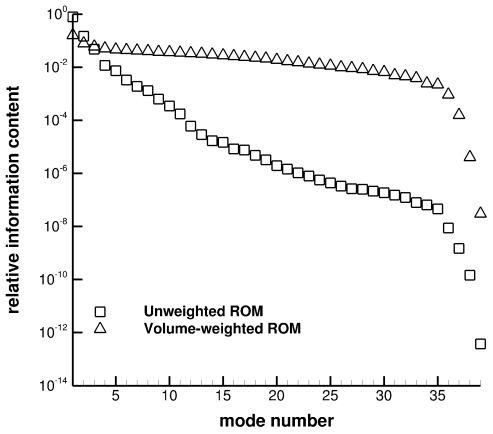

Figure 4.10: Relative information content of all unweighted and volume-weighted POD modes for large civil aircraft. $M = 0.85$, $H = 10km$, $\alpha_0 \approx 2.5°$

tained for all herein presented models, the accuracy decreases slightly as demonstrated above. In fact, this trade-off between stability and accuracy has also been reported in different POD applications [148]. In current industrial multidisciplinary applications, potential flow methods are dominating. Therefore, the decrease in accuracy of the volume-weighted ROM is acceptable since it enables the inclusion of highly accurate CFD loads in application areas which currently are solely based on low-fidelity aerodynamics.

4.2 Large Civil Aircraft Case

The next test case is the large civil aircraft, introduced in detail in Section 3.2, at the same flow conditions. The system response is sampled at 20 reduced frequencies between 0 and 2 using a power law as before for the aerofoil test case and given in Eq. (4.1). Complex conjugate samples are included during the model construction.

4.2.1 Volume-weighted Proper Orthogonal Decomposition Method

The relative information content of all possible 39 POD modes is displayed in Fig. 4.10. As for the aerofoil case before, it is depending on the volume-weighting and the majority of energy for both models is contained within the first mode. For the unweighted ROM, this is approximately 78% compared to only 15% with volume-weighting. This indicates that the flow around the full aircraft configuration is more complex than for the aerofoil where the unsteady behaviour was dominated by the gust-shock interaction. Since different flow phenomena besides the shock are present for the aircraft, it can not be expected that the first mode contains all relevant information. Moreover, if a volume-weighting is performed, no significant drop is present between the first and the

last mode. Thus, using the same truncation levels, the volume-weighted ROM will be larger compared to its unweighted counterpart. However, compared to the size of the full order model these differences are negligible.

The magnitude of pressure for the first unweighted and volume-weighted POD mode is shown for the whole aircraft, around the main wing and around the tail in Fig. 4.11. Several slices are displayed to visualise the three-dimensional structure of the POD mode, also inside the flowfield. For both ROMs the affected areas are the wing and the HTP with no pressure fluctuations present around the fuselage and fin. Since the vertical gust excitation is symmetric, deviations on the port and starboard wing are identical. On the upper wing surface, the governing flow features, namely the shock formation and the suction area around the leading edge, are clearly visible and describe the area of highest variations in Figs. 4.11(c) and 4.11(d). When the volume-weighted formulation is used also the suction area between the leading edge and the shock is clearly visible. This is interesting since the change in lift on the wing results primarily from surface pressure changes in this region rather than the shock motion. Comparing inboard and outboard sections of the wing, both POD modes contain dominant features in the outboard region supporting the fact that gust loads define the outer wing structure. With no shock formation present on the tail, the HTP exhibits pressure deviations only around the suction line at the leading edge with no significant differences between both ROMs. This again emphasises that gust loads are critical for the wing design and rather unimportant for any other structure.

The influence of energy retained inside the ROM is investigated using a 1-cos gust with length $L_g = 116$ m and an amplitude of 0.001% of the freestream velocity to ensure a dynamically linear response of the FOM solution. Time histories of the lift and pitching moment coefficient for the full order reference solution and the unweighted as well as volume-weighted ROM are presented in Fig. 4.12. First, the unweighted ROM is analysed. If all possible 39 modes are included, the time-domain signals are rebuilt accurately. When the energy is decreased to 99.9999%, reducing the number of modes to 28, the accuracy does not decrease. For 99.99% however, the time-domain signals are no longer correctly predicted by the ROM. Even though the size decrease to 12 modes this ROM is not useful for analysing gust response behaviour. For the volume-weighted ROM a different trend is observed. Retaining all modes accurately captures the FOM behavior for lift as well as pitching moment coefficient. This is in contrast to the aerofoil case in which the pitching moment coefficient behaviour was not accurately computed. However, for the aircraft the pitching moment is also more global value since it is mainly driven by the force on the horizontal tail plane and wing rather than from the local pressure distribution on the wing. Even though the accuracy does not decrease, 99.9999% and 99.99% does only decrease the model size to 38 and 37 modes, respectively. When adjusting the levels it soon becomes obvious that there is no natural cut off any more making a mode truncation unreasonable for the volume-weighted ROM

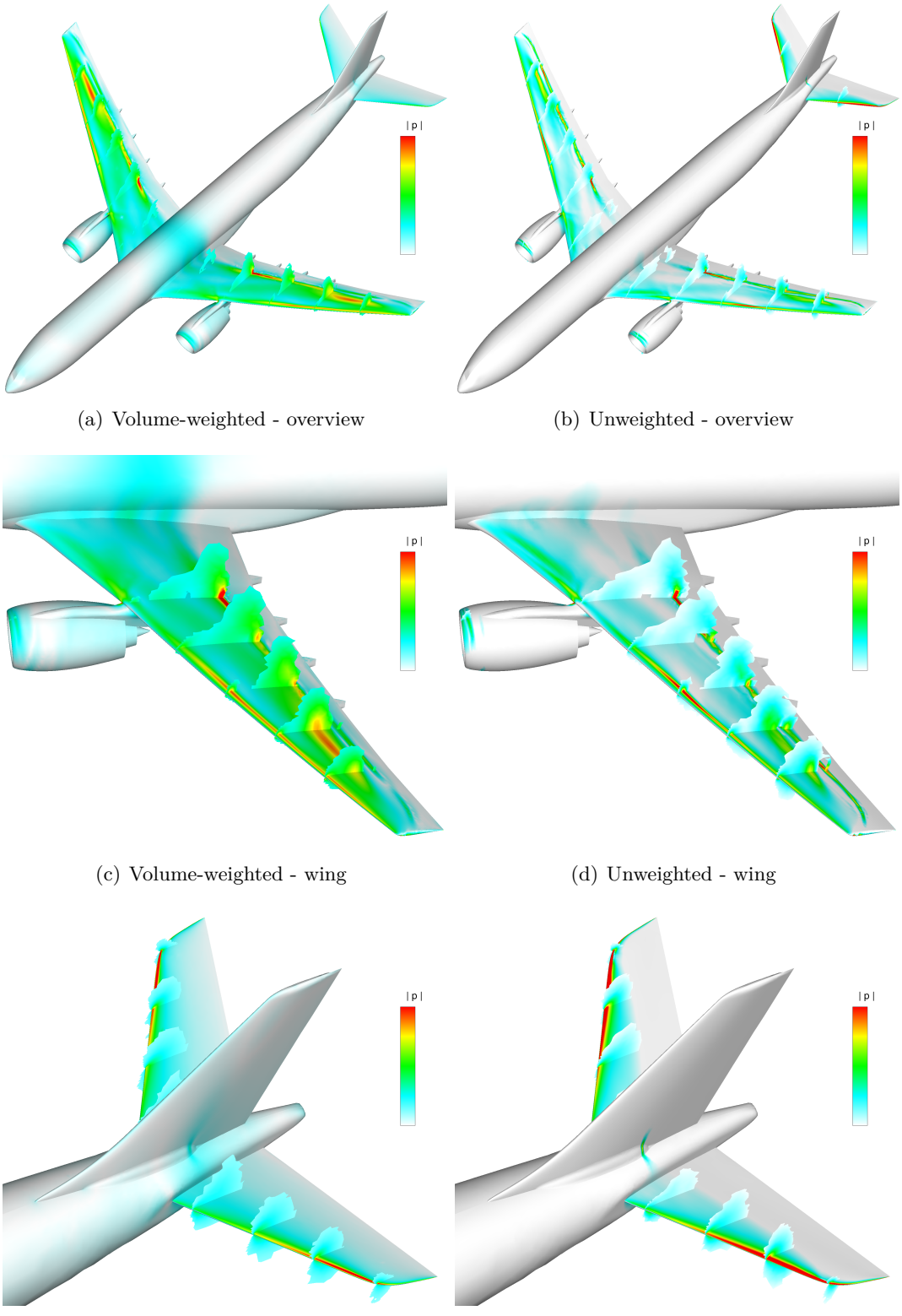

(a) Volume-weighted - overview

(b) Unweighted - overview

(c) Volume-weighted - wing

(d) Unweighted - wing

(e) Volume-weighted - tail

(f) Unweighted - tail

Figure 4.11: Pressure magnitude for first POD mode of large civil aircraft with and without volume-weighting. $M = 0.85$, $H = 10km$, $\alpha_0 \approx 2.5°$

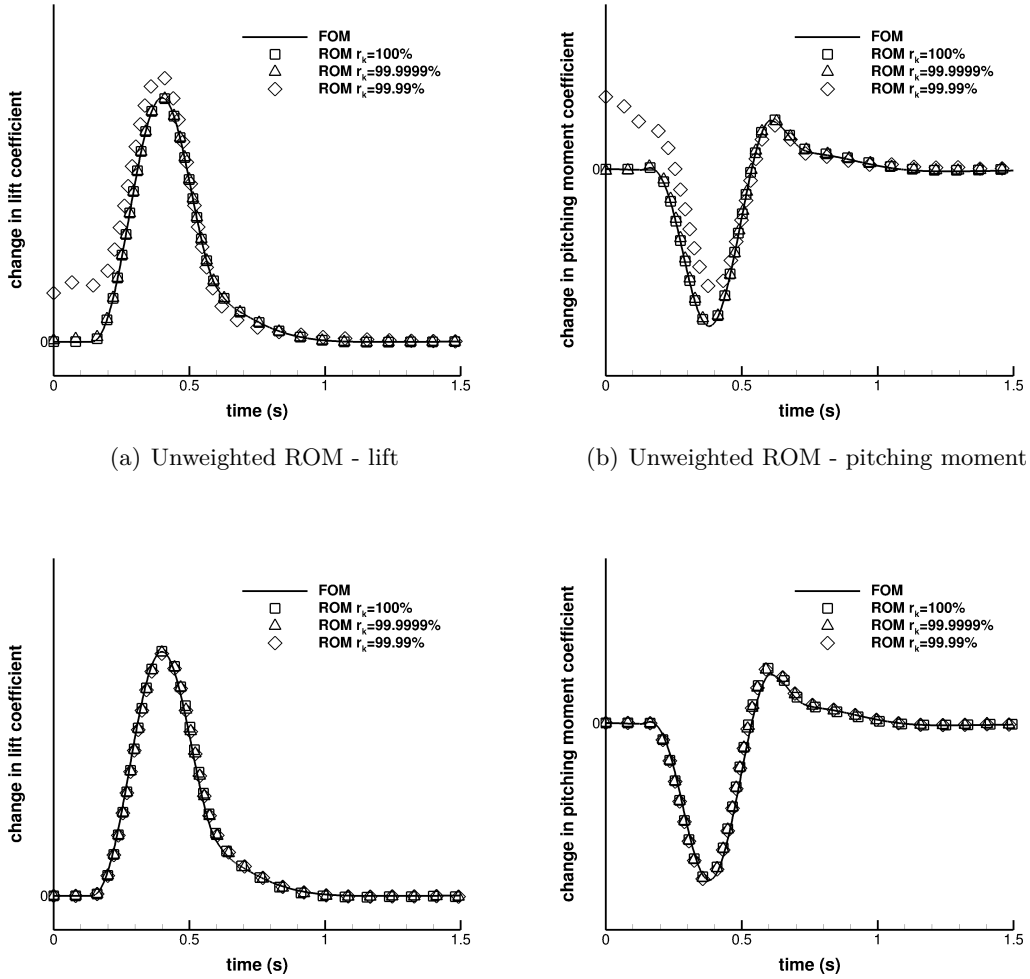

(a) Unweighted ROM - lift

(b) Unweighted ROM - pitching moment

(c) Volume-weighted ROM - lift

(d) Volume-weighted ROM - pitching moment

Figure 4.12: Investigation of modes retained in POD ROM for aircraft using a 1-cos gust with $L_g = 116$ m for time history of change in lift and pitching moment coefficient. $M = 0.85$, $H = 10km$, $\alpha_0 \approx 2.5°$

for the aircraft case.

Surface pressure distributions on the starboard wing are compared between the FOM reference solution and the unweighted and volume-weighted ROM with 100% relative information content, shown in Fig. 4.13. The maximum difference in all figures is roughly 6% of the maximum change of pressure of the FOM. As expected the maximum changes in the flowfield for the FOM as well as the ROMs are around the leading edge suction area and the shock location at roughly 70% chord length. When comparing the unweighted and the volume-weighted ROM the surface pressure around the shock position becomes less distinct, while slight deviations are visible throughout. Similar to the aerofoil, the volume-weighted ROM predicts a more smeared shock. Nevertheless,

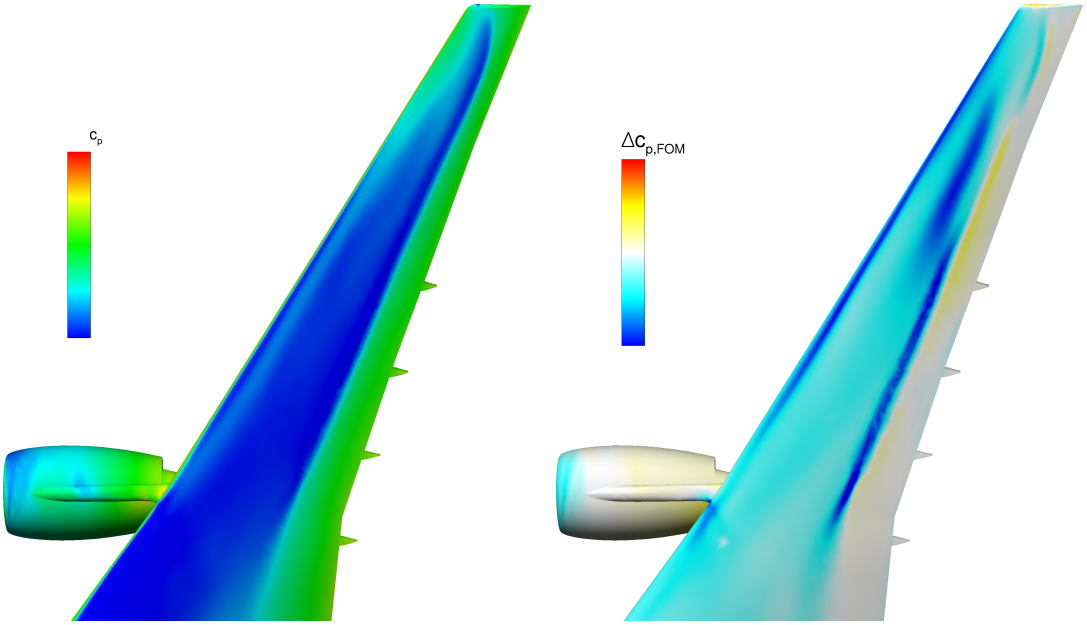

(a) Instantaneous surface pressure FOM

(b) Change in surface pressure FOM

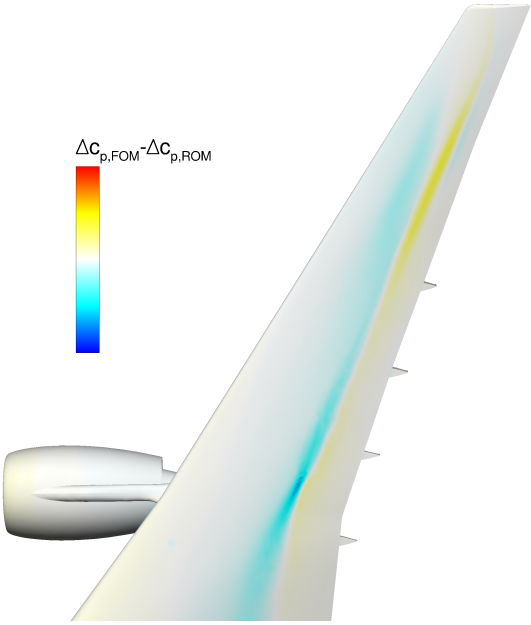

(c) Unweighted ROM $r_k = 100\%$

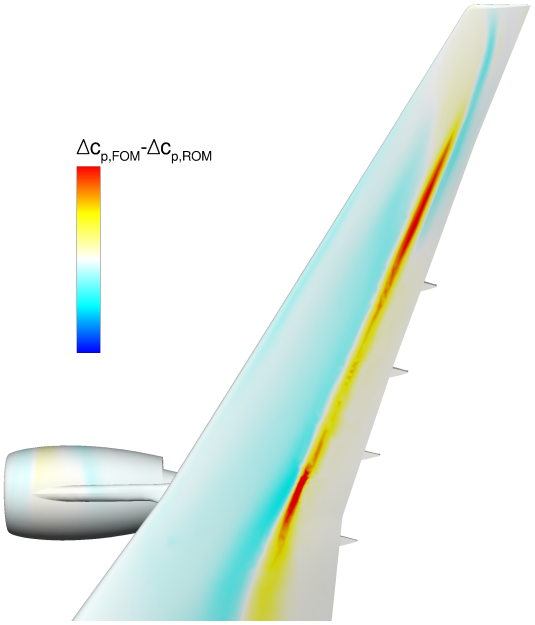

(d) Volume-weighted ROM $r_k = 100\%$

Figure 4.13: Investigation of unweighted and volume-weighted POD ROM using a 1-cos gust with $L_g = 116$ m for change in surface pressure at $\Delta C_{L,max}$. $M = 0.85$, $H = 10km$, $\alpha_0 \approx 2.5°$

both models offer accurate predictions at significantly decreased computational cost.

In the following results are presented for the volume-weighted ROM since a time-domain stable ROM is considered highly beneficial during the aircraft design and certification process. It not only allows to compute surface loads rapidly but further enables the connection to other subdisciplines more easily which is an essential requirement to

Table 4.1: Comparison of offline computational cost for volume-weighted POD ROM

Tasks 192 cores	Cost
Time-domain simulation	1
Reduced order model build-up (total cost)	0.441
a) Calculating snapshots	0.425
b) ROM construction	0.021

Table 4.2: Comparison of online computational cost for volume-weighted POD ROM

Tasks 1 core	Cost
Solving ROM for a single 1-cos gust	10^{-4}
Post-processing	
a) Rebuilding global coefficients	10^{-8}
b) Rebuilding surfaces loads	10^{-6}

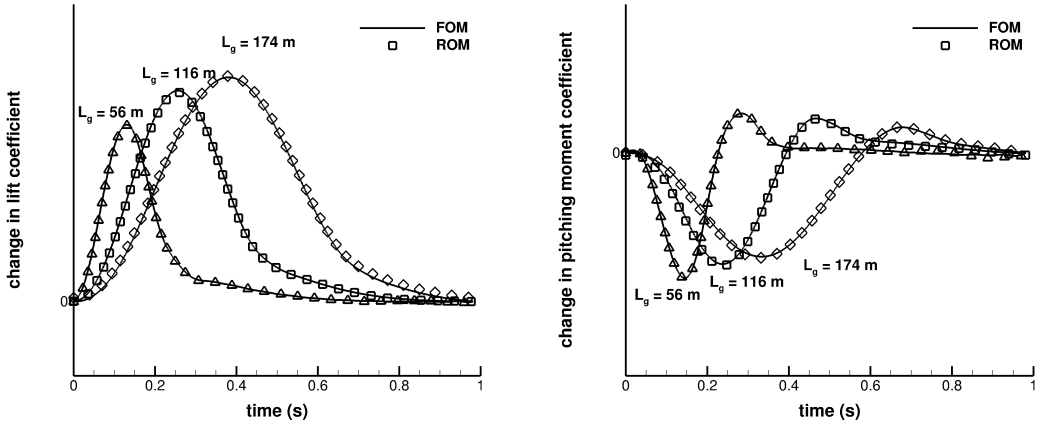

(a) Lift coefficient

(b) Pitching moment coefficient

Figure 4.14: Time histories of lift and pitching moment coefficient for 1-cos gusts with $L_g =$ 58 m, 116 m and 174 m. $M = 0.85$, $H = 10km$, $\alpha_0 \approx 2.5°$

progress towards CFD accurate unsteady loads. Significant reductions in size have been achieved compared to the FOM with only 39 instead of nearly 50 million. The accuracy is satisfying with an error below 1% and 6% for global coefficients and local surface pressure distributions, respectively.

Once the reduced order model is available, several 1-cos gusts can be analysed at negligible computational cost. Dynamic responses for the coefficient of lift for three different representative gust lengths, namely $L_g = 58$ m, 116 m and 174 m, are visualised in Fig. 4.14(a). Excellent agreement between the reduced model and the full order reference solutions is obtained for all gust lengths. Only minor differences occur around maximum lift as already discussed above. When looking at the pitching

moment coefficient in Fig. 4.14(b), again good agreement is found.

Computational cost for building the reduced order model, as well as for solving it, is summarised in Table 4.1 and 4.2, respectively. Since both the ROM and the unsteady time-marching approach require a steady-state solution, computational cost of the elastic trimming process is excluded. All values are non-dimensionalised by the computational cost of a full-order, time-domain reference solution. The most expensive part during the ROM generation is the frequency-domain sampling process with 0.425. Nevertheless, sampling all snapshots in frequency domain already offers a cost saving factor of about 2.5 compared to one full-order, unsteady time-marching solution. Constructing the ROM, including the build-up of the reduced Jacobian matrix $\mathcal{A}$ and projecting the gust influence matrix, costs an additional 0.021. Obtaining a 1-cos response in time domain using the ROM is approximately four orders of magnitude faster than solving the full order model, while global coefficients, such as lift and pitching moment, are available at essentially no additional cost. Furthermore, solving the ROM can be done on a local desktop computer, whereas a high power computing system is necessary for every time-marching reference solution. Reconstructing surface pressure distributions is computationally as expensive as solving the reduced model. Shear forces and moments, essential during the aircraft loads process, are produced together with the pressure distributions and come at no additional computational cost.

As for the frequency-domain method, this model has some limitations which should be mentioned here. In fact, nearly all limitations are directly inherited from the LFD sampling method. These are the need for a point of linearisation and the assumption of infinitesimally small amplitudes. For a more in-depth discussion of these, the interested reader is referred to Section 3.2. During the LFD analysis of the system also the inverse Fourier transform was discussed as one weakness since a cut-off points needs to be defined. If the ROM is evaluated in time-domain this point is not of direct concern since all frequencies are an inherent part of the solution. However, the prediction accuracy might be decreased since an extrapolation is done because samples are computed using the LFD method at distinct a-priori defined reduced frequencies. A possible alternative here might be utilizing the pulse excitation and transferring the obtained time history in the frequency domain.

Next, the model behaviour for certification amplitudes is analysed since these large amplitudes are crucial for the aircraft design. However, before that some words should be said about the different steps taken and the conclusions drawn from this. A POD based model reduction technique is outlined following a Galerkin projection approach. The resulting small sized system can then always be solved in frequency domain using the inverse Fourier transformation. If the system should be integrated in time, the reduced Jacobian matrix can not have any eigenvalues with positive real part. This is not the case for the classical POD method is used and instead a volume-weighted inner product has been applied. Whereas the reduced Jacobian matrix now only has

eigenvalues with negative real parts, the accuracy of the system decreases slightly. Within this work it has been found that the trade-off between stability and accuracay is well justified for an aircraft case since the ROM can be utilised more widely during the aircraft design and certification process which was one of the main goals throughout.

4.2.2 Application to Certification Requirement Conditions

Finally, the ROM is used to investigate a dynamic response to a realistic 1-cos gust as defined by the European Aviation Safety Agency in CS 25.341 [5]. The gust length is chosen as $L_g = 116$ m and the amplitude is nearly 7% of the freestream velocity. The change in lift coefficient and pitching moment coefficient over time is shown in Fig. 4.15. For the lift coefficient good agreement for the overall shape is observed, whereas minor differences occur around the maximum value as well as in the decay. In the FOM reference solution, the large gust amplitude causes the boundary layer over the wing to detach behind the shock from roughly 30% wing-span until the wing-tip. Since no boundary layer separation was present in the steady-state solution, this is a dynamically non-linear behaviour which, by definition, can not be represented by the linearised model. Note that in general linearised methods are capable of handling detached flows if this phenomena is already present in the steady-state solution as demonstrated for the aerofoil case 3 in Chapter 3. The minimum in pitching moment coefficient is still quite accurately predicted while the following maximum value is underpredicted. As before the strong gust amplitude causes a non-linear response which is even clearer visible for the moment coefficient. Since the ROM is based on LFD snapshots, the highest possible accuracy is the linearised frequency-domain solution, discussed also for non-linear responses in Chapter 3. Having said this, a complete breakdown of the ROM solution is not observed for the chosen flow conditions. This might not be the case in general when approaching edge-of-the-envelope conditions.

The absolute surface pressure difference at maximum lift coefficient is shown for the upper and lower surface in Fig. 4.16 to estimate the discrepancies when comparing both simulation techniques further. Since a dynamically non-linear response occurs during the time-domain analysis, which results in a decrease in amplitudes, the highest error arises around the shock location on the upper wing surface. In addition, some minor discrepancies are present around the leading edge, caused by the same amplitude mechanism. Besides these very localised errors, also the region downstream of the shock from roughly 30% to the wing-tip differ between FOM and ROM which is related to the aforementioned unsteady flow separation at the maximum lift coefficient. On the lower surface only some minor differences occur close to the wing-tip and leading edge. Even though the flow in the nacelle-pylon-wing junction area is fairly complex in the steady solution, a linearised model is accurate enough to predict its gust response behaviour even for certification gust amplitudes.

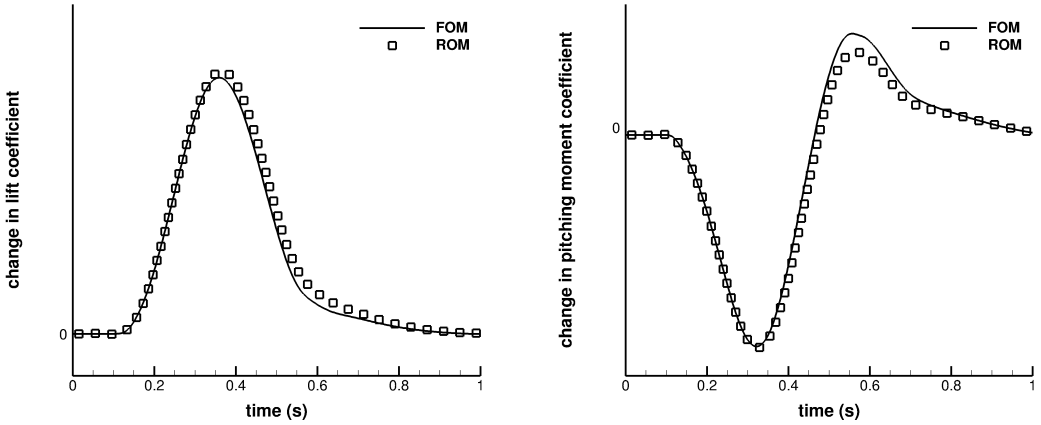

(a) Lift coefficient (b) Pitching moment coefficient

Figure 4.15: Time history of lift coefficient and pitching moment coefficient for 1-cos gust with $L_g = 116$ m and certification gust amplitude. $M = 0.85$, $H = 10km$, $\alpha_0 \approx 2.5°$

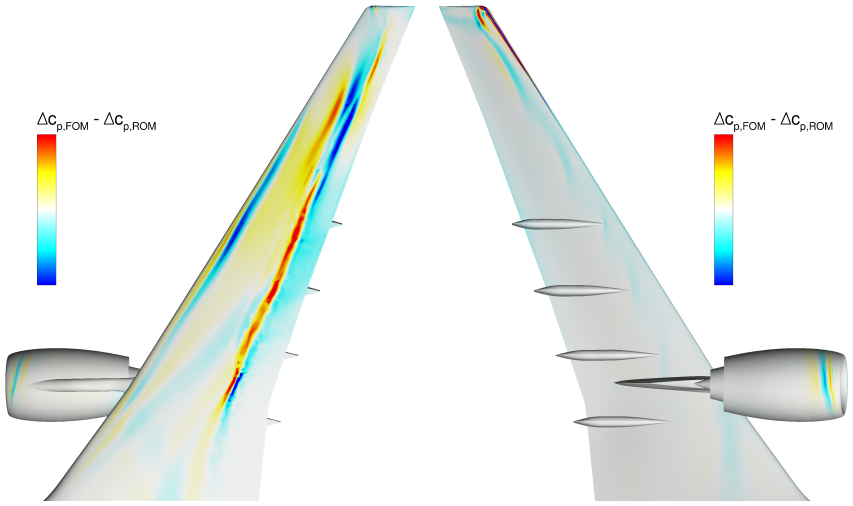

(a) Upper surface (b) Lower surface

Figure 4.16: Surface-pressure difference at peak load for 1-cos gust with $L_g = 116$ m and certification gust amplitude. $M = 0.85$, $H = 10km$, $\alpha_0 \approx 2.5°$

4.3 Summary on Aerodynamic Model Reduction

This chapter outlines a method to compute aerodynamic responses to gust encounter at two orders of magnitude reduced computational cost while preserving the accuracy of the underlying CFD solver. Modes are computed based on frequency-domain sampling data using POD and the operator of the RANS equations is then projected onto these modes. The cell volume can be included when computing the correlation matrix leading to the volume-weighted POD method which offers a stable ROM. Following the

projection, an arbitrary number of 1-cos gust responses can be obtained at negligible additional cost. Compared to the FOM, significant reductions in degrees of freedoms have been demonstrated for an aerofoil as well as a large civil aircraft while high accuracy was achieved. Recapitulating the three requirements discussed in Section 1.4 which are decrease in computational cost while retaining accuracy of the underlying CFD solver with a high level of automatisation, the proposed aerodynamic ROM fulfils all three of them for rigid gust response simulations. While the first two points are obvious, the reduced need in expert knowledge is achieved by the ROM formulation since it can be solved without any CFD knowledge. Nevertheless, while everything can be automated, setting up the process and generating the model still requires an experienced user.

Based on the presented aerodynamic ROM a couple of interesting questions arise. Currently the cell volume is considered for stabilising the reduced system which has a negative impact on the prediction accuracy. Instead, also the adjoint system could be sampled using a specific cost function such as change in lift coefficient with respect to fluid unknowns, and these computed additional sampling data could be used in a balanced model reduction. While this doubles upfront cost, the resulting model is ensured to be stable in time domain. In addition, gust loads analysis is an inherently multidisciplinary process and the inclusion of structural dynamics for the aircraft test case is of general interest and required by regulatory bodies. Since predicted loads for the aircraft case using the volume-weighted ROM are satisfying, the next chapter will focus on coupled fluid-structure analysis for the large civil aircraft.

Chapter 5

Aeroelastic Model Reduction

This chapter presents an aeroelastic reduced order modelling approach to decrease the large size of coupled fluid-structure systems which remains a problem in an industrial design and certification environment. The introduced ROM enables the use of high fidelity aerodynamic loads based on CFD in a wide range of multidisciplinary applications such as loads and aeroelasticity and aeroservoelasticity. Eigenmode decomposition (EMD) is introduced which is highly effective in representing structural dynamics behaviour and is constructed based on wind-off structural modes. However, for system responses not dominated by structural motion, the model does not provide accurate results. One solution to this is the inclusion of additional selected modes, such as originating in the aerodynamics. Thus, the POD model introduced in Chapter 4 is used as an extension and a coupled formulation is presented. The efficiency of this unified approach is exemplified for the large civil aircraft from previous chapters. Good agreement between results from full and reduced order model simulations is obtained throughout while computational cost has been reduced significantly. The reduced order model can be used in a versatile plug-and-play style approach to enhance selectively established industrial aircraft design processes. The majority of results in this chapter has been presented in [119].

A schematic representation of the aeroelastic model reduction approach is given in Fig. 5.1. As for the aerodynamic model reduction, the approach consists of a sampling, an offline and an online stage. Initially, a sampling is performed for the POD as well as EMD model by solving linearized system with either gust or motion-induced forcing terms for varying reduced frequencies. The gust sampling is discussed in Chapter. 3 while the POD mode computation is equivalent to the approach presented in Chapter. 4. Moreover, from an industrial perspective, the motion-induced sampling is necessary for analysing the flutter stability of the aeroelastic system which is mandatory during the aircraft design regardless of constructing the herein proposed ROM. During the offline stage, first, the EMD and POD model are constructed based on the previously computed snapshots. Secondly, modal bases are combined and the full order system is

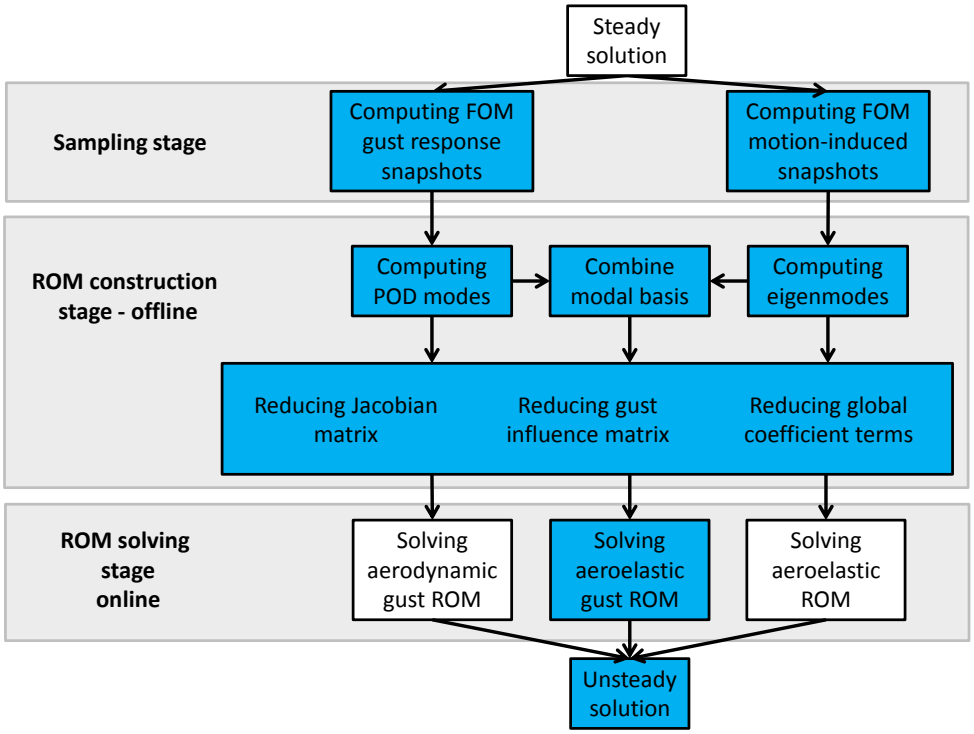

Figure 5.1: Schematic representation of aeroelastic model reduction approach

reduced and projected onto the combined modal subspace in a Petrov-Galerkin sense This includes the coupled Jacobian matrix, the gust influence matrix and additional terms used for the rapid reconstruction of global coefficients such as the lift coefficient. Once the model construction is done, the resulting small sized coupled system can be solved repeatedly for various different gusts during the online phase.

5.1 Large Civil Aircraft Case

The investigated test case in this chapter is the large civil aircraft which was introduced in Section 3.2 and further analysed in Section 4.2. After the elastic trimming is performed with 96 structural modes, the 15 most amplified structural modes are chosen and subsequently considered for modal reduction and dynamic responses. Several chosen 'in-vacuum' structural modes including a bending dominated as well as a torsion dominated mode are shown in Fig. 2.5 and have previously been discussed. Throughout, no structural damping is considered. The truncation of modes has been done to decrease the computational cost needed for the FOM as well as ROM investigations. Nevertheless, since the dynamic response of the both models is consistently investigated using these 15 modes, the applied truncation of modes does not impact the conclusions reached in developing the modelling tool.

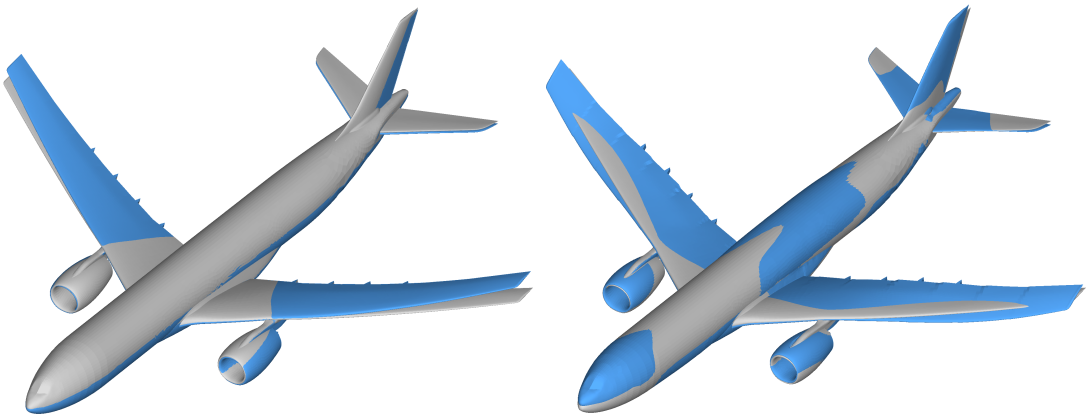

(a) Bending dominated eigenmode 1 (b) Torsion dominated eigenmode 13

Figure 5.2: A bending and torsion dominated wind-off eigenmode of large civil aircraft

5.1.1 Eigenmode Decomposition

Forced aerodynamic responses of theses structural modes are sampled at 12 reduced frequencies between 0 and 2 requiring overall 12×15 LFD solves. The sampling range is chosen based on the frequency range covered from the initial wind-off structural eigenmodes. The coupling between fluid-structure which is induced by generalised aerodynamic forces (GAFs) which are equivalent to the $Q(\omega^*)$ matrix

$$Q(\omega^*) = A_{sf}(A_{ff} - i\omega^*\mathcal{V})^{-1}A_{fs} \qquad \text{(2.54 revisited)}$$

and are shown for a bending (mode 1) and a torsion dominated mode (mode 13) which are displayed in Fig. 5.2. Note that, these modes are equivalent to the bending and torsion dominated mode in Fig. 2.5. Resulting GAFs are given in Fig. 5.3 for both modes and values have been scaled to one to qualitatively compare the different influences. Sampling locations are highlighted with a symbol. Especially modal deflections of the bending dominated mode cause a strong response of the wing torsion mode (GAF 13,1 in Fig. 5.3(c)). Instead, the influence of the torsion dominated mode on the bending dominated mode (GAF 1,13in Fig. 5.3(b)) is minor.

The evolution of the structural eigenvalues whilst affected by the fluid is then traced solving Eq. (2.55) at a starting altitude of 50 km until the target altitude of 10 km is reached. Resulting mode traces are shown in Fig. 5.4. With decreasing altitude the dynamic pressure increases and thus the coupling between the aerodynamics and structure becomes stronger due to increasing influence of GAFs. This coupling causes all modes to deviate from the imaginary axis towards a negative real part. Hence the system is stable. Even though the initial eigenmode was described by a single structural

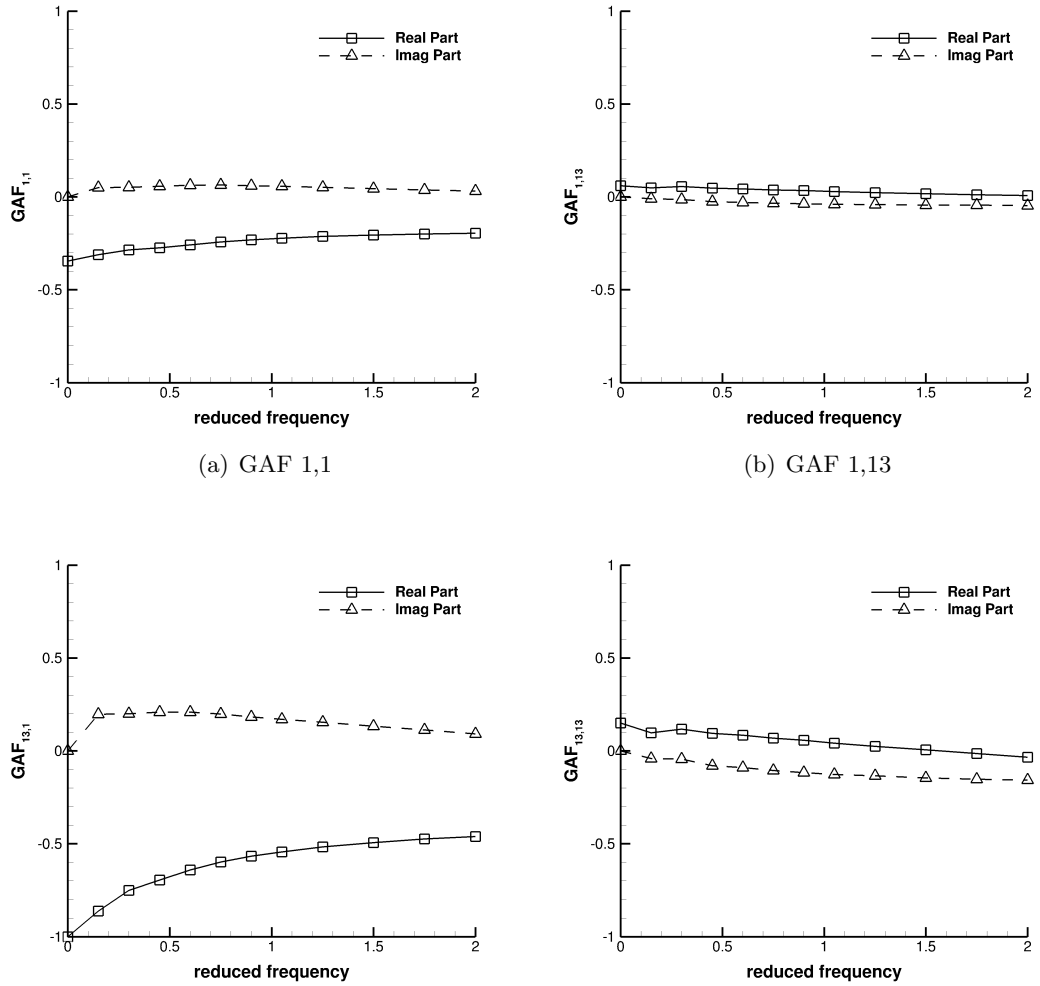

(a) GAF 1,1

(b) GAF 1,13

(c) GAF 13,1

(d) GAF 13,13

Figure 5.3: Generalised aerodynamic forces of large civil aircraft for bending and torsion dominated eigenmodes and their cross-correlations. $M = 0.85$, $H = 10km$, $\alpha_0 \approx 2.5°$

'in-vacuum' mode, resulting eigenmodes are a combination of all available 15 modes due to the aerodynamic coupling of the aeroelastic system.

The approximation of pk-type sampling is analysed by performing two iterations without simplifying Eq. (2.52). Since also the damping is considered in the term $(A_{\text{ff}} - \lambda\mathcal{V})$ (instead of $(A_{\text{ff}} - i\omega\mathcal{V})$) when tracing the eigenvalues, the method is referred to as p-type analysis to highlight the analogy to classic flutter investigations [150]. As an initial guess to the eigenvalues, the solution of the pk-type analysis of 10 km is used. For each eigenvalue one additional sample for all structural 'in-vacuum' modes using the real and imaginary part of the eigenvalue as a shift is computed and a single Newton solve is performed. This procedure can then be repeated until the desired number of p-type iterations is reached which is two in this case. For the here presented aircraft

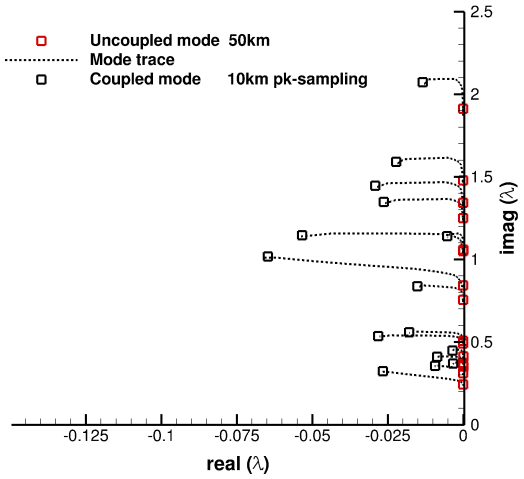

Figure 5.4: Evolution of eigenvalues λ during altitude tracing for pk-type sampling. $M = 0.85$, $H = 10km$, $\alpha_0 \approx 2.5°$

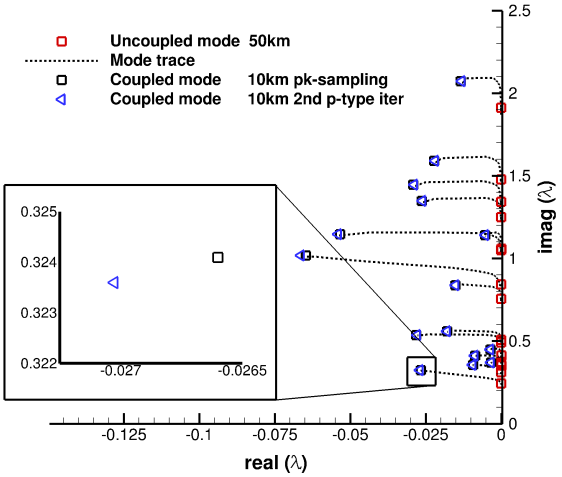

Figure 5.5: Evolution of eigenvalues λ during altitude tracing for p-type sampling. $M = 0.85$, $H = 10km$, $\alpha_0 \approx 2.5°$

model, this means that for each p-type iteration additional 225 (15 eigenvalues of interest times 15 structural 'in-vacuum' modes) LFD simulations are necessary. Thus, considering damping in the aerodynamic influence term during the eigenvalue trace is possible at increased computational cost. Deviations of the eigenvalues for all 15 modes are presented in Fig. 5.5. Note that a zoom is required to distinguish the approximated pk solution from the exact p-type. Minor deviations, especially for strongly damped eigenvalues, are present in the real part which reflects the neglected damping influence.

The fluid part of the left and right eigenvectors are computed, while discarding the real part of the eigenvalue, just as for the initial pk-type sampling. The magni-

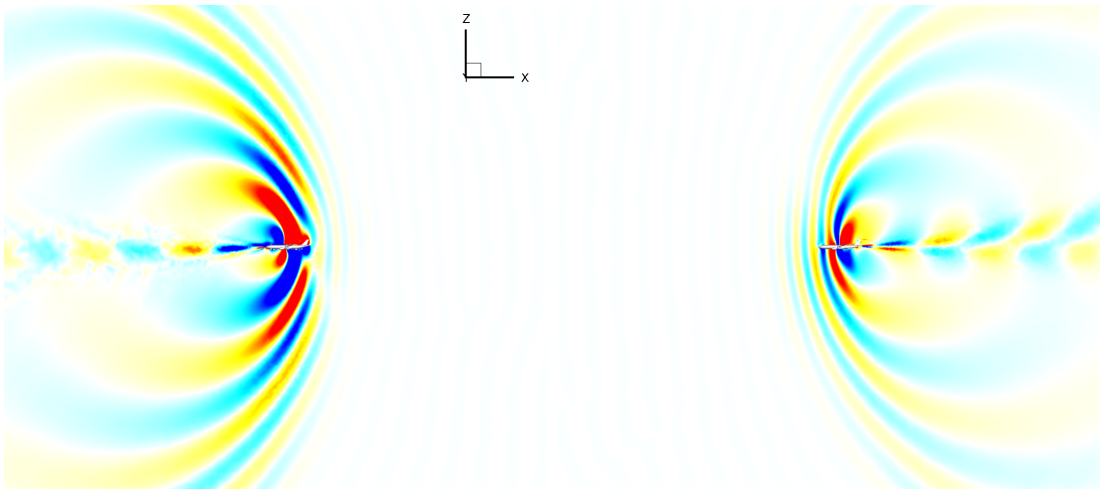

(a) Left eigenvector (b) Right eigenvector

Figure 5.6: Visualisation of first left and right eigenmode in the flowfield. $M = 0.85$, $H = 10km$, $\alpha_0 \approx 2.5°$

tude of pressure of the resulting first left and right eigenmode is visualised globally in Fig. 5.6 with the airframe centered. The right eigenmode indicates the regions within the flowfield which will respond once the eigenmode is excited. Since a transonic flow is investigated information is not travelling fully upstream. As expected strongest deviations occur above and below the aircraft and also in the wake region. The left eigenmode instead highlights regions where an excitation will cause a response of the eigenmode and can be seen as an indication of sensitive region for this particular eigenmode. In contrast the the right eigenmode mainly areas upstream of the airframe are sensitive. However, highest values again occur around the aircraft and upstream of the airframe.

For a more in-depth analysis, structural and fluid part of the first right eigenmode $\boldsymbol{\phi}_{\mathrm{EMD},1}$ are presented in Fig. 5.7. The structural deformation in Fig. 5.7(a) is multiplied by a factor to enhance visualisation. The surface deformation is a combination of all 15 'in-vacuum' structural mode shapes weighted by entries in $\boldsymbol{\phi}_s$ with the first mode imposing a bending-dominated deformation. The magnitude of pressure is shown in Fig. 5.7(b). It indicates the region in which the eigenmode has the highest influence on the pressure in the flowfield. Note that, since the whole flowfield is considered for the computation of eigenmodes, this mode not only affects the surface. Areas of high response are a combination of strong surface deflections and already pronounced flow behaviour in the steady-state surface pressure distribution such as the outboard-wing shock and the leading edge suction area at the tail plane.

As outlined in Section 2.2.2, complex-conjugates of all modes are included at no additional cost, and the coupled Jacobian and gust influence matrices are projected onto the model basis to reduce the system size from nearly 50 million to only 30

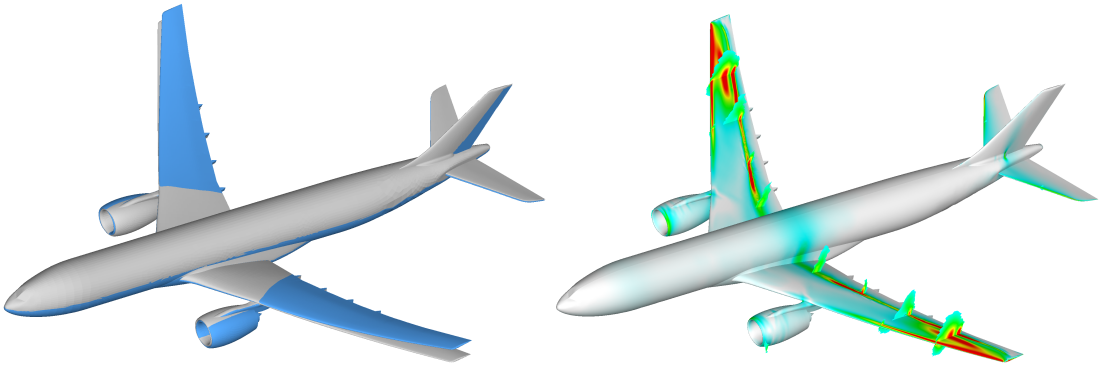

(a) Visualisation of structural part ϕ_s (b) Magnitude of pressure in ϕ_f

Figure 5.7: Visualisation of first right eigenmode $\phi_{\text{EMD},1}$ around airframe. $M = 0.85$, $H = 10km$, $\alpha_0 \approx 2.5°$

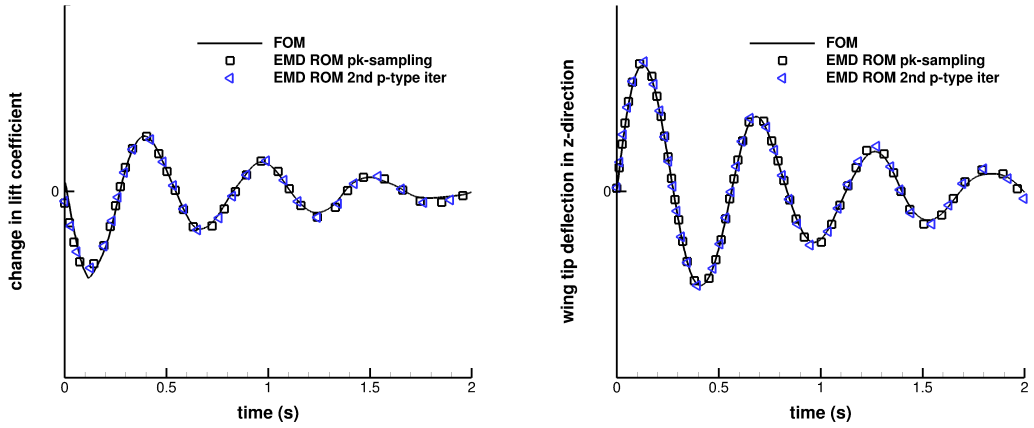

(a) Change in lift coefficient (b) Wing-tip deflection in z-direction

Figure 5.8: Initial disturbance response of EMD-based ROM for modal velocity excitation of 0.01 of the first mode. $M = 0.85$, $H = 10km$, $\alpha_0 \approx 2.5°$

degrees-of-freedom. As a first test, the system response to an initial disturbance in the modal velocity of 0.01 of the first mode is compared to the FOM reference solution for the change in lift coefficient as well as wingtip deflection in Fig. 5.8. Throughout good agreement is observed highlighting that the EMD ROM is an efficient model for structural driven excitations. Also the ROM after two p-type iterations has been constructed and results have been added to the figure without any differences to the pk-type ROM. This is expected since the approximated eigenvalues discussed in Fig. 5.5 are essentially equal.

Next, the generated EMD ROM is used to investigate the gust response of the flexible aircraft. The chosen gust parameters are $L_g = 116$ m, $v_{gz} = 0.0001\%$ of the freestream velocity and $x_0 = 5c_{ref}$, which is representative of a medium gust

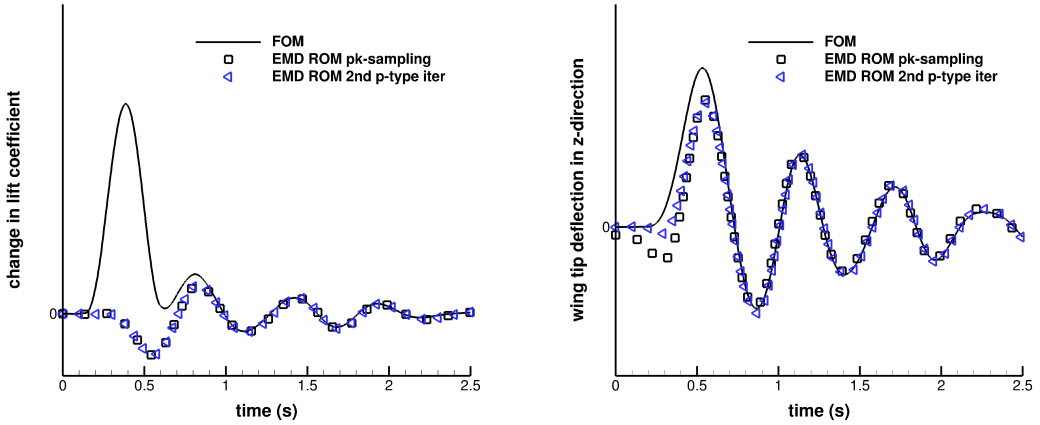

(a) Change in lift coefficient

(b) Wing-tip deflection in z-direction

Figure 5.9: Gust response of EMD-based ROM for 1-cos gust with $L_g = 116$ m. $M = 0.85$, $H = 10km$, $\alpha_0 \approx 2.5°$

length considering the certification requirements for large civil aircraft [5]. The small amplitude is imposed to ensure a dynamically linear response of the time-marching reference solution. The changes in lift coefficient and wing tip displacement in z-direction are displayed in Figs. 5.9(a) and 5.9(b), respectively. The ROM is not capable of reproducing the lift build-up due to the gust excitation, which effectively introduces an increment in angle of attack. However, once the gust has passed the aircraft and the change in lift is dominated by the damped structural response, the FOM and ROM predict a similar response. This behaviour can also be observed for the wing tip deflection even though not as distinct.

The gust response behaviour of the ROM after two p-type iterations is analysed to investigate the influence of the pk-approximation. Results are also shown in Fig. 5.9 with minor differences compared with the previous simplified pk model. The main difference is the initial condition for the wingtip deflection which causes some further deviations up until 0.5 s. Since the eigenvalues shown in Fig. 5.5 and the initial disturbance response in Fig. 5.8 do not change significantly, this difference in behaviour can be traced back to the eigenvectors which are computed once with and once without considering damping for the aerodynamic part. This difference in considered damping then influences the projection of the gust influence matrix during the model construction. However, when comparing computational cost needed for generating both models, the pk-type approximation outperforms the p-type ROM. For every p-type iteration step, roughly the same computational cost are necessary as needed for constructing the entire pk-type ROM. With two p-type iterations performed, the computational cost for computing the ROM which neglects damping is a factor of 3 less and thus only the ROM with pk-type approximation is analysed in the following. Moreover, it closely

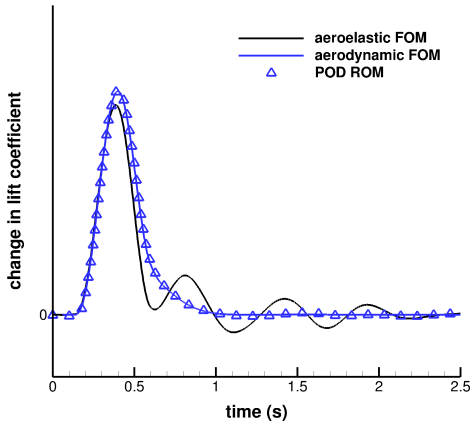

Figure 5.10: Change in lift coefficient to gust with $L_g = 116$ m for POD-based aerodynamics only ROM. $M = 0.85$, $H = 10km$, $\alpha_0 \approx 2.5°$

follows industrial standards on data generation. While the discussion of p- or pk-type sampling is a sitenote in this work, different numerical approaches to p-type CFD aerodynamics are still possible and worth investigating in the future. Especially during the analysis of flight-dynamics eigenmodes which have very low eigenfrequencies, p-type analysis might be necessary as indicated from initial results [151].

5.1.2 Aerodynamic Extension and Aeroelastic Analysis

In principle, the accuracy of responses to external excitation, such as gust, can be increased by enriching the modal basis with modes originating in the aerodynamic block A_{ff} of the coupled Jacobian matrix. In fact, this has been successfully applied for ROMs based on linear potential theory as demonstrated for a pitch-plunge aerofoil in [152]. The problem of this approach in combination with CFD-level aerodynamics is twofold. First, the size of the Jacobian matrix directly correlates with the mesh size as well as the number of conservative variables. For the presented case this results in approximately 50 million degrees-of-freedom and thus determining all eigenvalues, and selecting the eigenvalues of interest a-posteriori, is computationally prohibitive. Instead, computing a small number of eigenmodes for such problems is possible as demonstrated for stability analyses [90,91,153]. Secondly, for these approaches however, a region of interest needs to be defined a-priori which is currently not understood for gust responses. Thus, including eigenmodes from A_{ff} is considered not feasible and instead a subspace is approximated in the following using POD based on linearised responses of the aircraft to gust excitation.

The gust response of the aerodynamic subsystem is sampled at 20 reduced frequencies which are equally spaced between 0 and 2. Results and their corresponding complex-conjugates are used as snapshots to construct a POD ROM as outlined in Sec-

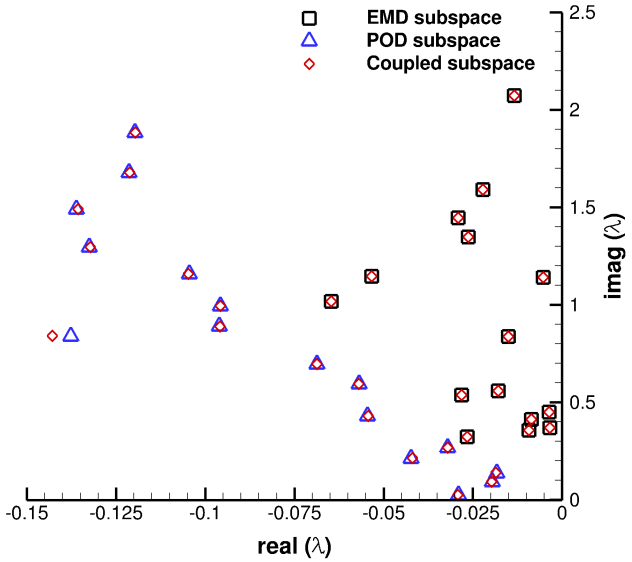

Figure 5.11: Eigenspectrum of reduced Jacobian matrix for POD, EMD and coupled ROM. $M = 0.85$, $H = 10km$, $\alpha_0 \approx 2.5°$

tion 2.2.1. For the model reduction all possible 39 POD modes are retained. Analysing the same gust parameters as for Fig. 5.9, the change in lift coefficient for a full-order, rigid aircraft gust response simulation and the POD ROM is shown in Fig. 5.10 with good agreement. Some minor deviations are visible in the ROM response after the gust has passed the aircraft, which is a result of the unsampled higher frequency range. However, critical peak loads are accurately predicted, thus the applied POD model is considered a reasonable compromise between computational cost and obtained accuracy. A more detailed discussion of the POD ROM for this particular case, including pressure distributions for the first mode and responses to different gust lengths, has been presented in Section 4.2. Moreover, the coupled FOM result is also displayed to highlight the need of an aeroelastic analysis rather than an aerodynamic one since peak loads are decreased and thus less conservative loads predictions are possible.

Both modal bases are combined by using the technique outlined in Sec. 2.2.3. Part of the coupled eigenspectrum of the projected coupled matrix, together with both individual solutions, is shown in Fig. 5.11. The dimension of the coupled ROM is 69 which is significantly smaller than that of the FOM with nearly 50 million. The influence of the multiplication with $(\Psi^H \mathcal{V} \Phi)^{-1}$ is expected to be small since the diagonal entries are equal one, due to $\Psi^H_{\text{EMD}} \mathcal{V} \Phi_{\text{EMD}} = I$ and $\Psi^H_{\text{POD}} \mathcal{V} \Phi_{\text{POD}} = I$. However, some eigenvalues, which originate from the POD system, experience a slight shift in real part whereas the imaginary part remains mostly unchanged. EMD-based eigenvalues, which are exact eigenvalues of the coupled problem, are basically unaffected by the ROM coupling. The coupled formulation now contains the subspace of both individual

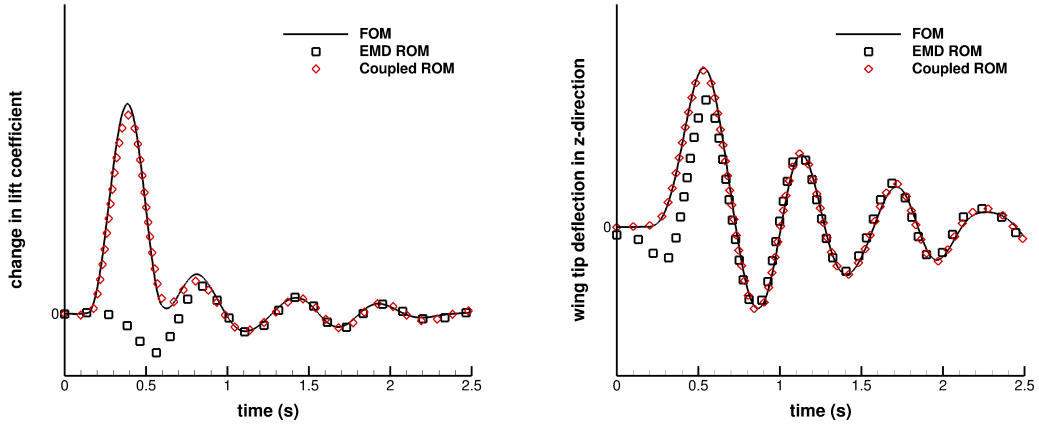

(a) Change in lift coefficient (b) Wing-tip deflection in z-direction

Figure 5.12: Response of global quantities of coupled ROM for 1-cos gust with $L_g = 116$ m. $M = 0.85$, $H = 10km$, $\alpha_0 \approx 2.5°$

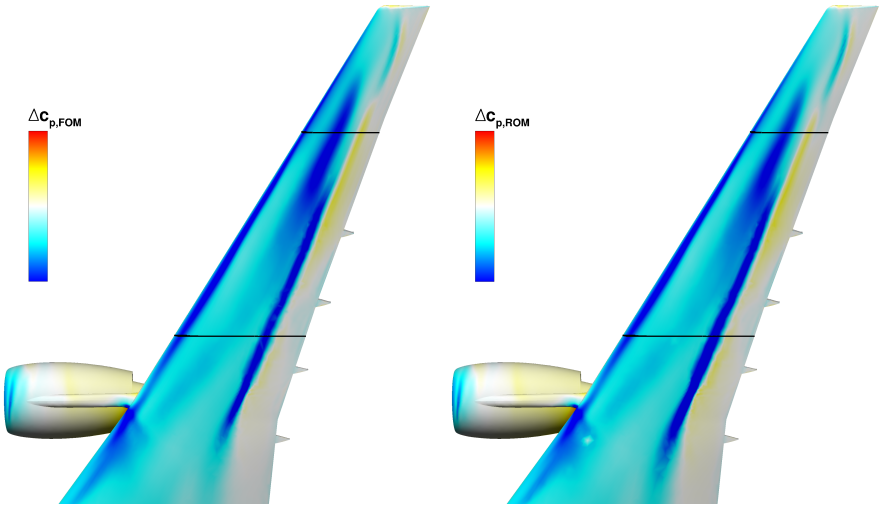

(a) $\boldsymbol{\Delta c_p}$ for FOM (b) $\boldsymbol{\Delta c_p}$ for ROM

Figure 5.13: Change in surface pressure distribution for FOM and coupled ROM for 1-cos gust with $L_g = 116$ m at $C_{L,max}$. Black lines indicate extracted slices. $M = 0.85$, $H = 10km$, $\alpha_0 \approx 2.5°$

ROMs and thus is capable of predicting a coupled fluid-structure response subject to gust excitation.

The resulting ROM is now used to investigate the same gust parameters as in Section 5.1.1. The changes in lift coefficient and wing tip displacement in z-direction are shown in Figs. 5.12(a) and 5.12(b), respectively. For both quantities of interest an improvement is observed. The ROM correctly predicts the change in lift coefficient while these changes are dominated by the gust excitation. Some minor differences occur

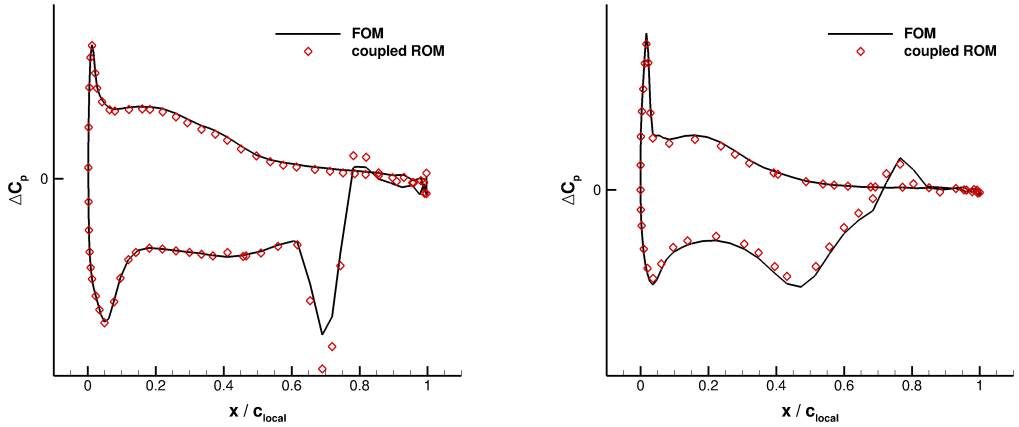

(a) $\boldsymbol{\Delta c_p}$ at 40% semi-wingspan

(b) $\boldsymbol{\Delta c_p}$ at 80% semi-wingspan

Figure 5.14: Change in pressure distribution for FOM and coupled ROM for 1-cos gust with $L_g = 116$ m at selected spanwise stations. $M = 0.85$, $H = 10km$, $\alpha_0 \approx 2.5°$

around the peak value and during the transition from an aerodynamically dominated response to structurally dominated behaviour around 0.7 s. The wing tip deflection shows an even better improvement making the predictions nearly indistinguishable. The ROM not only offers global coefficients and structural degrees-of-freedom at greatly reduced cost but also gives access to the flow topology of the whole domain. This is critical particularly for loads computations. Thus, the change in surface pressure at the peak lift value is presented in Figs. 5.13(a) and 5.13(b) for the FOM and ROM, respectively. Overall good agreement is observed with some minor differences close to the wing tip and in the engine-pylon-wing region. Based on the presented surface pressures sectional loads and root wing bending moments are readily accessible. In addition, local changes in surface pressure distribution have been extracted at 40% and 80% semi-wingspan. Results are compared in Fig. 5.14 between FOM and ROM with good agreement. Small deviations are visible around the shock location for the inboard pressure distribution whereas reference results are closely matched elsewhere.

Once the ROM is verified for a single 1-cos gust, arbitrary gust lengths can be analysed at negligible additional computational cost. Dynamic responses for the change in lift coefficient for two representative gust lengths of $L_g = 18$ m and 214 m, are provided in Fig. 5.15(a). These correspond to about the shortest and longest gust lengths, respectively, as defined by certification requirements. Excellent agreement between the reduced model and the full order reference solutions is obtained for the longer gust length. Minor differences occur around maximum lift for the shorter gust length due to the low frequency POD sampling. The dynamic response of the wing tip deflection in Fig. 5.15(b) shows good agreement throughout. To further enhance the accuracy 5 additional samples between 2 and 5 have been added and the model

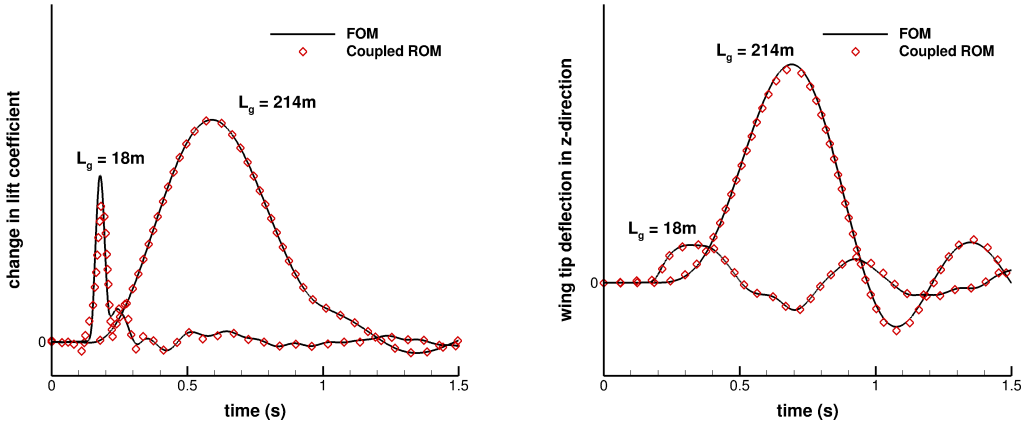

(a) Change in lift coefficient (b) Wing-tip deflection in z-direction

Figure 5.15: Gust responses of coupled ROM for 1-cos gusts with $L_g = 18$ m and $L_g = 214$ m. $M = 0.85$, $H = 10km$, $\alpha_0 \approx 2.5°$

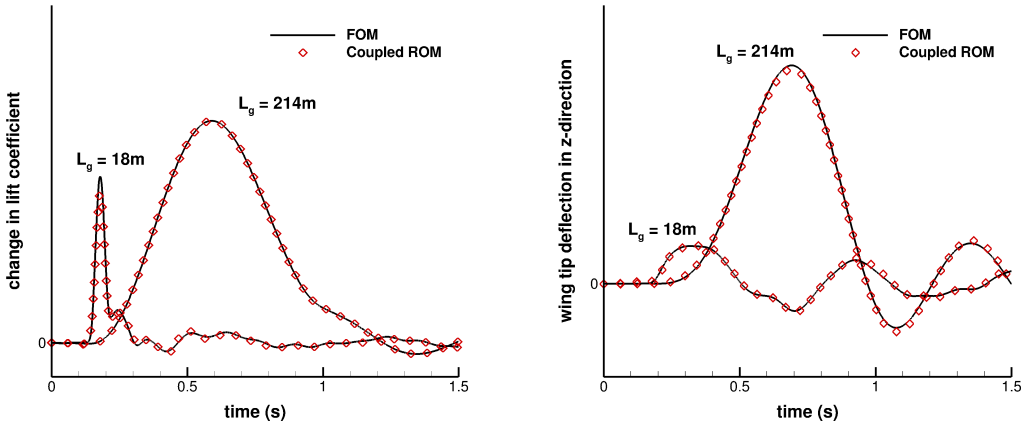

(a) Change in lift coefficient (b) Wing-tip deflection in z-direction

Figure 5.16: Gust responses of coupled ROM for 1-cos gusts with $L_g = 18$ m and $L_g = 214$ m with updated POD submodel (79 instead of 69 modes) including a larger reduced frequency range to enhance shortest gust length predictions. $M = 0.85$, $H = 10km$, $\alpha_0 \approx 2.5°$

construction has been repeated. The resulting system response for the short and longest gust are shown in Fig. 5.16. Whereas the longest gust response remains unchanged the accuracy for the change in lift coefficient for $L_g = 18$ m increases.

Computational cost is summarised in Tables 5.1 and 5.2 for the offline and online phase, respectively. Timings were obtained on the high performance computing facility ARCHER[1] using 192 standard compute cores. Since the computational time for a time-domain 1-cos simulation depends on the investigated gust length, the time listed are

[1] Advanced Research Computing High End Resource

Table 5.1: Comparison of offline computational cost for aircraft case

Tasks 192 cores	Cost
Time-domain simulation (single 1-cos response)	1
Reduced order model build-up (total cost)	2.55
a) Sampling EMD basis	2.28
b) Sampling POD basis	0.25
c) Constructing coupled ROM	0.02

normalised to 1 is an average of all three presented gust responses. In real time-units, it took 47h. The normalised time of 2.55 for the ROM generation contains the time needed for producing all pk-type sampling data and the subsequent coupled model construction. Solving the ROM can afterwards be done on a single core desktop computer and requires roughly three orders of magnitude less computational costs than a FOM solve, again slightly depending on the gust length of interest. It should be noted that roughly 95% of this time is needed for forming the matrix-vector product $\Psi^H \frac{\partial \mathbf{R}}{\partial \boldsymbol{v}_\mathrm{g}} \Delta \boldsymbol{v}_\mathrm{g}$ since this is performed over the full-order dimension. Approximations of this term can be investigated in the future, e.g. by applying a hyper-reduction technique. Cost for reconstruction of global coefficients, surface pressure distributions and structural deformations is negligible. Also, as demonstrated above, the ROM can be used to investigate a wide range of gust parameters without recomputing it, assuming the frequency range of interest is covered. Thus, the ROM method offers a speed-up compared to time-marching, coupled fluid-structure simulations if more than two different sets of gust parameters are required. Based on the acceptable means of compliance [146], published together with the certification requirements, around 30 different sets of gust parameters are of interest at one flight point which results in a speed-up factor of one order of magnitude using the ROM approach presented herein when considering construction and solving cost. If only online cost are of concern, the achieved speed-up increases to roughly four orders of magnitude.

It shall be emphasised that most of the data generated for the EMD basis construction is required already when using the frequency domain CFD model for aerodynamic database generation and aeroelastic stability prediction. Thus the actual speed-up will be higher than stated, when integrated within the entire tool chain. Moreover, gust responses analysis need to be performed accounting for a change in mass model, flight point and structural state summing up to several hundreds of flight points. The speed-up of roughly a factor of 20 applies to all of these combinations of parameters and therefore a consistent, higher fidelity CFD-based gust response analysis is possible using the herein proposed model reduction techniques. When accounting for the simultaneously possible flutter analysis an even higher speed-up is practically possible and the consistency between CFD-based stability and transient response simulations is further enhanced.

Table 5.2: Comparison of online computational cost for aircraft case

Tasks 1 core	Cost
Solving ROM for a single 1-cos gust	10^{-3}
Post-processing	
a) Rebuilding global coefficients	10^{-8}
b) Rebuilding surfaces loads	10^{-6}

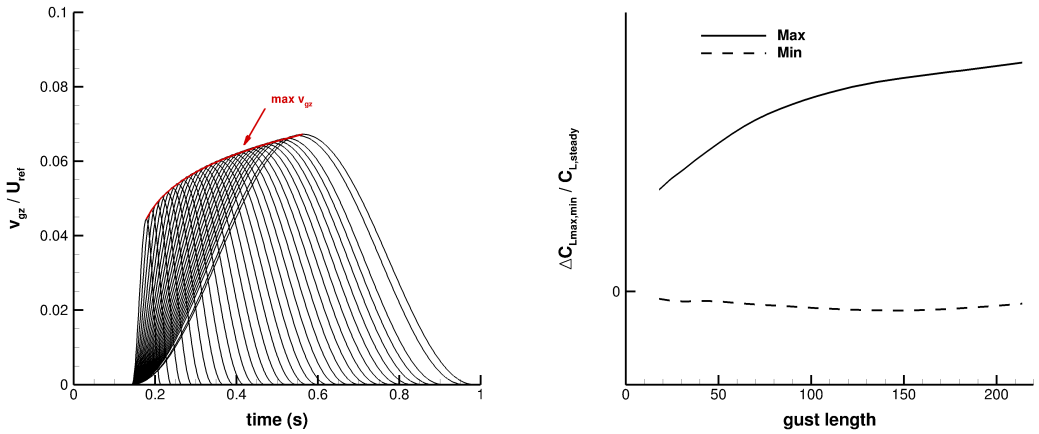

(a) Gust disturbances over time

(b) Change in lift coefficient

(c) Change in pitching moment coefficient

(d) Wing-tip deflection

Figure 5.17: Gust disturbances over time as defined by international certification requirements and aeroelastic maximum and minimum values for change in lift coefficient, pitching moment coefficient and wingtip deflection. $M = 0.85$, $H = 10km$, $\alpha_0 \approx 2.5°$

5.1.3 Application to Certification Requirements

Finally, the aeroelastic ROM can be used to investigate all 30 different gust length defined by international certification requirements with their corresponding amplitudes.

All gust excitations over time are shown in Fig. 5.17(a). Additional details on how to compute a gust amplitude for a certain gust length are given in Appendix A.

For each of the simulations, the maximum and minimum value for the change in lift coefficient, pitching moment coefficient and wingtip deflection is then extracted and displayed in Fig. 5.17. Whereas maximum values of the change in lift coefficient and wingtip deflection follow the increase of gust amplitude over gust length, the change in pitching moment coefficient exhibits a maximum around a gust length of 150 m. However, differences in the maximum change in pitching moment are not substantial. This indicates that the coupled aeroelastic system is still largely dominated by the gust excitation. For the minimum values, the wingtip deflection has its global minima at around a gust length of 130 m, which correlates to the eigenfrequency of the first coupled eigenmode which is largely wing bending dominated. As a next step during a gust response analysis for an aircraft design cycle, one would extract sectional forces and moments and include these during the structural sizing process if they are limiting loads. These sectional forces are readily available, as demonstrated in Chapter 3.2.2.

The computational cost for analysing all gust lengths above was around 2 hours on a local desktop computer, whereas the FOM equivalent would have taken a few weeks to run on an HPC. This again highlights the possibility that is offered by reduced order modelling to incorporate high fidelity aerodynamic loads in the aircraft design and certification process at costs comparable to classical panel based methods. Since the model construction can be done offline and thus time-independent from the final analysis, the ROM can provide accurate loads on demand.

5.2 Summary on Aeroelastic Reduced Order Modelling

This chapter outlined a method for model order reduction to compute coupled fluid-structure gust responses at low computational cost while preserving the accuracy of the underlying computational fluid dynamics solver. Throughout, a modal decomposition and projection philosophy is followed. Structural deformations are accounted for by considering aeroelastic eigenmodes which originate from the structure. This basis is then expanded by adding proper orthogonal decomposition modes to enhance the prediction accuracy during gust encounter. The linearised operator of the Reynolds-averaged Navier–Stokes equation is projected onto the subspace in a Petrov–Galerkin sense. Once the reduced model is constructed, a large number of gust responses can be obtained at negligible computational cost on a local desktop machine.

The efficiency of the proposed method has been demonstrated using an elastically-trimmed large civil aircraft at transonic flight conditions. The combined reduced order model decreases the number of degrees of freedom from nearly 50 million to just 69 while good agreement with full order reference solutions has been shown. Computational cost is discussed to evaluate the efficiency gain provided by the proposed model

reduction. Feasibility of rapid turnaround time using computational fluid dynamics in the industrial aeroelastic loads context is demonstrated, which presents a step towards the ambition of virtual aircraft design and certification. The proposed reduced order model can now be selectively included in established industrial processes during the design and certification period by either substituting an existing method or adding additional high fidelity information.

Chapter 6

Conclusions

The aim of this work was to establish methods that enable the routine use of computational fluid dynamics for dynamic gust loads analysis during the aircraft design and certification process. The use of highly accurate gust loads increases the prediction accuracy and therefore offers potential for more efficient aircraft. However, computational cost necessary for full order time-marching simulations are not affordable during industrial design cycles. Three challenges have been identified to meet industrial requirements; high accuracy/fidelity, low computational cost/time, automated and integrated tools. First, the accuracy of predicted loads should be equivalent to the underlying computational fluid dynamics model and ideally matches wind tunnel and in-flight test data. Secondly, turnaround time necessary to generate solutions needs to be reduced significantly compared to full order unsteady time-marching simulations. Thirdly, required expert knowledge to apply the developed software tools should be reduced as much as possible. For instance currently used tools, specifically corrected Doublet Lattice method requires detailed understanding of the complete dynamical system to apply such corrections to carefully selected modes.

These challenges have been addressed by following three steps. First, the so-called linearised frequency domain method has been extended towards gust response simulations. Secondly, an aerodynamic reduced order model has been introduced computing dominant modes with proper orthogonal decomposition and projecting the linearised operator of the Reynolds-averaged Navier–Stokes equations onto the subspace spanned by these modes. Thirdly, a modal basis for aeroelastic analysis has been computed by combining the aforementioned aerodynamic proper orthogonal decomposition modes with aeroelastic eigenmodes. All methods have been successfully demonstrated on a test case of industrial interest. While computational cost has been reduced significantly by two orders of magnitude, steady non-linear aerodynamic effects are accounted for. Moreover, highly accurate loads predictions are available by solving a small sized system on a desktop machine enabling other subdisciplines to include these loads in their respective process chains. Thus, this work presents a step towards establishing com-

putational fluid dynamics as the main source of unsteady aerodynamic data for gust loads analysis during the aircraft design and certification process.

In Chapter 2, the theoretical background of full and reduced order analysis is presented. The Reynolds-averaged Navier–Stokes equations are introduced and turbulence modelling is discussed briefly. Afterwards, steps to linearise the governing equations around a non-linear steady solution are outlined and a right-hand side gust forcing term is proposed. Also, reconstruction of aperiodic time-domain solutions using an incomplete, inverse Fourier transform based on sinusoidal data at individual frequencies is discussed. The second half of this chapter focuses on projection based reduced order modelling and introduces the core concepts of proper orthogonal decomposition as well as eigenmode decomposition. The two reduced bases are finally combined in a unified formulation for the investigation of aeroelastic responses to gust excitation.

The proposed time-linearised method for gust responses is verified in Chapter 3. Results have been presented for an aerofoil in different flow regimes and a large civil aircraft near cruise condition. Several sinusoidal gust responses are computed and results are compared to an unsteady time-marching approach with excellent agreement for global coefficients as well as surface pressure distributions. Different aperiodic 1-cos gusts are reconstructed using superposition in conjunction with an incomplete, inverse Fourier transform again with good agreement to the reference solutions. Computational cost has been reduced by two orders of magnitude while steady non-linear effects are accounted for. Since the current industrial gust loads analysis process is also based on frequency-domain sampling, the herein presented approach enables the substitution of computational fluid dynamics without significant changes to an existing process chain.

In Chapter 4, a method is presented and verified to compute aerodynamic responses to gust encounter at several orders of magnitude reduced computational cost while preserving the accuracy of the underlying computational fluid dynamics solver. Constructing the reduced model requires sampling at a few frequencies and proper orthogonal decomposition. The resulting modal basis is used to project the linearised operator of the Reynolds-averaged Navier–Stokes equations. Once the reduced model is generated an arbitrary number of 1-cos gust responses can be obtained at negligible computational cost on a local desktop machine. Results have been presented for an aerofoil in transonic flow and the same passenger aircraft analysed before with excellent agreement. The proposed model enables the inclusion of unsteady highly accurate aerodynamic loads in cases where a rapid evaluation is essential and no high performance computing systems are desirable such as control design.

Chapter 5 extends the aerodynamic reduced order model towards a coupled fluid-structure analysis. Aeroelastic eigenmodes which originate from the structural subsystem are computed. Additional modes to model the gust response behaviour are obtained by applying proper orthogonal decomposition as discussed in Chapter 4. The linearised operator of the coupled aeroelastic system is projected onto the unified sub-

space in a Petrov–Galerkin sense. Results are presented for the large civil aircraft case used throughout to demonstrate the industrial readiness of the proposed method. The degrees of freedom were reduced to just 69 from initially nearly 50 million. Thus, computational cost of an aeroelastic gust response analysis has been reduced by two orders of magnitude compared to full order, time-marching analysis including the construction of the reduced model while accuracy has been preserved. It shall be emphasised that most of the data generated for the modal basis construction is required already when using the frequency-domain computational fluid dynamics model for aerodynamic database generation and aeroelastic stability prediction. Therefore, the actual speed-up will be higher than stated, when considering the entire aircraft design and certification process and looking at the tools presented in this work as modular add-ons.

6.1 Future Work

Various future directions could be pursued based on the work presented here which could be categorised according to technical readiness. First, the proposed methods could be extended from an academic point of view within the lower levels of the technical readiness scheme (mainly 1 to 3). Secondly, computational fluid dynamics should be established as the main source for unsteady aerodynamic data during the aircraft design which correlates to a relatively high technical readiness level of 4 to 6.

From a research point of view and thus low technical readiness level, the proper orthogonal decomposition based reduced order model in Chapter 4 could be replaced with its balanced counterpart. This might improve accuracy and offer an even higher reduction in system size while stability in time domain without any additional steps is ensured. Required steps for adoption of balanced proper orthogonal decomposition should be straightforward since only samples from the adjoint system are needed additionally which is already established during the left eigenvector computation. Resulting modes could then be used in the coupled model formulation just as the gust modes discussed herein. Note the similarity with the right/direct and left/adjoint eigenmode basis.

In Section 2.2.2 the investigation of the initial value problem for transient growth behaviour as an additional to the eigenmode based response analysis was already briefly mentioned. Since the fluid dynamics community has impressively demonstrated that the short- and long-term response behaviour of a system governed by a non-normal Jacobian matrix can significantly differ [140], it might be worth pursuing this additional type of response analysis also for aeroelastic system response at transonic flow conditions. In fact, nearly all necessary ingredients (eigenvalues, left and right eigenmodes) have already been computed and discussed within this work and might provide an even better understanding of the complex, underlying physical phenomena. Moreover, the author expects that the inclusion of short-term response behaviour will become even

more prominent if not mandatory once more unstable, vortex-dominated configuration will be of interest.

In Section 3.2, it was demonstrated that dynamically non-linear effects cause full and reduced order solutions to differ. Thus, discussion of dynamically non-linear effects will further improve prediction accuracy beyond linear amplitudes. Preliminary promising results have been demonstrated using a harmonic balance method for an aerofoil under gust excitation [135]. However, the reduction in computational cost which is achievable when applying harmonic balance instead of time-linearised methods decreases significantly. For the reduced order model framework discussed herein, the inclusion of higher order terms in the Taylor expansion has shown good results for small test cases based on potential flow theory [152]. The inclusion of such higher order terms in the Taylor expansion when considering computational fluid dynamics has not been successfully demonstrated yet and might bring another level of prediction accuracy and range of applications.

While not discussed within this work, non-linearities might also originate from the structural model. These are currently not accounted for since a linear modal structural model is used. With the aim to decrease structural weight during the aircraft design by applying aeroelastic tailoring, more leightweight structures and/or modern composite materials, the assumption of a linear structural behaviour becomes more and more questionable. Instead, similar to the aerodynamic system also the non-linear structural system could be linearised around a non-linear steady solution and modes could then be traced for the coupled system.

An extension of the eigenmode decomposition based model towards flight dynamics degrees of freedom is necessary to fulfil certification requirements. In a parallel and related project, work has been presented on how to efficiently alter the Schur formulation for rigid body modes [151]. The herein presented proper orthogonal decomposition approach has been applied for a preliminary investigation of free-free aircraft gust encounter, using the same aircraft case. Obtained results are as satisfying as for the fluid-structure coupled system. Investigation of lateral excitations and free-flying, elastic aircraft under gust excitations is ongoing.

From an industrial point of view and thus higher technical readiness levels, investigating the proposed coupled reduced order model during aircraft design and optimisation will enable other subdisciplines to access computational fluid dynamics based loads and improve their own predictions as mentioned throughout this work. For example, the application of computational fluid dynamics loads for the prediction of edge-of-the-envelope multiphysics and accounting for the predicted loads already at initial stages of the design is expected to bring a significant increase in physical knowledge earlier. As another example, the inclusion of a control system to perform gust load alleviation should be mentioned. While current industrial practice is based on steady computational aerodynamics data in combination with quasi-steady potential theory for

unsteady loads, the presented reduced order model offers computational aerodynamics loads also for unsteady responses.

A significant decision driver for industry to consider new methods during aircraft design is to achieve certification also for improved process chains which rely on new, more accurate methods. In fact, to solely base unsteady loads predictions on computational aerodynamic methods, the certification aspect is crucial and should not be underestimated. So far, the linearised frequency-domain method for gust responses proposed herein is investigated within industry and work to obtain certification for their process chains and correlated tools including the linearised frequency domain method for gust is ongoing.

Bibliography

[1] Wright, O., *How We Invented the Airplane*, Harper Magazine, 1955.

[2] Etkin, B., "Turbulent Wind and Its Effect on Flight," *Journal of Aircraft*, Vol. 18, No. 5, 1981, pp. 327–345.

[3] Hoblit, F. M., *Gust Loads on Aircraft: Concepts and Applications*, American Institute of Aeronautics & Astronautics, 1988.

[4] Brunstein, A. I., "Clear Air Turbulence Accidents," *SAFE Journal*, Vol. 8, 1978.

[5] European Aviation Safety Agency, "Certification Specifications for Large Aeroplanes (CS-25)," 2015.

[6] Wagner, H., "Über die Entstehung des dynamischen Auftriebs von Tragflügeln," *Zeitschrift für angewandte Mathematik und Mechanik*, Vol. 5, No. 1, 1925, pp. 17–35.

[7] Küssner, H. G., "Zusammenfassender Bericht über den instationären Auftrieb von Flügeln," *Luftfahrtforschung*, Vol. 13, No. 2, 1936, pp. 410–424.

[8] Theodorsen, T., "General Theory of Aerodynamic Instability and the Mechanism of Flutter," Tech. Rep. 496, NACA, 1935.

[9] Sears, W. R., "On the Reaction of an Elastic Wing to Vertical Gusts," *Journal of the Aeronautical Sciences*, Vol. 8, No. 2, 1941, pp. 64–67.

[10] Jones, R. T., "The unsteady lift of a wing with finite aspect ratio," Tech. rep., NACA TR-641, 1940.

[11] Wright, J. R. and Cooper, J. E., *Introduction to Aircraft Aeroelasticity and Loads*, John Wiley & Sons, 2007.

[12] Albano, E. and Rodden, W. P., "A Doublet Lattice Method for Calculating Lift Distribution on Oscillating Surfaces in Subsonic Flow," *AIAA Journal*, Vol. 7, No. 2, 1969, pp. 279–285.

[13] Blair, M., "A compilation of the mathematics leading to the doublet lattice method," Tech. Rep. WL-TR-92-3028, NASA, 1992.

[14] Rodrigues, E. A. and Kamiyama, M. T., "Computation of Dynamic Loads on Aircraft Structure due to Continuous Gust using MSC/NASTRAN," *MacNeal-Schwendler Co*, Vol. 1, No. 1, 1997, pp. 1–17.

[15] Chudý, P., "Response of a Light Aircraft Under Gust Loads," *Acta Polytechnica*, Vol. 44, No. 2, 2004, pp. 97–102.

[16] Kier, T., "Comparison of Unsteady Aerodynamic Modelling Methodologies with Respect to Flight Loads Analysis," *AIAA Atmospheric Flight Mechanics Conference and Exhibit*, 2005, AIAA 2005-6027.

[17] Brink-Spalink, J. and Bruns, J., "Correction of unsteady aerodynamic influence coefficients using experimental or CFD data," *International Forum on Aeroelasticity and Structural Dynamics*, 2001, IFASD 2001-034.

[18] Palacios, R., Climent, H., and Karlsson, A., "Assessment of strategies for correcting linear unsteady aerodynamics using CFD or experimental results," *Progress in computational flow-structure interaction*, 2003, pp. 209–224.

[19] Giesing, J. P., Kalman, T. P., and Rodden, W. P., "Correcton factor techniques for improving aerodynamic prediction methods," Tech. Rep. NASA CR-144967, NASA, 1976.

[20] Garner, H. C., "A Practical Approach to the Prediction of Oscillatory Pressure Distributions on Wings in Supercritical Flow," Tech. Rep. CP 1356, Aeronautical Research Council, 1976.

[21] Pitt, D. M. and Goodman, C. E., "Flutter Calculations using Doublet Lattice Aerodynamics modified by the Full Potential Flow Equations," *28th AIAA/ASME/ASCE/AHS Structures, Structural Dynamics and Materials Conference*, 1987, AIAA 87-0882-CP.

[22] Silva, R., Mello, O., and Azevedo, J., "Transonic Flutter Calculations based on Assumed Mode Shapes Corrections," *International Forum of Aeroeasticity and Structural Dynamics*, 2001.

[23] Jadic, I., Hartlet, D., and Giri, J., "An enhanced correction factor technique for aerodynamic influence coefficient methods," *MSC's proceedings for 1999 Aerospace User's Conference*, 1999.

[24] Chen, P. C., Silva, R. G. A., and Liu, D. D., "Transonic AIC weighting method using successive Kernel expansion," *46th Structures, Structural Dynamics and Materials Conference*, 2005, AIAA 2005-1991.

[25] Thormann, R., "Extension of the subsonic doublet lattice method in transonic region using successive Kernel expansion," *Deutscher Luft- und Raumfahrtkongress*, 2009.

[26] Thormann, R. and Dimitrov, D., "Correction of aerodynamic influence matrices for transonic flow," *CEAS Aeronautical Journal*, Vol. 1, No. 1, 2014, pp. 1–12.

[27] Dimitrov, D. and Thormann, R., "DLM-Correction Methods for Aerodynamic Gust Response Prediction," *International Forum on Aeroelasticity and Structural Dynamics (IFASD)*, 2013, IFASD 2013-24C.

[28] Jameson, A., "Re-engineering the Design Process Through Computation," *Journal of Aircraft*, Vol. 36, 1999, pp. 36–50.

[29] Malik, M. R. and Bushnell, D. M., "Role of Computational Fluid Dynamics and Wind Tunnels in Aeronautics R&D," *NASA Report*, 2012, NASA TP-2012-217602.

[30] Soltnick, J. e. a., "CFD Vision 2030 Study," *A Path to Revolutionary Computational Aerosciences*, 2009, NASA/CR-2014-218178.

[31] Anderson, J., *Computational Fluid Dynamics*, MvGraw-Hill Education, 1995.

[32] Wendt, J. F., editor, *Computational Fluid Dynamics An Introduction*, Springer, 2009.

[33] Blazek, J., *Computational Fluid Dynamics: Principles and Applications*, Elsvier, 3rd ed., 2015.

[34] Heinrich, R. and Reimer, L., "Comparison of Different Approaches for Gust Modeling in the CFD Code TAU," *International Forum on Aeroelasticity & Structural Dynamics*, 2013, IFAS 2013-36B.

[35] Thormann, R., Pagliuca, G., and Timme, S., "Influence of Gust Modelling on Free-Flight Aerofoils," *International Forum on Aeroelasticity and Structural Dynamics (IFASD)*, 2017, IFASD 2017-195.

[36] Hixon, R., Mankbadi, R. R., and Scott, J. R., "Application of a nonlinear computational aeroacoustics code to the gust-airfoil problem," *AIAA Journal*, Vol. 44, No. 2, 2006, pp. 323–328.

[37] Tang, L. and Baeder, J. D., "Adaptive Euler simulations of airfoil-vortex interaction," *International journal for numerical methods in fluids*, Vol. 53, No. 5, 2007, pp. 777–792.

[38] Lighthill, M. J., "On displacement thickness," *Journal of Fluid Mechanics*, Vol. 4, No. 4, 1958, pp. 383.

[39] Srinivasan, G. R., McCroskey, W. J., and Baeder, J. D., "Aerodynamics of two-dimensional blade-vortex interaction," *AIAA Journal*, Vol. 24, No. 10, 1986, pp. 1569–1576.

[40] Parameswaran, V. and Baeder, J. D., "Indicial Aerodynamics in Compressible Flow-Direct Computational Fluid Dynamic Calculations," *Journal of Aircraft*, Vol. 34, No. 1, 1997, pp. 131–133.

[41] Stephens, C. H., Andrew, S. A. J., and Kajal, K. G., "Application of the transpiration method for aeroservoelastic prediction using CFD," *39th AIAA/ASME/ASCE/AHS/ASC Structures, Structural Dynamics, and Materials Conference and Exhibit*, 1998, pp. 1–8.

[42] Zaide, A. and Raveh, D. E., "Numerical simulation and reduced-order modeling of airfoil gust response," *AIAA Journal*, Vol. 44, No. 8, 2006, pp. 1826–1834.

[43] Sitaraman, J. and Baeder, J. D., "Computational-fluid-dynamics-based enhanced indicial aerodynamic models," *Journal of Aircraft*, Vol. 41, No. 4, 2004, pp. 798–810.

[44] Zhang, W., Ye, Z., Yang, Q., and Shi, A., "Gust response analysis using CFD-based reduced order models," *47th AIAA Aerospace Sciences Meeting Including The New Horizons Forum and Aerospace Exposition*, No. January, 2009, pp. 1–8.

[45] Liauzun, C., "Aeroelastic Response to Gust Using CFD Teqchniques," 2010, FEDSM-ICNMM 2010-30153.

[46] Wang, Z., Zhang, Z., Chen, P. C., and Sarhaddi, D., "A compact cfd-based reduced order modeling for gust analysis," *52nd AIAA/ASME/ASCE/AHS/ASC Structures, Structural Dynamics and Materials Conference*, 2011.

[47] Dong, G., Min, X., and Shilu, C., "Nonlinear Gust Response Analysis of Free Flexible Aircraft," *International Journal of Intelligent Systems and Applications*, Vol. 2, 2013, pp. 1–15.

[48] Bartels, R., "Developing an Accurate CFD Based Gust Model for the Truss Braced Wing Aircraft," *31st AIAA Applied Aerodynamics Conference*, 2013.

[49] Wales, C., Jones, D., and Gaitonde, A., "Simulation of Airfoil Gust Responses Using Prescribed Velocities," *International Forum on Aeroelasticity and Structural Dynamics*, 2011, IFASD-2011-53.

[50] Wales, C., Gaitonde, A., and Jones, D., "Reduced order modelling for aeroelastic aerofoil response to a gust," *51st AIAA Aerospace Sciences Meeting including the New Horizons Forum and Aerospace Exposition*, 2013, AIAA 2013-0790.

[51] Wales, C., Jones, D., and Gaitonde, A., "Prescribed Velocity Method for Simulation of Aerofoil Gust Responses," *Journal of Aircraft*, 2015, pp. 64–76.

[52] Huntley, S. J., Jones, D., and Gaitonde, A. L., "2D and 3D gust response using a prescribed velocity method in viscous flows," *6th AIAA Fluid Dynamics Conference*, 2016, AIAA 2016-4259.

[53] Jirasek, A., "Vortex-Generator Model and Its Application to Flow Control," *Journal of Aircraft*, Vol. 42, No. 6, 2005, pp. 1486–1491.

[54] Jirasek, A., "CFD Analysis of Gust Using Two Different Gust Models," *RTO AVT-189 Specialist Meeting on Assessment of Stability and Control Prediction Methods for Air and Sea Vehicles*, 2011.

[55] Park, K. C. and Felippa, C. A., "Partitioned analysis of coupled systems," *Computational Methods in Transient Analysis*, edited by T. Belytschko and T. J. R. Hughes, 1983.

[56] Zienkiewicz, O. C. and Chan, A. H. C., *Coupled Problems and Their Numerical Solution*, Springer, 1989, pp. 139–176.

[57] Piperno, S. and Farhat, C., "Partitioned procedures for the transient solution of coupled aeroelastic problems Part II: energy transfer analysis and three-dimensional applications," *Computer Methods in Applied Mechanics and Engineering*, Vol. 190, No. 24, 2001, pp. 3147–3170.

[58] Heinrich, R., Kroll, N., Neumann, J., and Nagel, B., "Fluid-Structure Coupling for Aerodynamic Analysis and Design - A DLR Perspective," *46th AIAA Aerospace Sciences Meeting and Exibition*, 2006, AIAA 2008-561.

[59] Rodden, W. P., *Theoretical and Computational Aeroelasticity*, Crest Publishing, 1st ed., 2011.

[60] Reimer, L., Ritter, M., Heinrich, R., and Krüger, W., "CFD-based Gust Load Analysis for a Free-flying Flexible Passenger Aircraft in Comparison to a DLM-based Approach," *22nd AIAA Computational Fluid Dynamics Conference*, 2015, AIAA 2015-2455.

[61] Huntley, S. J., Jones, D., and Gaitonde, A. L., "Aeroelastic Gust Response of an Aircraft Using a Prescribed Velocity Method in Viscous Flows," *23rd AIAA Computational Fluid Dynamics Conference*, 2017, AIAA 2017-3616.

[62] Whitehead, D. S. and Grant, J. R., "Force and Moment Coefficients of High Deflection Cascades," *2nd International Symposium on Aeroelasticity in Turbomachinery*, 1981.

[63] Verdon, J. M. and Caspar, J. R., "Development of a Linear Unsteady Aerodynamic Analysis for Finite-Deflection Subsonic Cascades," *AIAA Journal*, Vol. 20, No. 9, 1982, pp. 1259–1267.

[64] Verdon, J. M. and Caspar, J. R., "A Linearized Unsteady Aerodynamic Analysis for Transonic Cascades," *Journal of Fluid Mechanics*, Vol. 149, 1984, pp. 403–429.

[65] Hall, K. C. and Clark, W. S., "Linearized Euler Predictions of Unsteady Aerodynamic Loads in Cascades," *AIAA Journal*, Vol. 31, No. 3, 1993, pp. 540–550.

[66] Hall, K. C., Clark, W. S., and Lorence, C. B., "A Linearized Euler Analysis of Unsteady Transonic Flows in Turbomachinery," *Journal of Turbomachinery*, Vol. 116, No. 3, 1994, pp. 477–488.

[67] Mortchéléwicz, G. D., "Application des Équations d'Euler Linéarisées á la Prévision du Flottement," *85th Meeting of the AGARD Structures and Materials Panel*, 1997, AGARD Report 822: Numerical Unsteady Aerodynamic and Aeroelastic Simulation.

[68] Widhalm, M., Dwight, R. P., Thormann, R., and Hübner, A. R., "Efficient Computation of Dynamic Stability Data with a Linearized Frequency Domain Solver," *5th European Conference on Computational Fluid Dynamics*, 2010, ECCOMAS CFD 2010.

[69] Weishäupl, C. and Laschka, B., "Small Disturbance Euler Simulations for Delta Wing Unsteady Flows due to Harmonic Oscillations," *Journal of Aircraft*, Vol. 41, No. 4, 2004, pp. 782–789.

[70] Clark, W. S. and Hall, K. C., "A Time-Linearized Navier-Stokes Analysis of Stall Flutter," *Journal of Turbomachinery*, Vol. 122, No. 3, 2000, pp. 467–476.

[71] Pechloff, A. and Laschka, B., "Small Disturbance Navier-Stokes Method: Efficient Tool for Predicting Unsteady Air Loads," *Journal of Aircraft*, Vol. 43, No. 1, 2006, pp. 17–29.

[72] Pechloff, A. and Laschka, B., "Small Disturbance Navier-Stokes Computations for Low-Aspect-Ratio Wing Pitching Oscillations," *Journal of Aircraft*, Vol. 47, No. 3, 2010, pp. 737–753.

[73] Thormann, R. and Widhalm, M., "Linear-Frequency-Domain Predictions of Dynamic-Response Data for Viscous Transonic Flows," *AIAA Journal*, Vol. 51, No. 11, 2013, pp. 2540–2557.

[74] Thormann, R. and Widhalm, M., "Forced Motion Simulation using a Linear Frequency Domain Solver for a Generic Transport Aircraft," *International Forum on Aeroelasticity and Structural Dynamics (IFASD)*, 2013, IFASD 2013-17A.

[75] Beran, P. S. and Silva, W. A., "Reduced-order modeling - New approaches for computational physics," *39th Aerospace Sciences Meeting and Exhibit, Aerospace Sciences Meetings*, 2001, AIAA 2001-853.

[76] Lucia, D. J., Beran, P. S., and Silva, W. A., "Reduced-order modeling: new approaches for computational physics," *Progress in Aerospace Sciences*, Vol. 40, No. 1-2, 2004, pp. 51–117.

[77] Taira, K., Brunton, S. L., Dawson, S. T. M., Rowley, C. W., Colonius, T., McKeon, B. J., Schmidt, O. T., Gordeyev, S., Theofilis, V., and Ukeiley, L. S., "Model Analysis of Fluid Flows: An Overview," *AIAA Journal*, Vol. 55, No. 12, 2017, pp. 4013–4041.

[78] Raveh, D. E., "Reduced-order models for nonlinear unsteady aerodynamics," *AIAA Journal*, Vol. 39, No. 8, 2001, pp. 1417–1429.

[79] Raveh, D. E., "Identification of Computational-Fluid-Dynamics Based Unsteady Aerodynamic Models for Aeroelastic Analysis," *Journal of Aircraft*, Vol. 41, No. 3, 2004, pp. 620–632.

[80] Raveh, D. E., "CFD-Based Models of Aerodynamic Gust Response," *Journal of Aircraft*, Vol. 44, No. 3, 2007, pp. 888–897.

[81] Raveh, D. E., "CFD-based gust response analysis of free elastic aircraft," *ASD Journal*, Vol. 2, No. 1, 2010, pp. 23–34.

[82] Ghoreyshi, M., Jirasek, A., and Cummings, R. M., "Computational Investigation into the Use of Response Functions for Aerodynamic-Load Modeling," *AIAA Journal*, Vol. 50, No. 6, 2012, pp. 1314–1327.

[83] Hall, K. C., "Eigenanalysis of unsteady flows about airfoils, cascades, and wings," *AIAA Journal*, Vol. 32, No. 12, 1994, pp. 2426–2432.

[84] Lumley, J. L., "The Structures of Inhomogeneous Turbulent Flow," *Atmospheric Turbulence and Radio Wave Propagation*, 1967, pp. 166–178.

[85] Karhunen, K., "Zur Spektraltheorie Stochasticher Prozesse," *Annales Academiae Scientiarum Fennicae*, Vol. 37, 1946.

[86] Loève, M., *Probability Theory*, Princeton, 1955.

[87] Wales, C., Gaitonde, A., and Jones, D., "Reduced-Order Modeling of Gust Responses," *Journal of Aircraft*, Vol. 54, No. 4, 2017, pp. 1350–1363.

[88] Theofilis, V., Hein, S., and Dallmann, U., "On the origins of unsteadiness and three-dimensionality in a laminar separation bubble," *Phil. Trans. Roy. Soc. London A*, Vol. 358, 2000, pp. 3229–3246.

[89] Bres, G. A. and Colonius, T., "Three-dimensional instabilities in compressible flow over open cavities," *Journal of Fluid Mechanics*, Vol. 599, 2008, pp. 309–339.

[90] Sartor, F., Mettot, C., and Sipp, D., "Stability, receptivity and sensitivity analyses of buffeting transonic flow over a profile," *AIAA Journal*, Vol. 53, No. 7, 2015, pp. 1980–1993.

[91] Timme, S. and Thormann, R., "Towards Three-Dimensional Global Stability Analysis of Transonic Shock Buffet," *16th AIAA Aviation Technology*, 2016, AIAA 2016-3848.

[92] Dowell, E. H., "Eigenmode analysis in unsteady aerodynamics - Reduced-order models," *AIAA Journal*, Vol. 34, No. 8, 1997, pp. 1578–1583.

[93] Florea, R., Hall, K. C., and Cizmas, G. A., "Reduced-Order Modeling of Unsteady Viscous Flow in a Compressor Cascade," *AIAA Journal*, Vol. 36, No. 6, 1999, pp. 1039–1048.

[94] Dowell, E. H., Hall, K. C., Thomas, J. P., Florea, R., Epureanu, B. I., and Heeg, J., "Reduced Order Models in Unsteady Aerodynamics," *Engineering Mechanics*, Vol. 6, No. 4, 1999, pp. 229–252.

[95] Badcock, K. J. and Woodgate, M. A., "Bifurcation Prediction of Large-Order Aeroelastic Models," *AIAA Journal*, Vol. 48, No. 6, 2010, pp. 1037–1046.

[96] Timme, S., Badcock, K. J., and Da Ronch, A., "Linear Reduced Order Modelling for Gust Response Analysis using the DLR-TAU Code," *International Forum on Aeroelasticity and Structural Dynamics (IFASD)*, 2013, IFASD 2013-36A.

[97] Woodgate, M. A. and Badcock, K. J., "Fast prediction of transonic aeroelastic stability and limit cycles," *AIAA Journal*, Vol. 45, No. 6, 2007, pp. 1370–1381.

[98] Sirovich, L., "Turbulence and the dynamics of coherent structures, Parts I-III," *Q. Appl. Math.*, Vol. XLV, 1987, pp. 561–590.

[99] Berkooz, G., Holmes, P., and Lumley, J. L., "The Proper Orthogonal Decomposition in the Analysis of Turbulent Flows," *Annual Review of Fluid Mechanics*, Vol. 25, 1993, pp. 539 –575.

[100] Dowell, E. H. and Hall, K. C., "Reduced Order Models in Unsteady Aerodynamic Models, Aeroelasticity and Molecular Dynamics," *ICAS - 26th Congress of International Council of the Aeronautical Sciences*, 2008, ICAS 2008-0.1.

[101] Holmes, P., Lumley, J. L., Berkooz, G., and Rowley, C. W., *Turbulence, coherent structures, dynamical systems and symmetry*, Cambridge Univ. Press, 2nd ed., 2012.

[102] Kim, T., "Frequency-Domain Karhunen-Loève Method and Its Application to Linear Dynamic Systems," *AIAA Journal*, Vol. 36, No. 11, 1998, pp. 2117–2123.

[103] Hall, K. C., Thomas, J. P., and Dowell, E. H., "Proper Orthogonal Decomposition Technique for Transonic Unsteady Aerodynamic Flows," *AIAA Journal*, Vol. 38, No. 10, 2000, pp. 1853–1862.

[104] Beran, P. S., Lucia, D. J., and Pettit, C. L., "Reduced-order modelling of limit-cycle oscillation for aeroelastic systems," *Journal of Fluids and Structures*, Vol. 19, No. 5, 2004, pp. 575–590.

[105] Lieu, T., Farhat, C., and Lesoinne, M., "POD-based Aeroelastic Analysis of a Complete F-16 Configuration: ROM Adaptation and Demonstration," 2005, AIAA 2005-2295.

[106] Amsallem, D., Cortial, J., and Farhat, C., "Towards Real-Time Computational-Fluid-Dynamics-Based Aeroelastic Computations Using a Database of Reduced-Order Information," *AIAA Journal*, Vol. 48, No. 9, 2010, pp. 2029–2037.

[107] Bourguet, R., Braza, M., and Dervieux, A., "Reduced-order modeling of transonic flows around an airfoil submitted to small deformations," *Journal of Computational Physics*, Vol. 230, No. 1, 2011, pp. 159–184.

[108] Crowell, A. R. and J., M. J., "Model Reduction of Computational Aerothermodynamics for Hypersonic Aerothermoelasticity," *AIAA Journal*, Vol. 50, No. 1, 2012, pp. 74–84.

[109] Willcox, K. and Peraire, J., "Balanced Model Reduction via the Proper Orthogonal Decomposition," *AIAA Journal*, Vol. 40, No. 11, 2002, pp. 2323–2330.

[110] Rowley, C. W., "Model Reduction for Fluids, using Balanced Proper Orthogonal Decomposition," *International Journal of Bifurcation and Chaos*, Vol. 15, No. 3, 2005, pp. 997–1013.

[111] Dergham, G., Sipp, D., Robinet, J.-C., and Barbagallo, A., "Model reduction for fluids using frequential snapshots," *Physics of Fluids*, Vol. 23, No. 6, 2011, pp. 064101.

[112] Juang, J.-N. and Pappa, R. S., "An Eigensystem Realization Algorithm for Modal Parameter Identification and Model Reduction," *Journal of Guidance*, Vol. 8, No. 5, 1985, pp. 620–628.

[113] Kaiser, C., Thormann, R., Dimitrov, D., and Nitzsche, J., "Time-Linearized Analysis of Motion-Induced and Gust-Induced Airloads with the DLR TAU Code," *Deutscher Luft- und Raumfahrtkongress*, 2015.

[114] Förster, M. and Breitsamter, C., "Aeroelastic Prediction of Discrete Gust Loads Using Nonlinear and Time-Linearized CFD-Methods," *Journal of Aeroelasticity and Structural Dynamics*, Vol. 3, No. 3, 2015, pp. 252–255.

[115] Bekemeyer, P. and Timme, S., "Reduced Order Gust Response Simulation using Computational Fluid Dynamics," *57th AIAA/ASCE/AHS/ASC Structures, Structural Dynamics, and Materials Conference*, 2016, AIAA 2016-1485.

[116] Bekemeyer, P., Thormann, R., and Timme, S., "Frequency-Domain Gust Response Simulation using Computational Fluid Dynamics," *AIAA Journal*, Vol. 55, No. 7, 2017, pp. 2174–2185.

[117] Bekemeyer, P., Thormann, R., and Timme, S., "Rapid Gust Response Simulation of Large Civil Aircraft using Computational Fluid Dynamics," *RAeS Applied Aerodynamics Conference*, 2016.

[118] Bekemeyer, P., Thormann, R., and Timme, S., "Rapid Gust Response Simulation of Large Civil Aircraft using Computational Fluid Dynamics," *The Aeronautical Journal*, Vol. 121, 2017, pp. 1795–1807.

[119] Bekemeyer, P. and Timme, S., "Reduced Order Transonic Aeroelastic Gust Response Simulation of Large Aircraft," *35th AIAA Applied Aerodynamics Conference*, 2017, AIAA 2017-4361.

[120] Wilcox, D. C., *Turbulence modeling for CFD*, DCW Industries, Inc., 2006.

[121] Spalart, P. R. and Allmaras, S. R., "A One-Equation Turbulence Model for Aerodynamic Flows," *Recherche Aerospatiale*, Vol. 1, 1994, pp. 5–21.

[122] Thormann, R. and Timme, S., "Efficient Aerodynamic Derivative Calculation in Three-Dimensional Transonic Flow," *RAeS Applied Aerodynamics Conference*, 2016.

[123] Meinel, M. and Einarsson, G., "The FlowSimulator framework for massively parallel CFD applications," *PARA 2010 - State of the Art in Scientific and Parallel Computing*, 2010.

[124] Schwamborn, D., Gerhold, T., and Heinrich, R., "The DLR TAU-Code: Recent Applications in Research and Industry," *European Conference on Computational Fluid Dynamics*, 2006, ECCOMAS CFD 2006.

[125] Stickan, B., Dillinger, J., and Schewe, G., "Computational aeroelastic investigation of a transonic limit-cycle-oscillation experiment at a transport aircraft wing model," *Journal of Fluids and Structures*, Vol. 49, 2014, pp. 223–241.

[126] Neumann, J. and Mai, H., "Gust response: Simulation of an Aeroelastic Experiment by a Fluid-Structure Interaction Method," *Journal of Fluids and Structures*, Vol. 38, 2013, pp. 290–302.

[127] Jameson, A., Schmidt, W., and Turkel, E., "Numerical Solutions of the Euler Equations by Finite Volume Methods Using Runge-Kutta Time-Stepping Schemes," *14th Fluid and Plasma Dynamic Conference*, 1981, AIAA 1981–1259.

[128] Dwight, R., "An Implicit LU-SGS Scheme for Finite-Volume Discretizations of the Navier-Stokes Equations on Hybrid Grids," *DLR-FB-2005-05*, 2006.

[129] Rendall, T. C. S. and Allen, C. B., "Unified fluidstructure interpolation and mesh motion using radial basis functions," *International Journal for Numerical Methods in Engineering*, Vol. 74, No. 10, 2008, pp. 1519–1559.

[130] Michler, A., "Aircraft control surface deflection using RBF-based mesh deformation," *International Journal for Numerical Methods in Engineering*, Vol. 88, 2011, pp. 986–1007.

[131] Jirasek, A., M., D., and Navratil, J., "Computational Fluid Dynamics Study of Benchmark Supercritical Wing at Flutter Condition," *AIAA Journal*, Vol. 55, No. 1, 2017, pp. 153–160.

[132] Newmark, N. M., "A method of computation for structural dynamics," *Journal of Engineering Mechanics*, Vol. 85, No. 3, 1959, pp. 67–94.

[133] Xu, S., Timme, S., and Badcock, K. J., "Enabling off-design linearised aerodynamics analysis using Krylov subspace recycling technique," *Computers and Fluids*, Vol. 140, 2016, pp. 385–396.

[134] Saad, Y., *Iterative Methods for Sparse Linear Systems*, Society for Industrial and Applied Mathematics, Philadelphia, PA, 2nd ed., 2003.

[135] Thormann, R. and Timme, S., "Application of Harmonic Balance Method for Non-linear Gust Responses," *AIAA/ASCE/AHS/ASC Structures, Structural Dynamics, and Materials Conference*, 2018, AIAA 2018-1686.

[136] Amsallem, D. and Farhat, C., *On the Stability of Reduced-Order Linearized Computational Fluid Dynamics Models Based on POD and Galerkin Projection: Descriptor vs Non-Descriptor Forms*, Springer International Publishing, 2014, pp. 215–233.

[137] Timme, S., *Transonic Aeroelastic Instability Searches Using a Hierarchy of Aerodynamic Models*, Ph.D. thesis, University of Liverpool, 6 2010.

[138] Theofilis, V., "Global Linear Instability," *Annual Review of Fluid Mechanics*, Vol. 43, 2011, pp. 319–352.

[139] Schmid, P. J., "Nonmodal Stability Theory," *Annual Review of Fluid Mechanics*, Vol. 39, 2007, pp. 129–162.

[140] Kim, J. and Bewley, T. R., "A Linear Systems Approach to Flow Control," *Annual Review of Fluid Mechanics*, Vol. 39, 2007, pp. 383–417.

[141] Balay, S. and et al., *PETSc Users Manual*, Mathematics and Computer Science Division, Argonne National Laboratory, 3rd ed., 9 2011.

[142] Mettot, C., Florent, R., and Denis, S., "Computation of eigenvalue sensitivity to base flow modifications in a discrete framework: Application to open-loop control," *Journal of Computational Physics*, Vol. 269, 2014, pp. 234–258.

[143] Nitzsche, J., "A Numerical Study on Aerodynamic Resonance in Transonic Separated Flow," *International Forum on Aeroelasticity and Structural Dynamics (IFASD)*, 2009, IFASD 2009-126.

[144] Iovnovich, M. and Raveh, D. E., "Transonic Unsteady Aerodynamics in the Vicinity of Shock-Buffet Instability," *Journal of Fluids and Structures*, Vol. 29, 2012, pp. 131–142.

[145] Broyden, C. G., "A class of methods for solving nonlinear simultaneous equations," *Mathematics of Computation (American Mathematical Society)*, Vol. 19, No. 92, 1965, pp. 577–593.

[146] European Aviation Safety Agency, "Certification Specifications for Large Aeroplanes Amendment 17 (CS-25)," 2015.

[147] Silva, W., "Recent Enhancements to the Development of CFD-Based Aeroelastic Reduced-Order Models," *48th AIAA/ASME/ASCE/AHS/ASC Structures, Structural Dynamics, and Materials Conference, Structures, Structural Dynamics, and Materials and Co-located Conferences*, 2007.

[148] Kalashnikova, I. and Barone, M. F., "Efficient non-linear proper orthogonal decomposition/Galerkin reduced order models with stable penalty enforcement of boundary conditions," *International Journal for Numerical Methods in Engineering*, Vol. 90, No. 11, 2012, pp. 1337–1362.

[149] Beran, M. F., Kalashnikova, I., Segalman, D. J., and Thornquist, H. K., "Stable Galerkin reduced order models for linearized compressible flow," *Journal of Computational Physics*, Vol. 228, 2009, pp. 1932–1946.

[150] Hassig, H. J., "An approximate true damping solution of the flutter equation by determinant iteration," *Journal of Aircraf*, Vol. 8, No. 11, 1971, pp. 885–889.

[151] Pagliuca, G., Bekemeyer, P., Thormann, R., and Timme, S., "Model reduction for gust load analysis of free-flying aircraft," 2017, IFASD 2017-148.

[152] Tantaroudas, N., Da.Ronch, A., Gai, G., Badcock, K. J., and Palacios, R., "An Adaptive Aeroelastic Control Approach by using Nonlinear Reduced Order Models," *14th AIAA Aviation Technology, Integration, and Operations Conference*, 2014, AIAA 2014-2590.

[153] Iorio, M. C., Gonzalez, L. M., and Ferrer, E., "Direct and adjoint global stability analysis of turbulent transonic flows over a NACA0012 profile," *International Journal for Numerical Methods in Fluids*, Vol. 76, No. 3, 2014, pp. 147–168.

Appendix A

Certification Requirements for Gust Loads

Regulations concerning gusts and turbulence can be found in CS25.341 or FAR25.341 and are, except from a few words, identical [5]. Within these, gusts are either considered as discrete or continuous and guidelines are provided how to correctly analyse gust induced loads during the certification process. For both excitation types, the loads on each part of the structure must be computed using a dynamic analysis that contains all relevant structural modes, flight dynamics degrees of freedom and unsteady aerodynamic effects. Moreover, if a control system is present also this needs to be accounted for.

The discrete shape, also known as 1-cos gust, occurring in vertical and lateral direction is described by

$$\begin{aligned} U &= \frac{U_{\mathrm{ds}}}{2}\left[1 - cos\left(\frac{2\pi \mathrm{s}}{L_g}\right)\right] && \text{for} \quad 0 \leq \mathrm{s} \leq L_g \\ U &= 0 && \text{for} \quad \mathrm{s} > L_g \end{aligned} \tag{A.1}$$

where s, U_{ds} and L_g denote the distance penetrated into the gust, the design gust airspeed and the gust length, respectively. For the gust length L_g, a sufficient number between 18 m and 214 m must be investigated. Considering further guidelines provided in the acceptable means of compliance a total number of 30 in vertical and lateral directions is sufficient.

The design gust velocity is computed by

$$U_{ds} = U_{ref} F_g \left(\frac{H}{350}\right)^{\frac{1}{6}} \tag{A.2}$$

with U_{ref} describing the reference gust velocity in equivalent airspeed and F_g describing the flight profile alleviation factor. The reference gust velocity depends on the aircraft

speed and altitude. The values between maximum gust intensity speed V_B and cruise speed V_C are shown in Fig. A.1. At dive speed V_D, the gust intensity is reduced by the factor 0.5.

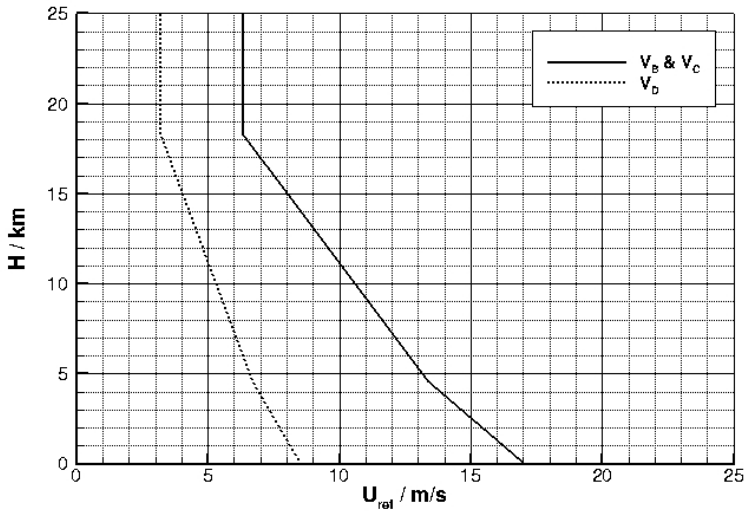

Figure A.1: Values for U_{ref} for different aircraft speeds

The flight profile alleviation factor in Eq. (A.2) depends on the altitude and different aircraft load cases. At see level the flight profile alleviation factor can be calculated by

$$F_g = 0.5(F_{gz} + F_{gm}) \tag{A.3}$$

where

$$F_{gz} = 1 - \frac{Z_{mo}}{76200}$$

$$F_{gm} = \sqrt{R_2 \tan\left(\frac{\pi R_1}{4}\right)}$$

$$R_1 = \frac{\text{Maximum Landing Weight}}{\text{Maximum Take-off Weight}}$$

$$R_2 = \frac{\text{Maximum Zero Fuel Weight}}{\text{Maximum Take-off Weight}}$$

with Z_{mo} denoting the maximum operating altitude. Above sea level the flight profile alleviation factor increases linearly to a value of 1.0 at the maximum operating altitude.

For continuous turbulence analysis, the limit loads must be determined using the following equation

$$P_L = P_{L-1g} \pm U_\sigma \overline{A} \tag{A.4}$$

where P_{L-1g} describes the 1-g steady load, $\overline{A}$ the ratio of the root-mean-square incremental load and U_σ the limit turbulence intensity in true airspeed. The root-mean-

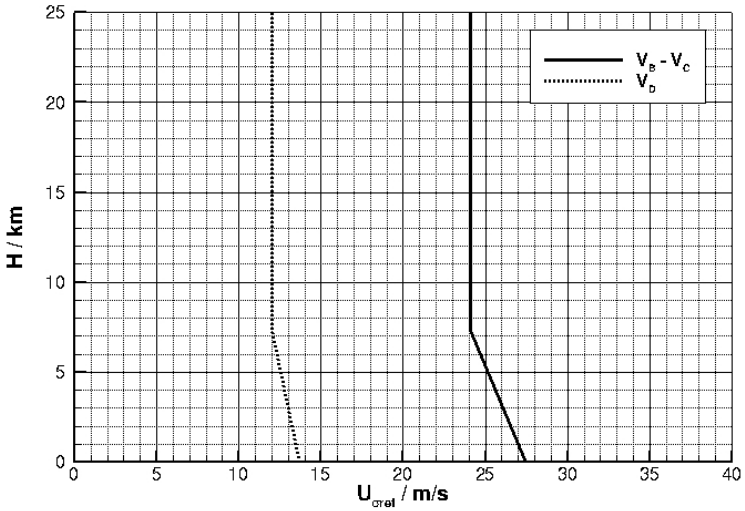

Figure A.2: Values for $U_{\sigma ref}$ for different aircraft speeds

square loads $\overline{A}$ are calculated using

$$\overline{A} = \sqrt{\int_0^\infty |H(\omega^*)|^2 \Phi_I(\omega^*) d(\omega^*)} \tag{A.5}$$

For the normalised power spectral density Φ_I the von-Kármán formula is applied

$$\Phi_I(\omega^*) = \frac{L}{\pi} \frac{1 + \frac{8}{3}(1.339\omega^* L)^2}{[1 + (1.339\omega^* L)^2]^{\frac{11}{6}}} \tag{A.6}$$

where ω^* denotes the reduced frequency and L the scale of turbulence equal to $2,500$ ft. The limit turbulence intensities U_σ is the continuous equivalent to the design gust velocity U_{ds} and can be calculated for speed between V_B and V_C using:

$$U_\sigma = U_{\sigma,ref} F_g \tag{A.7}$$

where F_g is the flight profile alleviation factor described in Eq. (A.3). The limit turbulence intensity $U_{\sigma,ref}$ depends on the altitude and the flight speed and is shown in Fig. A.2. For speeds between V_D and V_C a linear interpolation is necessary.